1-2-2012

State-resolved slice imaging of photochemical dynamics

Herath mudiyans nuradhika Herath
Wayne State University,

STATE-RESOLVED SLICE IMAGING OF PHOTOCHEMICAL DYNAMICS

by

HERATH MUDIYANSELAGE NURADHIKA HERATH

DISSERTATION

Submitted to the Graduate School

of Wayne State University,

Detroit, Michigan

in partial fulfillment of the requirements

for the degree of

DOCTOR OF PHILOSOPHY

2012

MAJOR: CHEMISTRY (Physical)

Approved by:

_____

Advisor Date

_____

_____

_____

_____

DEDICATION

- To my loving mother, father, two sisters and husband Asanga-

ACKNOWLEDGEMENTS

First and foremost I would like to sincerely and gratefully thank my advisor Prof. Arthur G. Suits for his valuable guidance, encouragements and patience though out this period. His positive attitudes towards solving difficult problems, always enrich with new ideas and techniques never cease to amaze me. I am deeply indebted for the every thing Prof. Suits has done for me.

Secondly I take this opportunity to thank all the Suits group members to made this period a productive and enjoyable one. I was very fortune enough to work with many post-docs from whom I learned a great deal of techniques and acquired knowledge. I would like to thank Dr. Vasiliy Goncharov, Dr. Stephanie Everhart and Dr. Michael Hause for teaching me many techniques and assisting me during the experiments. Also I would like to thank the former graduate students Dr. Ruchira Silva, Dr. Wilson Gichuhi for their help and the support during the period of my Phd. Special thanks goes to Dr. Armando Estilliore and Ms. Lu Yan for helping me in various ways. I would also acknowledge Ms. Brenedette Broderick for assisting me for the experiments in the last few months of the study.

Also I would like to thank our collaborators Prof. Oleg Vasyuntinskii, Prof. M.C. Lin and Dr. R. Zhu for proving us with the theoretical calculations which greatly helped to explaining our results.

I take this opportunity to thank my committee members Prof. Vladimir Chernyak, Prof. Claudio N. Verani and Prof. Steven Salley for their valuable time, suggestions and comments during the preparation of my dissertation.

This journey would have not been easy without the efficient administrative staff in Chemistry Department. I want to thank Sharon Kelly, Melissa Barton, Mary Wood, Diane Klimas,

Erin Bachert, Debbie McCreless and Bernie Meisik for all their help throughout my study. Also would like to extend my thanks to Nestor Ocampo for his support in various ways.

I thank all my Sri Lankan friends making this is an unforgettable experience. Special thanks goes to Hansini Mundigala, Pavithra Pathirathne, Thushani Herath, Chadani Warnasooriya and their families for the support, encouragements and enjoyable time we shared.

Last but not least I would like to thank my family for their support during this period. A special thanks goes to my mother who has been living behind the every success in my life and encouraging me to follow my dreams. I am very fortunate have two wonderful sisters, Sagarika Herath and Ruchira Herath and their families who take care of my parents while I am away to make my dreams come true. I thank my husband Asanga Bandara for his great understanding, patience, and unconditional love. His encouragements and advices kept me going in the difficult times in my PhD carrier.

TABLE OF CONTENTS

LIST OF TABLES

LIST OF FIGURES

PREFACE

This dissertation is based closely on the following refereed publications:

Chapter 1

Nuradhika Herath, Arthur G. Suits, "Roaming radical reactions", *J. Chem. Phys. Lett.* 2, 642-647, 2011

Chapter 2

Vasiliy Goncharov, **Nuradhika Herath**, Andres Arregui, Luis Banares, and Arthur G. Suits, "Masked velocity map imaging: A one-laser-beam doppler-free spectroscopic technique", *J Phys. Chem. A*, 113(16):38403843, 2009.

Chapter 3

Vasiliy Goncharov, **Nuradhika Herath**, and Arthur G. Suits,"Roaming dynamics in acetone dissociation", *J Phys. Chem. A*,112(39):94239428, 2008.

Chapter 4

Michael L. Hause, **Nuradhika Herath**, Rongshun Zhu, M. C. Lin, Arthur G. Suits,"Roaming-mediated isomerization of the photodissociation of nitrobenzene", *Nat Chem*, 3, 932-937, 2011

Chapter 5

Nuradhika Herath, Michael L. Hause, Arthur G. Suits," The photodissociation dynamics of tetrachloroethylene",*J. Chem. Phys.* , 134, 164301-164308, 2011

Chapter 6

Nuradhika Herath, Stephanie C. Everhart, Oleg S. Vasyuntinskii, Arthur G. Suits,"Slice imaging of nitric acid photodissociation : The $O(^1D)$ + HONO channel",*J. Chem. Phys.*,134, 0343011-034318, 2011

Chapter 1

Introduction

1.1 Introduction

At the beginning of the twentieth century, the development of the field of chemical kinetics and the knowledge of thermodynamics revealed that chemical changes occur through a complex network of elementary reactions. Attempts to unveil these elementary reactions began a revolutionary new approach, giving birth to the field of chemical dynamics. At the beginning, efforts were made to identify the reaction rates in the individual underlying processes i.e. isolation of the elementary reactions were carried out. These investigations emphasized the importance of the gas-phase studies since they provide the ability to elucidate the reactions involving one (unimolecular reactions) or two (bimolecular reactions) molecules, generally the primary reactive events.

Studies of chemical dynamics establishes the foundation for understanding the complex and extreme reactive environments such as the atmosphere of the earth and the other planets, interstellar clouds and combustion processes. Such studies required advanced laboratory techniques to isolate the reactants, products or the intermediate radicals generated during the chemical processes. As a result, the techniques span from the early flash photolysis experiments to the development of molecular beams to the advanced laser sources ranging from nanoseconds to ultrfast pulses and beyond. These developments elucidate the experimentally determined parameters with the theoretically obtained values of the molecular decay via the

major assumptions made by Rice, Ramsperger and Kessel (RRK theory) in late 1920s. Simultaneous developments in the computational field opened the door to explore the potential energy surfaces which is considered central to our view of interatomic interactions.

The field of chemical dynamics has aforementioned broad practical benefits but the individual results do not always accurately reveal our motivations or the primary goals of the research. Therefore, the purpose of basic research is not to produce results for the immediate use but to develop the fundation of the many areas of sciences for further developments.

In this dissertation we focus on understanding unimolecular reaction dynamics using state-resolved slice imaging approach. This powerful technique allows probing both the reactants' and products' individual quantum states and determining the energy, orientation or the alignment of the products. Further aspects include identifying new channels and mechanisms created during the photochemical events and product branching ratios. Examples included here are the studies done on acetone and nitrobenzene photodissociation, to search for new mechanisms created during the photodissociation. These are related to the roaming dynamics reported recently[1, 2] in formaldehyde photodissociation. Furthermore, the photodissociation dynamics studies of tetrachloroethylene and nitric acid will be reported. As will be seen, the power of the slice imaging technique applied here can give data on the *correlations* among these quantities for both products in a dissociation event, yielding unprecedented insight.The following two sections of the introduction include a brief overview of the roaming mechanism, a key aspect of the results presented in chapters 3 and 4, and the issue of angular momentum polarization in photodissociation, which is a *vector correlation* readily measured using the ion imaging technique, and a key aspect of the nitric acid results reported in chapter 6.

1.2 Introduction to Roaming Dynamics

The dissociation of a highly vibrationally excited molecule is a violent event; atoms thrash about, energy flows here and there, and in some sense, it is over very quickly, perhaps

nanoseconds for a medium sized molecule in a combustion environment. However, in another sense, when measured by the number of vibrational periods of the bond that finally breaks, it is a remarkably slow process. For a vibrational period of tens of femtoseconds, for example, this nanosecond lifetime represents on the order of a million oscillations. From this point of view, we might well ask why it should take so long. The simple answer is that enough energy must accumulate in one bond to break it. To determine the dissociation rate, statistical theories in effect simply count the number of ways that the energy may be partitioned in a bond in excess of the energy needed to break it and divide this by the total number of ways the energy may be distributed in the molecule. For a polyatomic molecule with its 3N - 6 vibrational degrees of freedom, there is an enormous density of states at these energies; therefore, it is very unlikely for all of the energy to happen to appear in a single bond at one time. It is far more likely that only a few vibrational quanta will be found in any one mode at any one time, and such conditions thus arise much more often. Similarly, one can readily imagine it more likely that a given vibrational mode will possess almost enough energy to dissociate rather than more than enough energy to dissociate. What happens in this case? If the energy is very close to the dissociation limit (we will see that it must be within a few hundred cm^{-1}), the bond can very nearly break, and the fragments separate to very long range. Of course, they may promptly fall back together, and the energy that had accumulated in the reaction coordinate may again be shared with the other modes for more thrashing about. However, there is another possibility. As the incipient fragments move out to long range, they will find themselves in a very flat region of the intermolecular potential and with vanishing kinetic energy. There, these radical fragments may be subject to subtle influences of the potential and begin to wander around. They may escape the forces drawing them back into the well, instead exploring remote regions of the potential surface, perhaps eventually finding a second attractive and highly reactive domain. Reaction may then occur leading to unanticipated chemical products and surprising internal energy distributions. We refer to this phenomenon as roaming, .

Although the evidence that we will present in what follows has emerged clearly only after much experimental and theoretical effort, simple reflection on the points presented above are enough to suggest that this phenomenon could make a significant contribution to product branching in unimolecular dissociation, and it might well be nearly universal. This subject has been reviewed in some detail recently;[2–4] therefore, our goal here will be to sketch a picture of roaming on this intuitive foundation, emphasizing the experimental results and pointing to some future direction for investigation. Although there had been some suggestion of such behavior in a variety of systems over the years,[5, 6] the first clear demonstration of roaming and identification of the underlying dynamics were reported in a series of combined theoretical and experimental studies[1, 7–10] of formaldehyde dissociation. Because this system so clearly illustrates the phenomenon, we will devote some attention to the formaldehyde results before turning to the broader evidence and implications of roaming.

This intriguing phenomenon was first ascribed theoretically and experimentally using formaldehyde dissociation by the Suits group in collaboration with the Bowman group at Emory. The photodissociation of formaldehyde occurs mainly in three pathways.

$$H_2CO \rightarrow H_2 + CO \qquad (channel\ 1) \tag{1.1}$$

$$H_2CO \rightarrow H + HCO \qquad (channel\ 2) \tag{1.2}$$

$$H_2CO \rightarrow [H - -HCO] \rightarrow H_2 + CO \qquad (channel\ 3) \tag{1.3}$$

A schematic representation of the energy level diagram of the formaldehyde photodissociation is illustrated in fig 1.1

The closed shell molecular products are formed via a high energy barrier on the ground state. At somewhat higher energies the decomposition occurs producing H + HCO, radical products; on the triplet surface, at still higher energies, the radical dissociation occurs via a small barrier. In all that is considered here, dissociation occurs on the ground state at energies below the triplet barrier, following internal conversion from the initially prepared

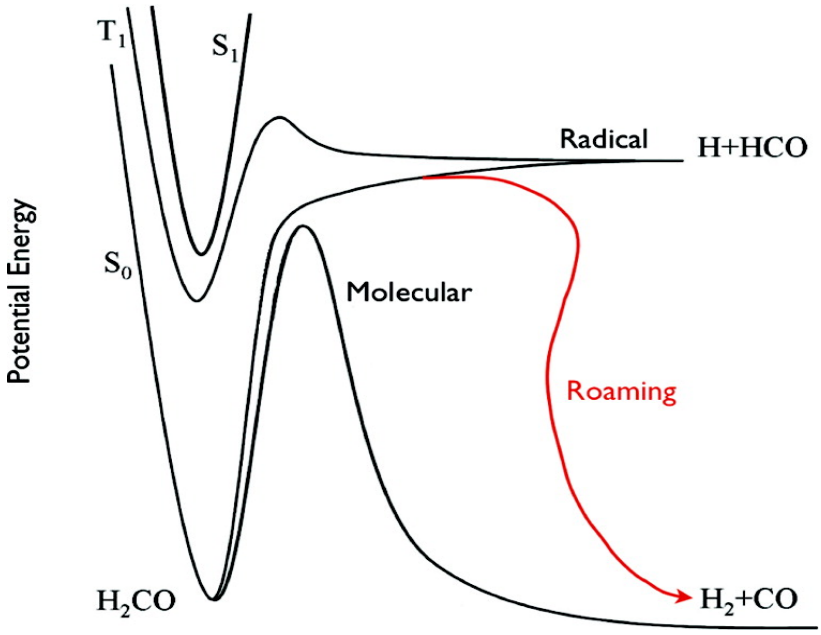

Figure 1.1: Schematic potential energy curves for the formaldehyde photodissociation

S_1.

A 1993 study from the Moore group at Berkeley showed evidence for a second molecular channel in the dissociation of formaldehyde. Their CO rotational distributions showed large excitation as the repulsive potential energy from the barrier shown in Figure 1.1 was efficiently converted to rotational excitation and translation. However, distributions obtained for dissociation above the energy of the radical channel showed, in addition, a pathway producing CO with very little rotational excitation. This was rather surprising;one set of products, CO and H_2, seemed to be influenced by the opening of another channel leading to radical products. Moore and co-workers believed that this bimodal rotational distribution was most likely related to interaction between the radical and molecular dissociation pathways, but they also considered an alternative explanation involving extreme anharmonicity of the transition state (TS) leading to dissociation from distinct geometries. We will return to these two alternative views below. Ion imaging results [1, 10] obtained a decade later in our group, reproduced in Figure 1.2, provided something not available to Moore and co-workers, state-correlated product distributions.

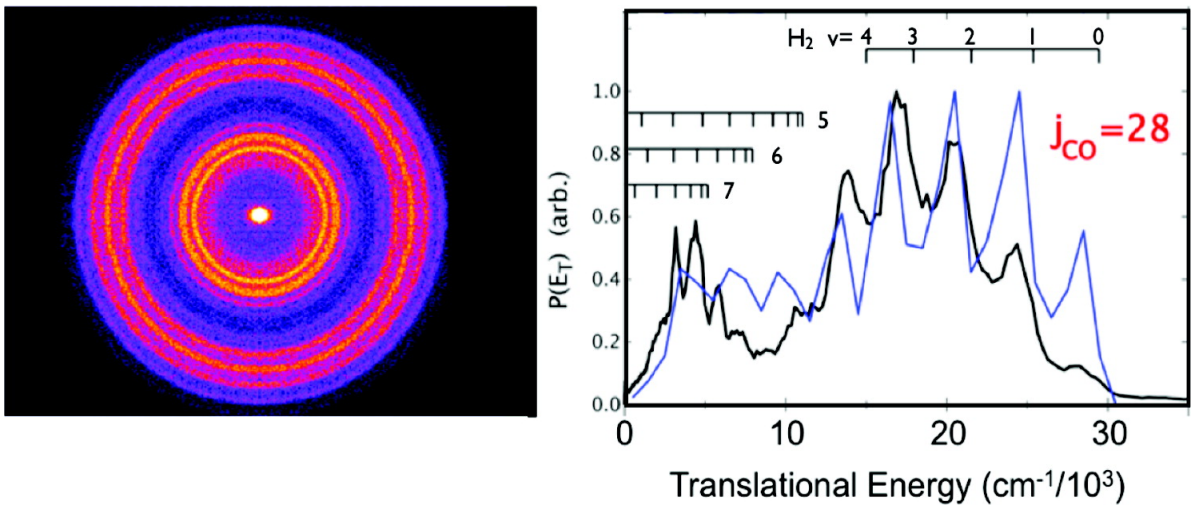

Figure 1.2: DC slice image CO (ν= 0, j= 28 for dissociation of H_2CO (left and the translational energy distributions (right) obtained from the image. The markers indicate correlated H_2 vibrational levels for J $_{H2}$ =5 (for ν= 5-7). The blue line is the result of QCT calculations. Adapted from D. Townsend *et al* , *Sci,* , 306, 1158 (2004) © AAAS

High-resolution velocity map images for specific CO quantum states give the corresponding internal state distribution for the H_2 partner by virtue of energy and momentum conservation. It became clear from the imaging results shown in Figure 1.2 that the anomalous low rotational levels highlighted in Moore's paper are associated with the production of very high vibrational levels of H_2. This surprising combination could not plausibly arise from dissociation via the normal TS geometry; therefore, an alternative pathway was clearly needed.

The definitive answer came from quasi-classical trajectory (QCT)calculations from the Bowman group at Emory that were obtained on a newly developed, high-quality ab initio potential energy surface[11] for H_2CO. Their calculations, performed under conditions chosen to mimic the experiment, gave bimodal distributions in good agreement with the imaging results. Furthermore, the trajectory calculations provided the ability to make movies of the reaction, slowed down by a factor of 10^{10}[9] or so. These trajectory animations clearly revealed the nature of the dynamics underlying the distinct sets of products; reactions that produced rotationally excited CO and vibrationally cold H_2 all followed the normal dissoci-

ation path and at some point passed through a geometry closely resembling that of the TS structure shown in Figure 1.1. In contrast, trajectories giving highly vibrationally excited H_2 followed a very different path, never visiting that geometry. Instead, one of the hydrogen atoms always ventured out 3.5 or 4 Å from the HCO fragment and then slowly roamed over the plane of the HCO, eventually finding the other H atom for reaction. Figure 1.3 shows such a roaming trajectory contrasted with a normal over-the-barrier trajectory in remarkable visualizations by F. Suits at IBM, based on the Bowman group QCT calculations [9].

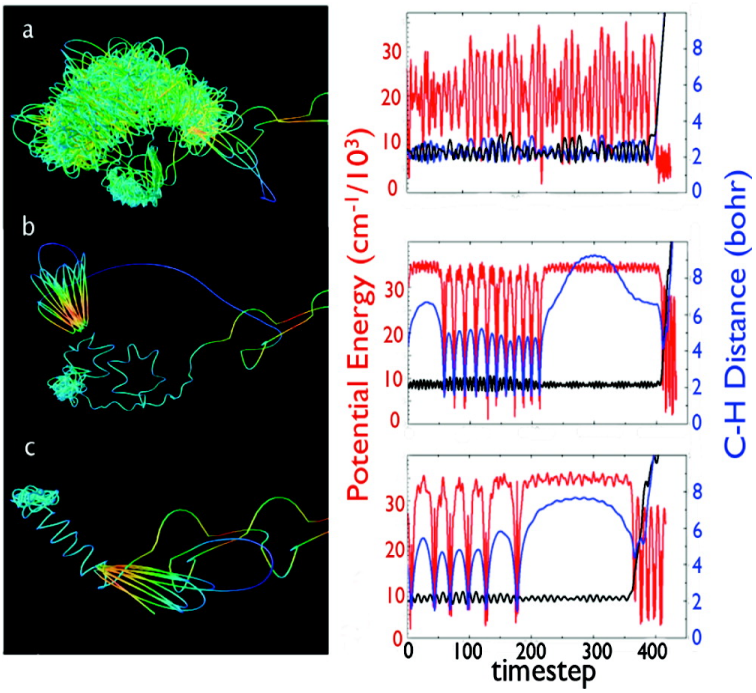

Figure 1.3: (Left) Visualizations of selected trajectories. Only H atom motions are shown, with the CO moiety omitted for clarity. The instantaneous speed is encoded in color (A) non roaming event; (B,C) roaming events (Right) Plots of C-H distances (black, blue) and the total potential energy (red) for each trajectory on the left. Adapted with the permission from S.A. Lahankar *et al*, *Chem. Phys.*, 347, 288(2008) ©Elsevier

This roaming may be viewed as a frustrated radical dissociation that leads, instead, to an intramolecular abstraction, just as we had envisioned in the introductory paragraphs above. Production of highly vibrationally excited H_2 and rotationally cold CO can be seen as a natural consequence of the extremely exoergic H + HCO reaction; therefore, the distinct

product state distributions for the formaldehyde roaming events are easy to understand in this light. For such an early barrier reaction, we expect the new bond to be highly excited and the old bond to behave as a spectator. Indeed, Bowman and co-workers have shown in trajectory calculations on the reaction of H with HCO that one component of the product distribution gives H_2 in vibrational levels of [1, 12] along with CO in low rotational levels, exactly analogous to the roaming products of H_2CO dissociation [13].

These initial formaldehyde results provided insight into the dynamics underlying the distinct product distributions but raised many questions as well. Is roaming simply a threshold phenomenon, and if not, what is its energy dependence? Is this behavior restricted to formaldehyde, or is it more general? Is it exclusively a H atom phenomenon, or may other species be involved in roaming? What are the implications of this for transition-state theory (TST), on which we base much of our theoretical understanding of chemical reactions? And what might be the practical implications of roaming if indeed this is a general but overlooked molecular decomposition mechanism?

The initial results were obtained at energies just 30-40 cm^{-1} above the radical threshold. Can roaming occur below the radical threshold? One way of examining this question is to scan the excitation laser around the radical threshold while monitoring CO products in low rotational levels (associated with roaming) or high rotational levels (representing dissociation over the barrier), an example of photofragment excitation (PHOFEX) spectroscopy. The results obtained in the vicinity of the radical threshold and below are shown in Figure 1.4.

Each peak represents a transition from the ground state to the first excited state that ultimately leads to the indicated CO quantum state that is being detected after dissociation. No mode specificity has been observed; therefore, the nature of the excited-state preparation is not significant. This is because decomposition takes place on the ground state long after the initial excitation. The threshold for the radical dissociation is marked on the plot. The top panel shows CO in j = 45, representing the normal molecular product. Peaks are seen

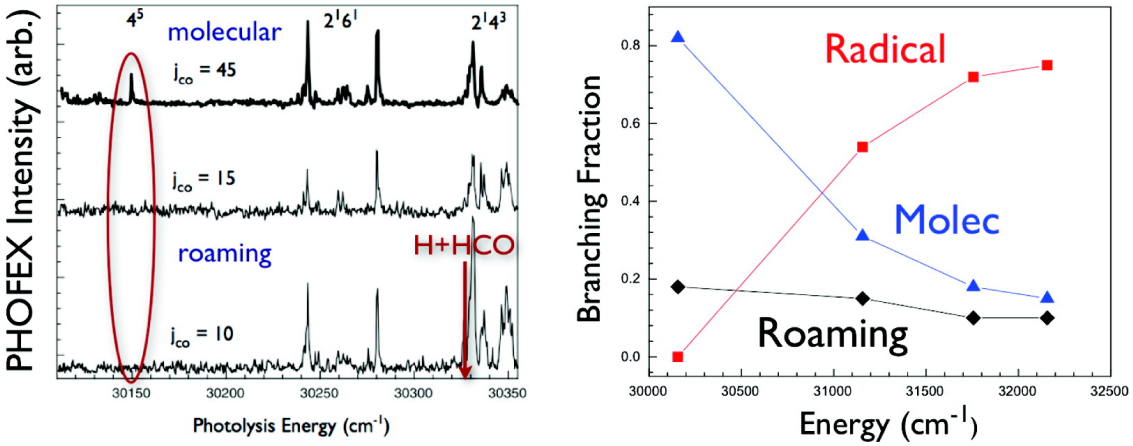

Figure 1.4: (left) PHOFEX scan across the radical dissociation threshold (30329 cm^{-1}) for indicated CO rotational levels. The red oval shows the absence of roaming at energies 180 cm^{-1} below the radical threshold. (Right) Energy-dependent multichannel branching for formaldehyde. (Right) Plots of C-H distances (black, blue) and the total potential energy (red). Adapted with the permission from S.A. Lahankar *et al*, *J. Chem. Phys.*, 126, 044314 (2007) ©AIP

corresponding to well-known metastable levels in the excited state. In the lower two panels, we see the same region of the spectrum probed on low CO rotational levels that come from roaming. As shown in the lower two spectra, roaming products are clearly seen as low as 90 cm^{-1} below the radical threshold, but by 180 cm-1 below, they are gone. The conventional molecular channel, on the other hand, persists down to the level of the barrier, well below the radical threshold.

Harding and co-workers[14] reported a distinct roaming transition- state region for formaldehyde. They refer to this as a region because it is so flat, and several of the frequencies are so low that it is unrealistic to consider it a normal TS for the purpose of calculating rates. Nevertheless, there are several noteworthy features of the saddle point that they have identified. One is that it features the roaming H atom out of the plane of HCO, about 3.5-4 Å away. This is quite consistent with the trajectory calculations, which also seem to pass through this part of the potential surface before leading to the roaming abstraction. The second key aspect of this is that the location of this saddle point is about 40 cm^{-1} below the radical asymptote. This is consistent, within plausible uncertainty in the calculation, with the

PHOFEX data in Figure 1.4.

One interesting question is whether there is any connection between this saddle point and the tight TS that leads to the normal molecular channel. Although the products seemto follow one pathway or the other, are these two saddle points related? Bowman and co-workers have recently reported[4] that one may trace a path from the roaming saddle point directly to the molecular saddle point, and this path rises only 2.5 kcal/mol above the roaming saddle point. This suggests that these two saddle points may indeed be connected, and both of the explanations given in the paper by van Zee et al. are correct; that is, the second molecular channel represents extreme anharmonicity of the TS, and at the same time, this is a consequence of the opening of the radical channel. Indeed it is the anharmonicity associated with the opening of the radical channel that is responsible for roaming. Roaming in formaldehyde is seen to occur at energies in the immediate vicinity of the radical threshold, but does this mean that it is strictly a threshold phenomenon? Again, PHOFEX spectra can shed light on this point. Such spectra, obtained up to 3000 cm^{-1} above the radical asymptote,[9] when analyzed and scaled using imaging data, yield the multichannel branching also shown in Figure 1.4. As expected, the loose TS leading to radical products means that this channel rapidly dominates once it is open, at the expense of the normal molecular channel. However, as the roaming channel is derived from the radical channel, it shows only a weak energy dependence, decreasing gradually with increasing energy.

The next question to address is that of generality. Are there other systems that demonstrate roaming behavior? The answer is a resounding yes. Acetaldehyde has been studied quite extensively in this regard, first with a report of CO Doppler profiles and vector correlations from Kable and Houston [15]. This was followed by extensive theoretical and experimental measurements that have consistently confirmed roaming behavior in acetaldehyde, only disagreeing over its extent [16–19]. FTIR measurements showed very hot methane,with up to 4 eV of internal energy, from acetaldehyde photodissociation at 308 nm. This internal state distribution was consistent with trajectory calculations on a full dimensional poten-

tial surface starting from the equilibrium geometry, which suggested that roaming was the dominant decay mechanism at these energies. Shock tube measurements[20] of the H atom yields (taken as a marker for the HCO product of the radical channel) indicated a 23% branching to the roaming radical pathway in thermal pyrolysis of acetaldehyde at temperatures of 1346-1888 K and pressures of several hundred Torr. These experimental points are shown in Figure 1.5 , paired with reduced dimensional trajectory (RDT) calculations[21] employing a six-dimensional surface (with the radicals frozen in their equilibrium geometries). The theoretical results underestimate the roaming yield slightly compared to the shock tube experiment, but all studies to date confirm roaming dynamics in this system, even under atmospheric pressure, high temperature, thermal conditions.

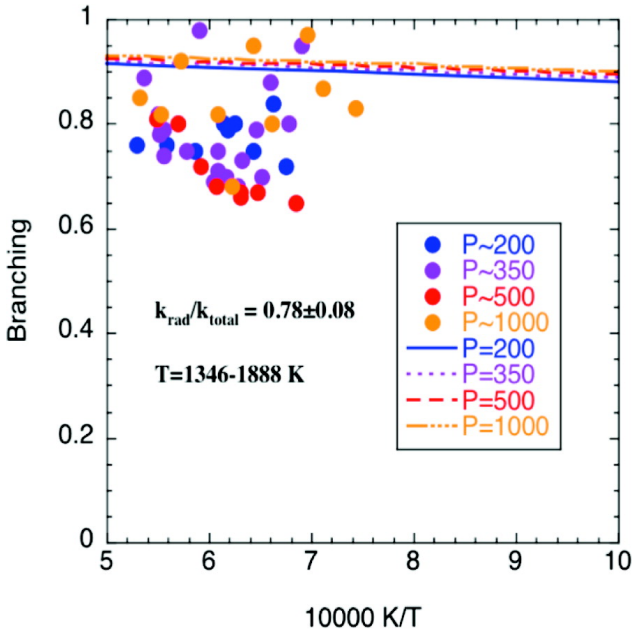

Figure 1.5: Points show results of shock tube measurements of H atom yield (corresponding to the radical channel) in acetaldehyde pyrolysis by Michael and co-workers from [20]. Lines are the result of RDT P: pressure in Torr. Adapted with the permission from L. B. Harding *et al*, *J. Phys. Chem. A*, 114, 765 (2010) ©ACS

Many additional examples of roaming dynamics have been reported. Acetone dissociation at 230 nm, one of our contributions to this topic, was recently found to give a significant yield of very slow CO products in low rotational levels, ascribed to intramolecular abstraction

by a roaming methyl group which will be described in detail later in the Results section.

A fascinating recent development was reported in a theoretical study of the ground state decomposition of a series of alkanes, propane to neopentane, by Harding and Klippenstein [21]. Two key findings result from this investigation, (1) roaming radical pathways exist with barriers roughly 1 kcal/mol below the lowest bond fission asymptote in all cases, and these lead to exoergic abstraction pathways, giving closed-shell products, and (2) the roaming minimum energy paths may be divided into two classes; one, Woodward-Hoffmann-allowed, involves an inversion of one of the radicals along the intrinsic reaction coordinate, while the other, Woodward-Hoffmann-forbidden, does not. The calculations suggest that for smaller radicals, the former case applies, while for larger systems, the greater dispersion interaction relative to orbital phase contribution in the saddle point region relaxes this constraint. It will be very interesting to see experimental verification of these observations. However, given the nature of these reactions, the question arises: Just how relevant is the MEP in these reactions, anyway? This is a point of some controversy.

We have so far discussed roaming dynamics in closed-shell systems. Can radicals exhibit roaming dissociation dynamics? There are several recent examples worthy of note. A joint theoretical and experimental study of allyl radicals by Chen *et al.*[22] reported that the H migration channel shows a pathway dynamically similar to the roaming mechanism. Photodissociation of the allyl radical was shown to have three H migration channels producing C_2H_2. Two of them were classified as conventional channels, taking place at lower energies via tight TSs. The third channel clearly involved formation of $H_2CC: + CH_3$ at much higher energy. Although this did not take place via an intramolecular abstraction, it resembles roaming in that it involves a distinct pathway to the same products that becomes important at higher energy owing to a loose TS.

Another radical that shows strong evidence of a roaming decomposition pathway is nitrate, NO_3, which is an important atmospheric intermediate [23]. This system can dissociate to $O_2 + NO$ and $O + NO_2$ in the visible region. However, the molecular products are

only seen at energies below, but within 250 cm^{-1}, of the simple bond fission threshold [24]. Above that threshold, only O + NO_2 is seen. Simply on the basis of the discussion above, this alone strongly suggests a roaming mechanism involving near dissocation to O + NO_2, followed by intramolecular abstraction leading to O_2 formation. Recent imaging results from North and co-workers[23] show that the O_2 product is formed in vibrational levels up to $\nu = 9$, entirely consistent with intramolecular abstraction at long range as in formaldehyde and acetaldehyde. In a sense, the nitrate radical case may be seen as representative of another class of roaming events, what we will term roaming-mediated isomerization, exemplified by nitromethane dissociation. Nitromethane was found to give both CH_3 + NO_2 and CH_3O + NO in infrared multiphoton dissociation experiments [25]. The latter products were ascribed to the isomerization $CH_3NO_2 \rightarrow CH_3ONO$ followed by decomposition of the nitrite, and the energy of the isomerization barrier was estimated to be 55.5 kcal/mol (∼5 kcal/mol below the simple bond fission asymptote) based on the observed branching. However, numerous theoretical and experimental investigations over the years failed to identify a suitable isomerization pathway, so that by 2003, M. C. Lin and co-workers entitled their investigation of the situation[26] "Nitromethane-Methyl Nitrite Rearrangement: A Persistent Discrepancy Between Theory and Experiment". Theoretical methods consistently found TSs that were both above the bond fission threshold and too tight to account for the substantial branching that was seen experimentally. By 2009, in light of the roaming reports on other systems, Zhu and Lin had found a new roaming-like TS (see Figure 1.6) within 1 kcal/mol of the bond fission energy [27].

This TS contrasts with the tight isomerization barrier about 10 kcal/mol higher in energy. The key characteristic of the surface shown in Figure 6 is that there are similar energies for the RNO_2 and RONO bonds; this will be the case quite generally for many nitro compounds, suggesting that this roaming-mediated isomerization may be an important aspect of the decomposition of energetic materials. Other systems that possess energetically similar isomers with low dissociation thresholds may well show similar roaming-mediated isomerization. Our

investigations on this topic began with nitrobenzene photodissociation and will be discussed in detail later in the Results section.

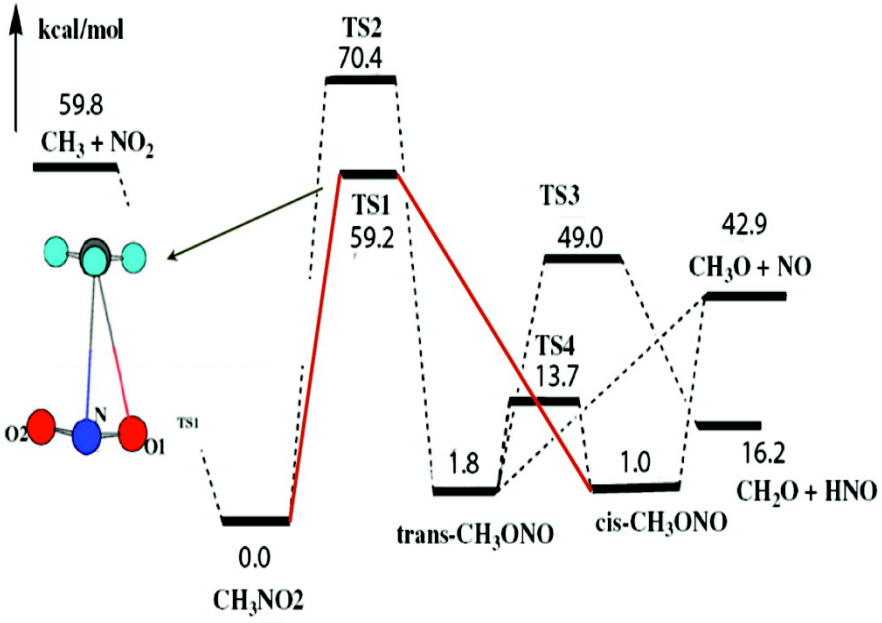

Figure 1.6: Potential energy diagram for nitromethane showing roaming like isomerization TS. The roaming-mediated isomerization pathway is indicated by red lines. Adapted with the permission from R. Zhu *et al*, *Chem. Phys. Lett.* , 478, 11 (2009) ©Elsevier

1.3 Angular Momentum Polarization

Angular momentum polarization is an often measured vector property using ion imaging techniques. These vector correlations provide a great deal of information regarding the excited state symmetry, photodissociation dynamics, the shape of potential energy surfaces and the lifetime of the photodissociation events. Consider a molecule dissociated using a linearly polarized light. The angular distribution is given by [28]

$$I(\theta) \propto 1 + \beta_2(\cos\theta) + \beta_4(\cos\theta) + \beta_6(\cos\theta) + ... \tag{1.4}$$

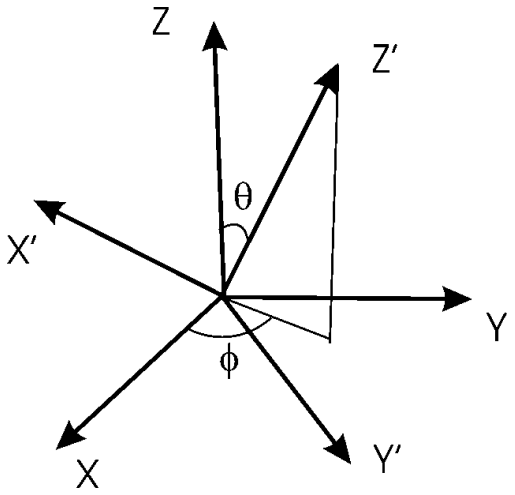

Figure 1.7: Laboratory and molecular reference frame. Adapted with the permission from A.G. Suits *et al*, *Chem. Rev.* , 108, 3706 (2008) ©ACS

Another important vector correlation is the relationship between the photofragment recoil velocity v and the angular momentum j of the photofragments. This property referred to as the $v-j$ correlation can be used to unravel the atomic orbital polarization of the photofragments. Indeed, numerous experimental and theoretical studies have been carried out in this regard, among them the work done by the Suits group, Zare group and Vasyutinskii and coworkers can be highlighted [29–34]. These studies provide great insight into the photophysics governing the events of the photofragment dissociations, including non adiabatic dynamics and coherent dissociation mechanisms. Other parameters are inroduced (analogus to β) to discribed the orientation and electronic alignment of the generated photofragments[35].

Chapter 2

Experimental Methods

2.1 General overview

Our investigations of unimolecular processes require knowledge of the energy, the states of the final products and their speed and angular distributions (momenta). Unimolecular photodissociation can be described in the following way.

$$AB_{(e,v,j)} + hv \rightarrow A_{(e,v,j,mj)} + B_{(e,v,j,mj)} + KE \tag{2.1}$$

Where e, v, j , mj are the electronic, vibrational rotational , and angular momentum quantum numbers of the reactant and the products, and KE is the kinetic energy release during the photochemical event. Measuring the quantum numbers and energy of each product involves a complicated array of experiments, therefore for simplification, a series of controlled experiments can be carried out. Many of the experimental techniques involve measuring the velocity of the state-selected fragments created during the reactions. Understanding the direction of various products scattered after a photochemical event with respect to the laboratory frame is referred as the measuring the recoil velocity of the products. In this dissertation we focus on investigation of unimolecular photodissociation dynamics measuring the velocity of the state-selected products. We applied an ion imaging approach combined with time-of-flight (TOF) method to obtain the velocity of the desired product and using the conservation of linear momentum and the energy, the velocity and the translational energy

of the co-product can be calculated.

To make it less complicated, the reactants are prepared in known or well-defined states. For this purpose, methods based on supersonic expansions are used to generate reactants with well-defined initial velocities.[36] This is achieved by seeding the reactants in a rare gas and the collisions between the molecules cause the internal energy of the molecules to decrease drastically leaving only a few internal degrees of freedom excited. This helps to define the total excitation of the molecules after absorbing a given amount of energy. Of course the next obvious question is how to detect these products state-specifically. Indeed, the subsequent developments in the laser performances especially tunability and the high resolution helped to detect these state-resolved products using multiphoton ionization methods. Here we applied resonance the enhanced multiphoton ionization (REMPI) technique to excite and ionize the photofragments. Usually the molecules are excited to a resonant state via nhv photons where n is an integer (typically 1,2 or 3) and ionization could be achieved by absorbing another photon. The next two sections consist of a brief introduction to ion imaging technique and our new Doppler-free approach: Masked velocity map imaging.

2.2 DC Slice Imaging Approach

Chandler and Houston first invented ion imaging technique in 1986 [37]. In these types of experiments, one can acquire snap shots of the velocity distributions generated during the photochemical events. In a typical ion imaging experiment, molecules are supersonically expanded into a reaction chamber and photodissociated by a photolysis laser and ionized by a probe laser. These ions travel in a field free time-of flight on to a microchannel plate (MCP)/phosphor detector. The resulting image can be viewed by a Charged Coupled Device (CCD) camera (figure 2.1)

The resolution of the conventional ion imaging is poor due to the use of homogeneous electric fields so that the dimensions of the ionization region blur the detected image. About a decade after first invented the ion imaging approach, Epink and Parker introduced a new

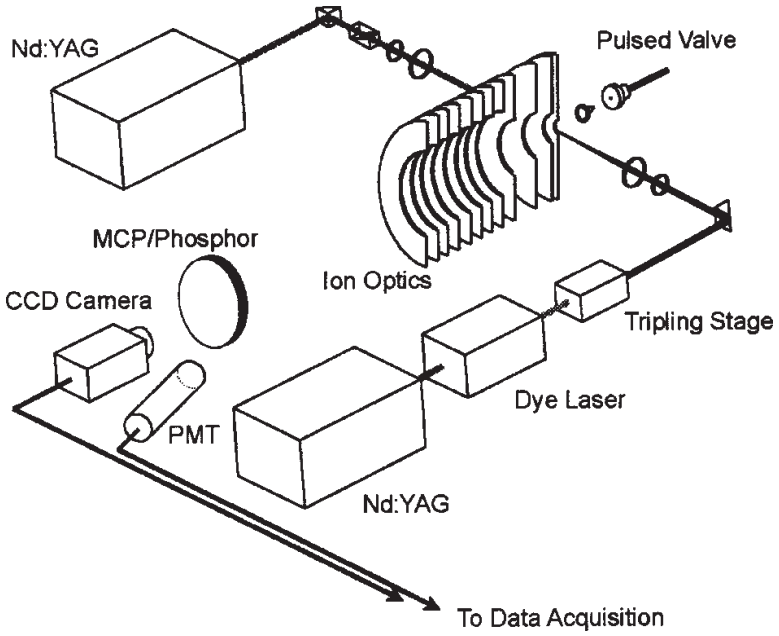

Figure 2.1: Schematic representation of the experimental setup for dc slice imaging. Adapted with the permission from D. Townsend *et al*, *Rev. Sci. Intrum.* , 74, 2530 (2003) ©AIP

variant of ion imaging called velocity map imaging[38]. The resolution of the images was enhanced significantly (a factor of fite or so). Nevertheless this approach of projecting the entire recoil sphere onto the detector has disadvantages such as a requirement of applying mathematical reconstructions methods to obtain the desired three dimensional velocity distribution. To overcome this problem, the Suits Group introduced the dc slice imaging method[39] in which a weak fields in the interaction region allow the ion cloud to stretch along the flight axis, so a short gate pulse is applied on to the MCP detector can selectively extract the central slice of the ion cloud. This method allows to directly acquire the three dimensional image still conserving the high resolution of the velocity map imaging. It is analogous to the 3-D imaging approach developed independently by Kopin Liu at the same time[40].

Our apparatus consist of two chambers, a source chamber and a reaction chamber operated at 1×10^{-5} Torr and 2×10^{-7} torr respectively. The seeded molecules are introduced to the source chamber using a solenoid valve operated at 10 Hz with a pulse duration of

230 μs. The supersonically expanded molecular beam is collimated using a 1 mm skimmer and the molecules enter the reaction chamber where the velocity map ion optic assembly is located. Then the molecules are photodissociated and ionized using the REMPI technique. The product ions are accelerated in a 1 m long field free Time-of-Flight (TOF) onto a dual microchannel plate array of 120 mm diameter, which is coupled to a P-47 phosphor screen. The resulting ion image is viewed by a CCD camera (Sony XC-ST50, 768 $\times$ 494 pixels). The recoding is done by IMACQ Megapixel acquisition program and the analysis was done by using IMAN program[41].

2.3 Masked Velocity map Imaging Approach

Since their first demonstration over 30 years ago, Doppler-free approaches[42–44] have become the methods of choice in virtually all applications where the very high spectral resolving power is needed. When combined with resonantly enhanced multiphoton ionization (REMPI), in addition to high-resolution, extraordinary sensitivity in detection can also be achieved. The intrinsic high sensitivity and high signal-to-noise ratio of REMPI becomes even more enhanced because all species in the detection volume are simultaneously in resonance. In a proof-of-principle experiment, Vrakking *et al.*[45] demonstrated that Doppler-free REMPI is an ultra sensitive probe ($6.8\times$ 103 molecules/cm^3 for H_2) of quantum state distributions of reaction products. In recent years, Doppler-free or reduced-Doppler approaches have been applied to ion imaging studies with considerable success, and a number of variations of these techniques have emerged [46–52].

Here we demonstrate another promising application for Doppler-free REMPI in velocity map imaging experiments. We demonstrate a way to obtain Doppler-free REMPI spectra for spectroscopic studies and state distribution analysis of reaction products with just one laser beam. In all the above-mentioned experiments the Doppler-free spectra are achieved by exposing the molecules under study to a pair of counter propagating laser beams in 2-photon transitions. Taking into account the Doppler shifts caused by the velocity of the atoms or

molecules, the frequencies of the photons appear symmetrically up-shifted and down-shifted in the molecule rest frame. When the pair of counter propagating photons is absorbed the total two-photon energy becomes independent of the velocity, and hence the Doppler effect is canceled. There are a few experimental as well as fundamental complications in the two-photon Doppler-free scheme. Imperfect temporal or spatial overlap of two counter propagating laser beams causes decrease in the detection efficiency[46]. Providing two laser beams instead of one can be time-consuming and a substantially more expensive endeavor especially in case of VUV lasers. On top of that, much higher laser power is needed to drive two-photon transitions compared to the one-photon ones. One laser beam signal as well as accidental one-photon resonances often deteriorate signal-to-noise ratios, but in principle, these can often be dealt with by changing laser beam polarizations [47]. Not all the transitions can be readily accessed and analyzed by two-photon methods due to the fundamental impediments in working out two-photon selection rules.

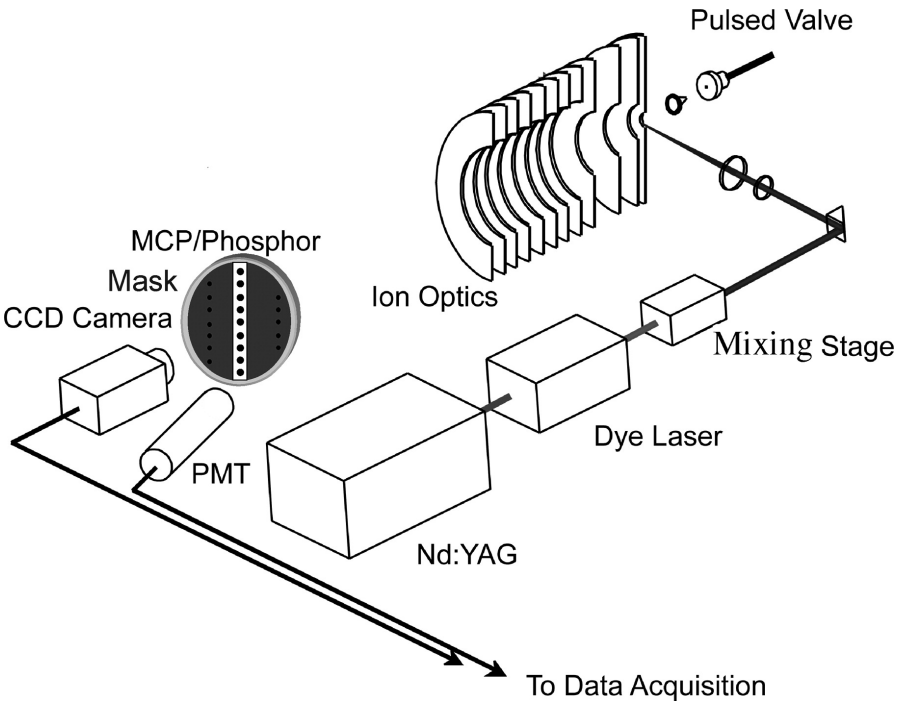

Figure 2.2: Experimental setup for masked velocity map imaging

The approach presented here permits us to overcome all these complications by employ-

ing just one laser beam and restricting detection to only those species with zero velocity component along the laser propagation direction.A mask with a narrow vertical slit through the middle was placed on the outer side of a phosphor screen, in front of a photomultiplier tube (PMT) as shown in the figure 2.2

The width of the slit was varied depending on the UV laser linewidth and velocity of reaction products under study and was chosen to be roughly equal the portion of the Doppler profile corresponding to the laser linewidth to maximize sensitivity without sacrificing spectral resolution. For this purpose, the reaction products of interest were resonantly ionized by a UV laser at the center of the resonance and the mask was placed on the outer surface of the phosphor screen, before the PMT, with the slit size matching the laser-linewidth-determined portion of the Doppler profile in the middle of the phosphor screen.

The benefits of his method are demonstrated in spectroscopic characterization of highly translationally and rotationally excited CO fragments resulting from the 230 nm photolysis of OCS and acetone, yielding substantially improved values of the rotational constants for the B state ($v'' = 0$) of the CO molecule. The resolving power and the state distribution analysis of reaction products are also demonstrated for room-temperature H atoms generated by dissociation of background hydrogen molecules and oxygen atom detected from the 225.6 nm photolysis of ozone [53].

Chapter 3

Roaming Dynamics of Acetone Dissociation

3.1 Introduction

The "roaming mechanism" has recently emerged as a new pathway in unimolecular decomposition [1, 9, 10, 12, 15, 17, 19, 54, 55] as described in the previous chapter (Introduction). In this chapter, we present evidence for an analogous roaming contribution in the ultraviolet photodissociation of acetone through the S_1 electronic state, implying highly vibrationally excited methane as a co-product.The fate of this hot methane product will be considered further below.

$$CH_3COCH_3 \rightarrow (CH_3 + CH_3CO) \rightarrow CH_4 + H_2CCO \rightarrow CH_4 + CH_2 + CO \qquad (3.1)$$

although hot ethane and CO is another possibility initially proposed, discussed further below.

The photochemistry of acetone is among the most thoroughly studied of any polyatomic molecule, with hundreds of studies ranging from classical flash photolysis and nanosecond laser studies[56–62] to a dizzying array of recent femtosecond studies[57, 63–72] as well as extensive theoretical work[69, 73–75]. It is perhaps surprising that a unified picture of its dissociation dynamics has not yet emerged. This is likely a testament to the complexity of the problem and the changing dynamics with excitation energy as key surface crossings are accessed. Nevertheless, some conclusions are widely accepted, and the schematic energy

diagram in Figure 3.1 is useful as we review them.

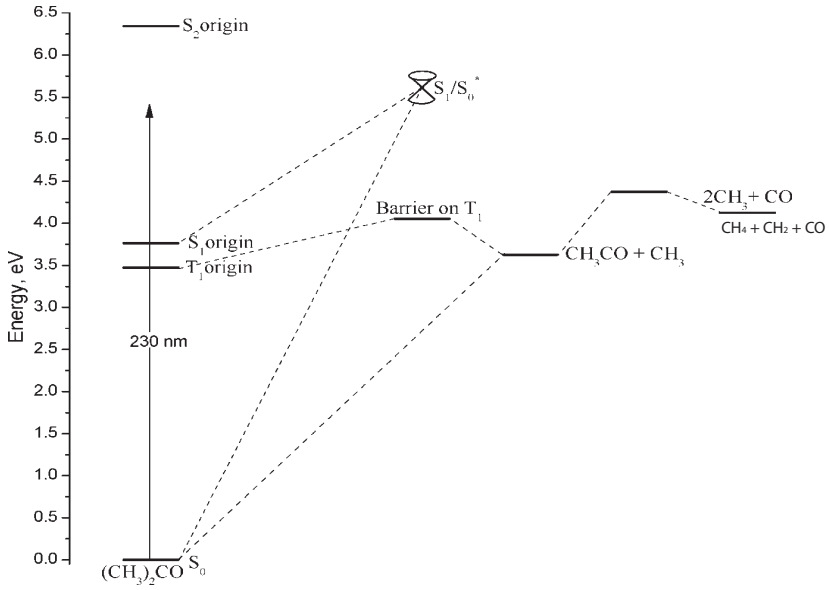

Figure 3.1: Energy diagram for photodissociation of acetone at 230 nm

Excitation in the first absorption band is from a nonbonding oxygen atom orbital to a π^* orbital leading to the S_1 surface which has a pyramidal central carbon. At the long wavelength end of the absorption, dissociation occurs via C-C bond fission following inter-system crossing (ISC) to the triplet surface (T_1), as long as the energy exceeds that of the triplet barrier, 4.05 eV (305.8 nm). At higher excitation energies, e.g., 248 nm, the triplet dissociation (the "T_1" pathway) can leave enough excitation in the remaining acetyl radical for it to undergo secondary decomposition. The acetyl radical itself has an exit barrier of $\sim$ 0.4 eV,[76] so that the translational energy distribution for the CO product of this secondary decomposition peaks away from zero[61]. However, some recent isotopic labeling experiments have complicated this picture somewhat[77]. Mercury lamp photolysis of mixtures of acetone and perdeuteroacetone in a cell at energies below the triplet barrier were found to give rise to a significant fraction ($\sim$25%) of ethane molecules via an intramolecular pathway. The implications of this will be considered further below.

The dissociation dynamics following excitation to S_2 in the intense second absorption band around 193 nm (an n-3s Rydberg excitation) have also received a great deal of attention,[58–61, 66, 70] and much of the discussion is relevant here as well. Pilling and co-workers studied the reaction via end product analysis and time-resolved absorption in a cell at 300 and 600 K.[60] They observed ethane and CO as dominant products, but based on radical scavenging experiments concluded that reaction to produce CO and two methyl radicals accounted for 95% of the overall photolysis, with H and CH_4 elimination accounting about equally for the remaining 5% North *et al.*,[61] using photofragment translational spectroscopy, saw a single CH_3 time-of-flight peak but were able to fit it by assuming two components, one of which was little changed from their result for the 248 nm case. They concluded that the S_2 dissociation also proceeded mainly by internal conversion to S_1, with the S_1 dynamics following the same decomposition path, via the triplet, as at 248 nm. At 193 nm, however, essentially all of the acetyl undergoes secondary decomposition. Zewail and co-workers[70, 78] have argued instead that in this energy region, direct decomposition on S_1 may occur via a transition state that correlates to a linear acetyl radical in the A state (essentially one component of a Renner-Teller pair that is anyway degenerate at the linear geometry). This is the "S_1 mechanism", since championed by Cheng *et al.*[70–72] We should note that the acetyl radical is then believed to relax immediately to the ground state, so that the subsequent secondary decomposition would be essentially the same as that on the T_1 pathway.

One feature of this discussion that has not received much attention is the S_1/S_0 crossing, shown in Figure 3.1 and identified in calculations from Liu et al.[73], Zewail and coworkers[69] and from very recent study by Morokuma and coworkers[79]. In particular, Morokuma and coworkers identified presence of four pathways that the ground state molecules can regenerate from S_1 surface (fig 3.2).

Among those four pathways, S_0/S_1-MXS1 has been identified in the previously reported studies[69, 73]. The other three pathways include S_0/S_1-MXS2, S_1/T_1 and S_0/T_1. Dissocia-

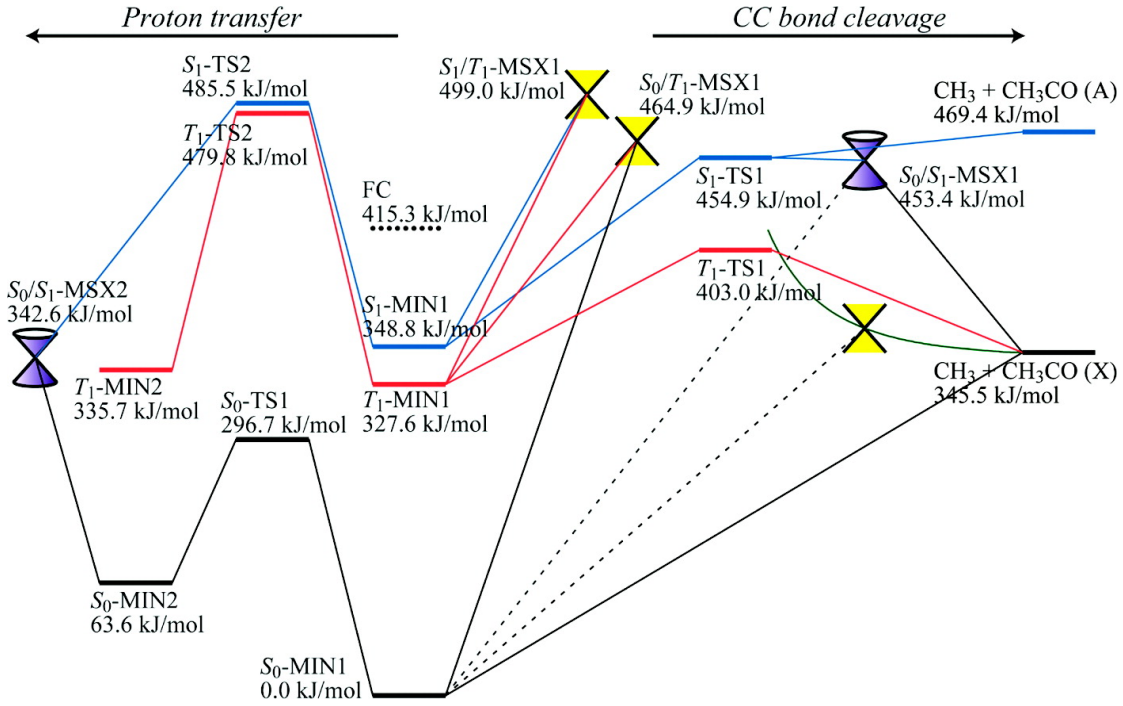

Figure 3.2: Energy diagram for photodissociation of acetone based on the CASPT2/6-31+G*. Adapted from S. Maeda *et al*, *J. Phys. Chem. Lett.*, 1, 1841 ©ACS

tion on the ground-state can then occur without a barrier to give CH_3 + acetyl. The absence of a barrier is key for the roaming intepretation below. In short, the S_1 and S_0 surfaces are mixed at these geometries. Key points in sorting through all these issues are the locations of the CIs and crossings among the relevant surfaces, summarized here: The T_1 barrier is 4.05 eV, the S_1/S_0 CI is 4.76 eV and the S_1 barrier is 5.8 eV. Zewail and co-workers have also explored direct decomposition on the S_2 surface,[75] but the barrier is $\sim$ 7.1 eV, so that pathway is not relevant for dissociation at 193 nm or below.

In this study we present DC slice imaging[39] of state-selected CO molecules following dissociation of acetone around 230nm. The imaging results are combined with Doppler-free resonant multiphoton ionization (REMPI) spectra of the CO product obtained using a new masked velocity mapping approach, to reveal a surprising aspect of acetone photodissociation dynamics in the high-energy range of the S_1 absorption.

3.2 Experimental Section

A supersonic beam, 5% of acetone seeded in Ar, produced by a General valve with the backing pressure of 2 atm and pulse duration ∼200 μs, was introduced into a differentially pumped velocity map imaging apparatus, which has been described elsewhere.[39] The background pressures in the source and detector chambers with the beam on were $\sim 2 \times 10^{-6}$ and $\sim 2 \times 10^{-7}$ torr, respectively. The valve and inlet tubing were kept at 55 $^{\circ}$ C to minimize acetone condensation on the walls and cluster formation in the molecular beam. In order to accomplish a laser line width limited resolution and avoid scanning through broad Doppler profiles of the ground-state CO rotational lines, a two color reduced-Doppler (TCRD) approach was utilized, as previously described [49]. For this purpose, two identical and independently tunable UV laser beams were generated by sum frequency mixing of the third harmonic of seeded Nd:YAG lasers (Spectra Physics, model: Quanta-Ray PRO 250) and a fundamental output of dye lasers (Sirah Laser- and Plasmatechnik GmbH, model: PrecisionScan) pumped by the second harmonic of the same Nd:YAG laser. The UV laser beams were temporally overlapped and sent into the detector chamber in opposite directions. The experiment was designed in such a way that a photon from either laser could cause photolysis of acetone, but only a pair of photons, one from each laser, led to resonant ionization of CO products[49, 80]. For this, the wavelength of one laser was fixed near the resonance and the wavelength of the other was set so that the combined energy of two photons was fixed on a resonance of the Q-branch of the (2 + 1) REMPI B ($\nu = 0$) $^1\Sigma^+ \leftarrow$ (ν" =0) $^1\Sigma^+$ transition. We found that the laser fluence of ∼2 mJ/mm^2 was sufficient to photodissociate acetone and resonantly ionize CO. The resulting ions were accelerated toward a 120 mm microchannel plate detector coupled to a phosphor screen, monitored both with a CCD camera and a photomultiplier tube. The DC slice imaging approach was employed along with our IMACQ Megapixel imaging software, as previously reported,[39, 41] for image acquisition and analysis. REMPI spectra were recorded by collecting the signal from the photomultiplier

tube while stepping the laser wavelength across the B←X transition of CO and measuring the wavelength of the dye laser at each step with a digital wavelength meter (WaveMaster, Coherent, ± 0.1 cm^{-1} accuracy), (0.02 cm^{-1} resolution). During all experiments, extra care was taken to sample only the very early part of the molecular beam expansion where no clusters are expected. One of the products of the photolysis of acetone clusters is an acetone ion with nonzero translational energy. Those ions were detected at the tail of the supersonic beam expansion only when the acetone to Ar ratio was increased to ± 1:1. Under the conditions of the experiment, CO^+ was the only ion poduced to any significant extent, and there was no CO^+ signal when the laser was tuned away from the resonance.

3.3 Results

The images and translational energy distributions of the ground-state CO in various degrees of rotational excitation (J″= 4, 8, 14, 30) produced from the photolysis of acetone at 230 nm are given in Figure 3.3. As can be qualitatively inferred from the images, the available energy is partitioned into CO fragments in two distinct ways.

A rather broad translational energy distribution is seen in a wide range of CO product rotational levels and appears to be more prominent with larger J″. In addition, some images for the first few rotational levels of CO also show a very sharp peak at low translational energy release. However, as J″ increases the broad distribution rapidly becomes dominant. The same bimodal distribution can be observed and characterized on a quantitative basis from the corresponding translational energy distributions (see Figure 3.3). We should note that, in contrast to the customary manner of presenting the total translational energy release, here we show the translational energy for the detected CO fragment only, as the CO may arise from a mixture of two-body and three-body dissociation events. The average translational energies $\langle E_T \rangle$ obtained from the $P(E_T)$ distributions for various rotational levels of CO are given in Table 3.1

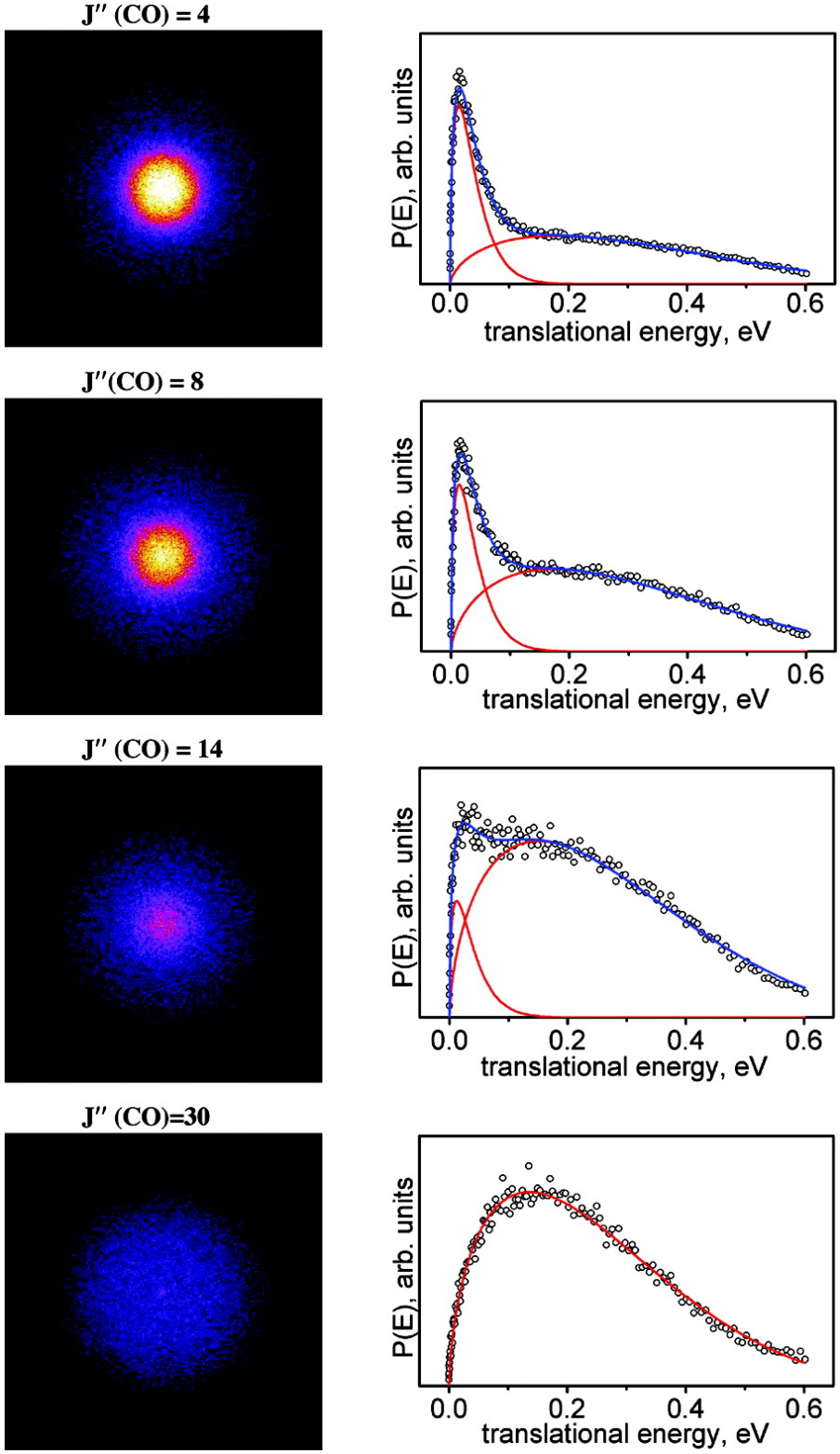

Figure 3.3: DC slice images and translational energy release of the CO fragments from the 230 nm photolysis of acetone

Table 3.1: Characteristics of Bimodal Distribution in CO photofragments

		$\langle E_T \rangle$			
J''	Total eV	broad,eV	Sharp,eV	branching to sharp,%	relative rotational population
4	0.23	0.310(6)	0.038(3)	30	0.031
6	0.24	0.310(6)	0.038(3)	26	0.042
8	0.26	0.310(6)	0.038(3)	19	0.038
10	0.25	0.292(6)	0.038(6)	16	0.036
14	0.26	0.279(6)	-	8	0.027
20	0.27	0.266(6)	-	0	0.022
30	0.25	0.252(3)	-	0	0.014

In order to estimate the branching of the two different energy partitioning modes, $P(E_T)$ curves were fitted to the general expression of the following form[81]

$$P(E_T)_{bimodal} = P(E_T)_{sharp} + P(E_T)_{broad} \tag{3.2}$$

$$= A(E_T)^i(1 - E_T)^j + B(E_T)^m(1 - E_T)^n \tag{3.3}$$

where the power coefficient n was kept fixed for all rotational levels as the tail of the $P(E_T)$bimodal has no contribution from $P(E_T)$sharp. These expressions provide a simple way of decomposing the energy distributions, but we do not mean to draw any direct mechanistic inferences from this fitting or the value of these coefficients. Even though other coefficients (i, j, and m) were varied, the resulting parameters turned out to be almost the same for different J'' as well. Only the weighting parameters (A and B) changed significantly, which is not surprising as the translational energy distributions in this case (e.g., coming off the acetyl barrier) will not be expected to change dramatically with J''. The resulting curves are given in Figure 3.3. The individual fitted distributions are shown in red, whereas the total distribution is given in blue. As can be seen, the simulated curves are well fitted to the experimental data points. The branching for different rotational levels is summarized in the Table 3.1. The overall branching for the ground-state CO (ν= 0) can be obtained if the relative rotational populations are known, which in turn can be estimated from the

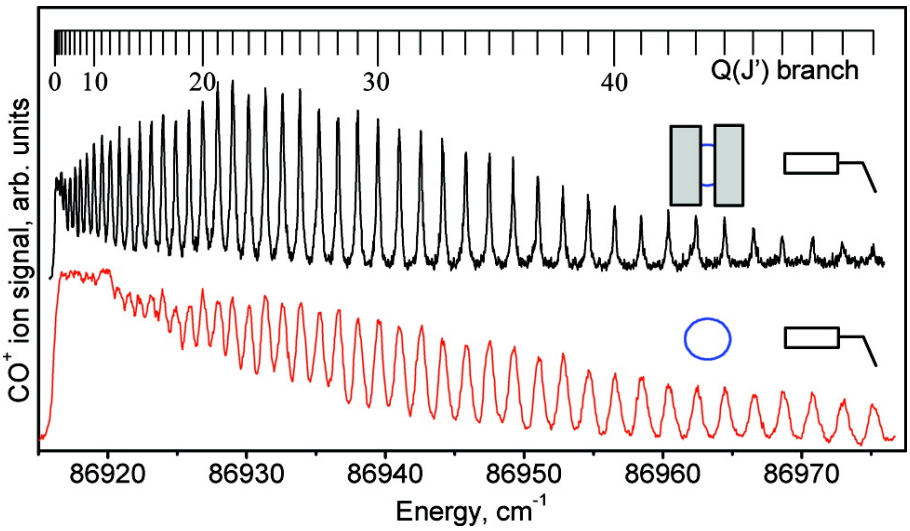

Figure 3.4: 2 + 1 REMPI spectra of the Q-branch of the (ν = 0) $^1\Sigma^+\leftarrow$ (ν'' =0) $^1\Sigma^+$ transition of CO from acetone dissociation at 230 nm. The Dopplerfree spectrum shown in black was collected under the masked velocity mapping conditions. The Doppler-broadened spectrum recorded with the unmasked detector is shown in red

rotational line intensities. For this purpose TCRD REMPI spectra of the Q-branch B←X transition were initially recorded. Surprisingly, the spectra exhibited a very well pronounced sinusoidal ionization probability superimposed on the line intensity profile that precluded further rotational state distribution analysis. More details on this effect will follow. In the meantime, we developed the Doppler-free masked imaging approach described in the previous chapter.[49] For the population analysis, a simple mathematical procedure was then performed to transform the line intensities under masked detector conditions to the unmasked full ion cloud signal. Figure 3.4 demonstrates a comparison between a Doppler-broadened REMPI B←X spectrum of CO acquired with the unmasked detector (red trace) and a Doppler free spectrum recorded with the masked detector (black trace).

The substantially improved resolution permitted us to observe that the spectrum peaks around $J'' = 22$ and allowed us to estimate that about 15% ± 5% of the total CO fragments are produced with the sharp P(E_T) distribution. Here, the uncertainty is estimated based on reproducibility in our fitting procedure and the fact that we have only obtained images on a subset of all the rotational levels.

3.4 Discussion

The broad translational energy release observed together with a wide range of rotational excitation of CO following 230 nm acetone photolysis is dynamically identical to the characteristics of the stepwise dissociation mechanism of bond cleavage in acetone previously studied at 193 and 248 nm. Trentelman *et al.* [82] carried out a thorough investigation of the 193 nm dissociation of acetone using rotationally resolved VUV-LIF excitation spectroscopy to detect CO. They observed considerable rotational excitation peaking around J'' = 22 for ν= 0 of CO, which is in precise agreement with our results at 230 nm. The average translational energy value was determined to be 0.37 ± 0.05 eV by analyzing the Doppler profiles of several rovibronic transitions. North *et al.*[61] also performed a detailed investigation of the 193 photolysis of acetone using photofragment translational spectroscopy with universal detection of photodissociation products. Their average translational energy release value of 0.21 ± 0.03 eV is considerably lower. It should be noted that based on the perceptible deviation in rotational populations of the effusive and supersonic beam results for the J'' (CO) $\langle$ 15 data, Trentelman and co-workers[82] concluded that the excess population in low rotational states may originate from acetone clusters. Hence, it is possible that their translational energy measurements were performed for the J'' $\rangle$15 of CO, although not all of the rotational levels used for the analysis were specified. In any case, their result was a simple fit to Doppler-broadened lineshapes, and the laser line width contribution was significant in that case. Analysis of our bimodal distribution gives an average $\langle E_T \rangle$ around 0.24 eV, which is in good accord with measurements by North and co-workers. It should be noted that in this case comparing the average translational energies at the 193 and 230 nm photolysis is reasonable, as the translational energy release is likely dictated by the exit barrier heights in the primary and secondary dissociation steps, and insensitive to modest changes in available energy.

A question that immediately arises is why this slow component was not seen in the

experiments of North *et al.* One obvious answer is that our result is at 230 nm, while the North result is at 193 nm. However, we believe the dynamics are similar at these wavelengths, so we are not satisfied with this explanation. In fact, the broad component in our distribution is in very good agreement with the 193 nm translational energy distribution North derived for CO, but overall there is strong deviation at the lowest energies, below 0.1 eV where the sharp peak begins to contribute. However, the photofragment translational spectroscopy (PTS) experiments are not sensitive to the slowest products, as they do not scatter far from the beam. The precise low energy limit will depend on the molecular beam velocity and the angles used in the analysis, and this is not entirely clear from the paper. It is thus possible that this slow component was present in the PTS experiments but that data sufficiently close to the beam was not recorded and fitted to reveal this contribution to the translational energy distribution. We should note that detection of m/z = 28 in the PTS experiments is extremely challenging, and the signal-to-noise achieved in that work already quite remarkable. Finally, although our average translational energy release is close to that given by North, it is somewhat larger, while the slow contribution would be expected to make it smaller. However, our result is for CO (ν= 0) only, while theirs includes small contributions from higher vibrational levels, likely lowering the overall average.

Even though the stepwise dissociation mechanism has been previously studied in great detail, the sharp P(E_T) distribution detected for CO with low rotational excitation has not been reported. The remainder of this discussion will be focused on identifying dissociation pathways that can lead to the low-J CO product with low, sharply peaked translational energy release.

In order to address the possibility that the bimodal distribution of the CO products originates from the dissociation of acetone clusters, the dependence of the P(E_T) curves on nozzle temperature was examined. Figure 3.5 shows translational energy release at J''(CO) = 5 for the two sets of experiments differing only in the temperature of the inlet tubing and nozzle. The two P(E_T) distributions are almost identical, implying that the contribution

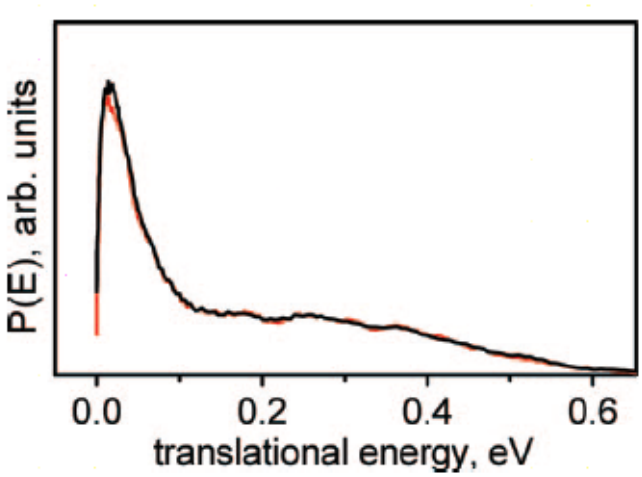

Figure 3.5: Nozzel temperature dependence of the P(E) distributions for CO ($J'' = 0$) Experiments in which the temperature of the inlet tubing and nozzel were kept at 373 and 323 K are plotted correspondingly as black and red lines

from the clusters is negligible. In general, the insensitivity of the observed distributions as the beam conditions were varied in the vicinity of that employed in the experiment further support the notion that these are monomer results.

An alternative source of the slow CO might be either a synchronous dissociation or unusual dynamics in the stepwise dissociation. For the former, based on momentum conservation we can readily estimate the translational energy imparted to the two methyl radicals. If we assume they depart simultaneously at the equilibrium bond angle for acetone, we find a translational energy of 0.065 eV in each methyl, also implying a total internal excitation of 6.3 eV in the methyl fragments. Although kinematically feasible, of course, there is no obvious mechanism to give rise to the simultaneous dissociation to highly vibrationally excited methyl radicals. As an alternative liming case, we can consider dissociation to ground-state methyl radicals and estimate the bond angle necessary to momentum match to CO. We find an angle of 96.8°, again calling for implausible dynamics rather difficult to justify. Finally, we can imagine stepwise dissociation with peculiar dynamics in the secondary dissociation causing the CO to be scattered back to the acetone center of mass, and in low rotational levels. Although it is possible to imagine this happening in some instances, it is very dif-

ficult to conceive of a reason for a distinct population of these events to happen with high probability.

As mentioned in the Introduction, recent comprehensive theoretical study by Morokuma and coworkers [79] propose a new mechanism to dissociate on the triplet surface. After the ISC from S_1 to T_1 the molecules may undergo dissociation on the triplet surface with a barrier of 4.97 eV producing a linear acetyl radical in the A state. Is the bimodal distribution in CO fragments then a sign of these two possible dissociation mechanisms: S_1 and T_1? In short, the answer is no. Given that the linear acetyl radical in the first electronically excited-state quickly relaxes to its ground state, as argued by Morokuma and co-workers, the secondary decomposition fragments do not preserve memory of their S_1 or T_1 parentage. Therefore, the CO fragments from both mechanisms will have very similar energy partitioning, and no bimodal distribution is anticipated.

Another possible explanation that may account for the sharp $P(E_T)$ involves dissociation on the ground-state surface. According to Morokuma and coworkers [79] there are four possible ways that the ground state molecules can be regenerated from the S_1 state (fig 3.2). One pathway could be S_1 to S_0 transition followed by T_1 to S_0 transition (green curve in the Fig). The second one is S_1 to S_0 transition via S_0/S_1-MSX1 which is also reported by by Liu *et al.*[73]. The next pathway could start after the photon transfer via S_1-TS2, the molecules can undergo S_1 to S_0 transition through the CI of S_0/S_1-MSX2. The final possibility is the S_1 to T_1 transition followed by a T_1 to S_0 transition through the CI of S_0/T_1-MSX1. The dissociation on the ground-state is quite distinctive in that it occurs without a barrier to give CH_3 + acetyl. This is a necessary precondition for "roaming" dynamics. Given the barrierless dissociation, it is quite common for the system to attain a condition where there is almost but not quite enough energy in the reaction coordinate for radical dissociation. The methyl radical can then explore a wide flat region of the potential energy surface. This "near dissociation" behavior of CH_3 radical may then eventually result in the intramolecular abstraction via two possible pathways. The more likely pathway is the methyl group abstract

a H atom from CH_2CO to produce vibrationally excited methane and CH_2CO which will eventually produce CH_2 + CO. The other possibility is the abstraction of the methyl group from CH_3CO radical to give excited ethane with CO. Both of these pathways follow the roaming mechanism.

The resulting CO fragments convey these distinct signatures of roaming as seen in the formaldehyde and acetaldehyde systems: very little translational energy release, low rotational excitation and high internal excitation of cofragments, which can be inferred from the $P(E_T)$ distributions if they can be resolved. For such complex molecules as acetone, we clearly do not expect to resolve the internal state distribution in the ethane or methane cofragmenst as we do for H_2 in the formaldehyde case. However, other characteristics of the CO energy partitioning in acetone dissociation are dynamically analogous to those observed in photolysis of formaldehyde and acetaldehyde via roaming[1, 12, 15, 18], making roaming of methyl radical to give highly excited photoproducts, we believe, the most plausible explanation for the observed bimodal distribution of CO in acetone dissociation at 230 nm. An alternative ground-state dissociation pathway would be molecular decomposition via a three-center transition state (TS). To our knowledge, no such TS has been identified theoretically, although it is reasonable to assume one exists. However, such a TS leading to closed shell products and CO products would very likely have a high barrier, so the CO product would be expected to show high translational energy and high rotational excitation, inconsistent with what we see here.

There is perhaps additional support for this picture in the cell experiments involving isotopic mixtures discussed in the Introduction [77]. Those experiments, showing quite clear evidence for intramolecular ethane production following acetone dissociation in the near-ultraviolet, raise a number of interesting questions. The studies were conducted at energies below the threshold for triplet dissociation. In this case, it is possible that dissociation occurs via less efficient coupling to the groundstate than via the CI discussed above, perhaps via the triplet. Production of methyl radicals can then lead to intermolecular ethane formation as

assumed by Pilling and co-workers[60]. However, roughly one-fourth of the ethane produced in the Russian study was attributed to an intramolecular reaction. In this case, it could be either by dissociation via a three-center transition state as mentioned above, or by a roaming mechanism as we have suggested. Although a TS pathway is certainly plausible, we are inclined to favor a roaming explanation in this case as well. The energy dependence shown in the formaldehyde system[9, 12], and the dominance of roaming in acetaldehyde[15], suggest that when it is possible, the larger A-factor for the associated radical channel serves to favor roaming over the dissociation via the tight molecular TS. However, at this point it is little more than speculation concerning the results in the near UV. At 230 nm, however, our results bear the clear sign of roaming in the CO quantum state-specific translational energy distributions.

3.5 Conclusions

DC slice imaging has been employed to study the photodissociation dynamics of acetone at 230 nm, with detection of the CO photoproduct via the B ($\nu = 0$) $^1\Sigma^+ \leftarrow$ ($\nu'' = 0$) $^1\Sigma^+$ transition. A bimodal translational energy distribution observed in the CO fragments points to two distinct dissociation pathways in the 230 nm photolysis of acetone. One pathway results in substantial translational energy release ($E_{ave} \approx 0.3$ eV) along with rather high rotational excitation (up to $J'' = 50$) of CO, and is attributed to the thoroughly investigated stepwise mechanism of bond cleavage in acetone. The other dissociation pathway leads to rotationally cold CO ($J'' =$ 0-20) with very little energy partitioned into translation ($E_{ave} \approx 0.04$ eV) and in this way it is dynamically similar to the recently reported roaming mechanism found in formaldehyde and acetaldehyde dissociation. We ascribe the second dissociation pathway to an analogous roaming dissociation mechanism taking place on the ground electronic state following internal conversion. For acetone, this would imply highly vibrationally excited $CH_4 + CH_2$ or C_2H_6 as co-products of rotationally cold CO. We estimate that about 15% of the total CO fragments are produced through the roaming pathway.

Rotational populations were obtained using a new Doppler-free method that simply relies on externally masking the phosphor screen under velocity map conditions in such a way that only the products with no velocity component along the laser propagation direction are detected.

Chapter 4

Roaming Mediated Isomerization of the Photodissociation of Nitrobenzene

4.1 Introduction

Nitroaromatics are well-known energetic materials. Their importance has led to extensive studies of their decomposition mechanisms, in particular for nitrobenzene, a prototype molecule of this sort. They have been studied using pyrolysis in static cells[83–88] and in molecular beams using ultraviolet excitation from 193 to 280 nm, with detection of the photoproducts using resonance- enhanced multiphoton ionization (REMPI), laser-induced fluorescence (LIF) and vacuum ultraviolet (VUV) photoionization[89–92]. For nitrobenzene, three major channels are found:

$$C_6H_5NO_2 + h\nu \rightarrow C_6H_5 + NO_2 \qquad channel\ 1 \qquad (4.1)$$

$$C_6H_5NO_2 + h\nu \rightarrow C_6H_5ONO \rightarrow C_6H_5O + NO_2 \qquad channel\ 2 \qquad (4.2)$$

$$C_6H_5NO_2 + h\nu \rightarrow C_6H_5NO + O \qquad channel\ 3 \qquad (4.3)$$

The NO_2 channel (1) is dominant at high energies, but the NO channel (2) makes up a significant fraction, with a branching ratio of 0.4 at 266 nm [91]. Although the importance of this isomerization has long been recognized, the mechanism has not been clearly elaborated. In this Article we explore this channel by studying NO production from the ultraviolet dissociation of nitrobenzene and see that "roaming-mediated isomerization" plays a key role.

Roaming reactions, as discussed in the previous chapter,[2, 15, 93] are a newly identified class of reaction, first clearly demonstrated in formaldehyde dissociation, but now believed to be quite general[94]. They involve near-dissociation to radicals followed by intramolecular abstraction, giving closed-shell products with characteristic internal state distributions typical for radical radical abstractions. For example, in the previously studied dissociation of NO_3, evidence strongly suggests[23] that a partially dissociated oxygen atom "roams" around NO_2 before abstracting one of its oxygen atoms to form O_2. Such studies of NO_3 decomposition, as well as those of roaming in CH_3NO_2 decomposition[26], suggest that this may also play a role in nitroaromatic chemistry.

There have been several previous studies on nitroaromatic decomposition, but a clear picture is yet to emerge. Other researchers have carried out photolysis studies on nitrobenzene between 220 and 320 nm and obtained the rotational spectrum of the NO products using LIF at 226 and 280 nm [89, 90]. Rotational temperatures were found to be 3,700 K and 2,400 K, respectively, and the dissociation was attributed to internal conversion (IC) to the ground state followed by isomerization to phenyl nitrite, with dissociation then either to phenoxy and NO or phenyl and NO_2. The phenoxy product was also found to dissociate further into CO and C_5H_5. Yet other researchers found an isomerization transition state on a natural bond potential energy surface using G2M and G3B3 theoretical methods [95]. The dissociation energy for the CN bond was found to be 75 $kcalmol^{-1}$ and the transition state leading to isomerization to phenyl nitrite was 65 kcal/mol. Using density functional theory, similar energetics of 71.2 $kcalmol^{-1}$ for the CN bond dissociation and 63.7 $kcalmol^{-1}$ for the transition state were determined[96]. When studying o-nitrotoluene dissociation using REMPI, a similar but non-Boltzmann like rotational distribution of NO was found[97]. One group also examined stationary points for o-nitrotoluene and found a much more complicated energy landscape, including the elimination of H_2O to form $C_6H_4C(H)ON$ [98]. Their modeling of pyrolysis suggested that loss of H_2O dominates below 1,000 K and NO_2 dominates above.

More recently, a combined experimental and theoretical work was carried out by Ni and co-workers that examined photodissociation of both nitrobenzene and o-nitrotoluene at 193, 248 and 266 nm [91]. Following ultraviolet photodissociation, product yields were determined as well as translational energy distributions using VUV ionization and multimass detection of the ions. The major channels for both molecules were NO and NO_2, with minor contributions of oxygen atom production for nitrobenzene and an OH channel for o-nitrotoluene. Of major interest was a bimodal distribution seen in the NO product channel, with a low energy component peaking near zero translational energy and a high-energy component near 40 $kcalmol^{-1}$. The higher energy feature was more apparent at higher dissociation energies. Theoretical calculations found a transition state leading to isomerization at 57.9 $kcalmol^{-1}$ and CN bond dissociation at 76.3 $kcalmol^{-1}$ for nitrotoluene, and similar numbers as before for nitrobenzene of 61.1 $kcalmol^{-1}$ and 74.1 $kcalmol^{-1}$, respectively (isomerization and CN fission, respectively). The authors used this to justify the difference between the two bimodal translational energy distributions as the splitting of the two peaks is 22 $kcalmol^{-1}$ and 30 $kcalmol^{-1}$ for nitrobenzene and nitrotoluene, respectively.

They offered two justifications for the bimodal distributions[91]. One was that there are two distinct NO elimination channels on the ground state (one of which produced C_6H_4OH as a co-fragment, in addition to isomerization to the nitrite), and the other was the possible existence of an NO elimination channel from a triplet excited state that competes with the fast IC to the ground state. The authors, however, noted difficulties with both explanations. The $C_6H_4C(H)ON$ product was associated with slow recoiling fragments due to the reduced exothermicity and higher transition state (TS) energy. However, this was not consistent with the observed wavelength dependence of the ratio of the fast and slow components. Furthermore, the calculated rates for C_6H_4OH + NO were several orders of magnitude lower than dissociation via the tight transition state on the ground electronic state. Also considered was a possible role for triplet dissociation, as mentioned above. A tight isomerization transition state was determined on the triplet surface 16 $kcalmol^{-1}$ above the T_1 minimum, suggesting

that much of the ensuing rearrangement energy might be available for recoil, as the triplet nitrite is bound by only 1 kcalmol^{-1}. Faced with this intriguing puzzle of the bimodal translational energy distributions in the NO product of nitroaromatics as reported in the comprehensive paper from Ni and co-workers, and aware of the possible role of a roaming contribution to the reaction mechanisms, we undertook a state-selected direct current (d.c.) slice imaging study to look more deeply into this bimodal distribution and complemented this with high-level electronic structure and rate calculations. In what follows we will focus on the dissociation of nitrobenzene, but our experiments on nitrotoluene are in close accord, as observed by Ni and co-workers.

4.2 Experimental methods

4.2.1 Experimental

A detailed description of the d.c. slice imaging apparatus used in this experiment is described elsewhere[39] and only a brief summary is given here. Samples of nitrobenzene, p-nitrotoluene or o-nitrotoluene were heated between 90 and 95 °C. About 1 atm of argon gas flowed through the heated sample to a pulsed solenoid valve heated to 100 °C that created a supersonic beam of seed ratio 12% into the source chamber operated at $\sim 1\times10^{-5}$ torr. Following passage through a skimmer, the molecular beam entered the main chamber, which was held at a pressure near $\sim 1\times10^{-7}$ torr, and was intersected by one laser beam near 226 nm. In this experiment, the laser pulse excited and dissociated the nitroaromatic molecule, with the resulting NO photoproducts probed with the same laser pulse using (1 + 1) REMPI through the rotational-resolved resonances of the NO $\nu = 0$, A $\leftarrow$ X transition. The laser beam was produced by sum frequency mixing of the third harmonic of a seeded Nd:yttrium aluminium garnet (Nd:YAG) laser with the fundamental output of a dye laser pumped by the second harmonic of the same Nd:YAG laser. The resulting ions were accelerated and detected by a 120-mm-diameter multichannel plate detector coupled to a fast phosphor screen. The ion optics, gate and data collection operated in the d.c. slice imaging

mode. A charged-coupled device camera captured the image, and a photomultiplier tube collected the total ion signal. IMACQ/IMAN megapixel imaging software[41] was used to acquire and analyse the resulting data.

4.2.2 Computational

Calculations were performed by our colleagues M. C. Lin and R. Zhu, and the methods they employed were as follows: The geometric parameters for the critical points on the $PhNO_2$ decomposition potential-energy surface were optimized at the UB3LYP//6-311+ G(3df, 2p) level. Intrinsic reaction coordinate analyses[99, 100] were performed to confirm the connection between transition states and designated reactants, products or intermediates. Single-point energy calculations of the stationary points were refined at the highest G2M (CC1) level[99, 100] based on the optimized geometries. All calculations were carried out using the Gaussian 09 program package[100]. The energy-dependent constants (kE) were evaluated using the flexible transition state approach[101] of the Variflex code[102]. The minimum energy path (MEP) representing the barrierless dissociation process of $C_6H_5NO_2$ $\rightarrow$ C_6H_5 + NO_2 was obtained by calculating the potential energy curve along the reaction coordinate CN bond in $C_6H_5NO_2$, where the CN bond length was stretched from the equilibrium value of 1.477 Å to 4.477 Å with an interval step size of 0.2 Å. Other geometric parameters were fully optimized. The dissociation curve could be fitted to the Morse potential function E(R) = D_e [1-exp(-β(RR_e))]^2, which was used to approximate the MEP path for the variational transition state in the rate calculation. In this equation, R is the reaction coordinate (the distance between the two bonding atoms, CN in this work), De is the bond energy excluding zero-point energy and Re is the equilibrium value of R (1.477 Å). The computed potential energies can be fitted reasonably to the Morse potential function with the parameter β =1.279 Å^{-1} The numbers of states for the tight transition states were evaluated according to the rigid-rotor harmonic-oscillator assumption, and the smaller frequencies in the RTS were treated as free rotors. The LennardJones (L-J) parameters are

taken to have the same values as used in ref. [2]: argon: σ= 3.47 Å, ε/k = 114 K; $C_6H_5NO_2$: σ= 5.0 Å, ε/k = 400 K.

4.3 Results and Discussion

Results for DC slice imaging dissociation of nitrobenzene near 226 nm, with probing of a range of product NO rotational levels, are shown in Fig. 4.1. In these images, dark to light indicates increasing product intensity, and the distance from the centre gives the nascent velocity distribution. Here, we can see a suggestion of the bimodality observed by Ni and co-workers in the state-integrated measurements. The lower probed rotational levels principally show a central globe, whereas intermediate and higher rotational levels clearly show two distinct components.

Using conservation of energy and momentum, we can readily convert these velocity space images into total translational energy distributions (Fig.4.2 (a-d)). Results for the integrated NO distributions from Ni and co-workers at 248 nm are also shown for comparison (Fig.4.2e). These translational distributions verify that there are two components in the NO distributions, and the faster one is more pronounced for higher NO rotational levels. At J = 59.5, the fast component (high E_T) is larger than the slow component by a margin of about 2:1. The low translational energy component is centered in the distributions near 5 kcal/mol. This slow component rises from a ratio of about 1:2 at high J = 59.5 to about 2:1 at the lowest J levels. Lower J levels were examined at J = 10.5, 3.5 and 1.5, but showed no significant difference from the image obtained at J = 29.5.

The results obtained are consistent with the study by Ni and co-workers showing a bimodal distribution of NO photofragments[91]. No significant anisotropy is seen in any of the images obtained, confirming a slow dissociation process that is probably due in part to internal conversion to the ground state. At an excitation energy of 226 nm and using the energies from Ni and co-workers, the total maximum energy release $\sim$ 104 kcal mol^{-}1 for nitrobenzene. Based on the NO rotational constants[103], the maximum total translational

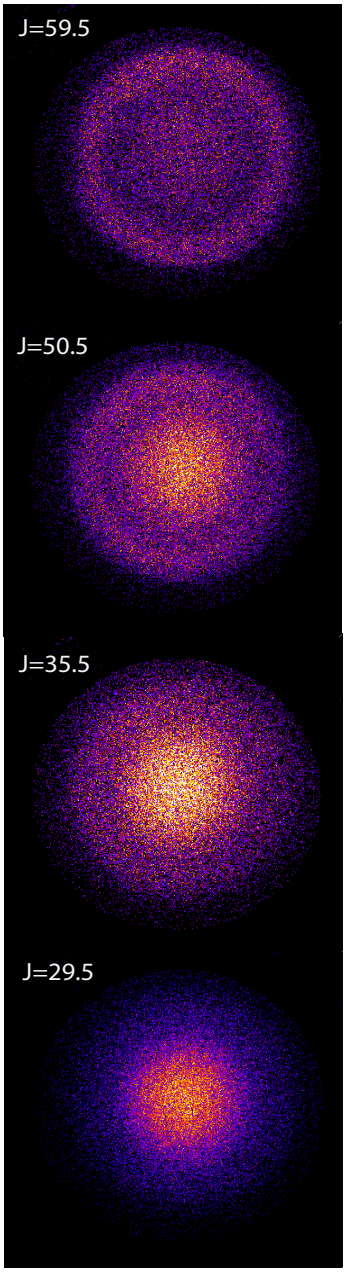

Figure 4.1: Direct current sliced images of NO from the photodissocation of nitrobenzene excitation at ∼226 nm. The NO fragment is probed via a 1+1 REMPI scheme through the NO $\nu = 0$, A $\leftarrow$ X band for the following transitions: P_1 (59.5), Q_1 (50.5), Q_1 (35.5) and Q_1 (29.5). After acceleration down a field-free flight tube, the NO ion cloud impacts a position-sensitive detector timed to record the central slice of the NO mass products. The distance from the center then corresponds directly to the centre-of-mass recoil velocity of the NO. The images show two components: the high rotational levels show more of the fast component, and the lower rotational levels mainly show the slow component.

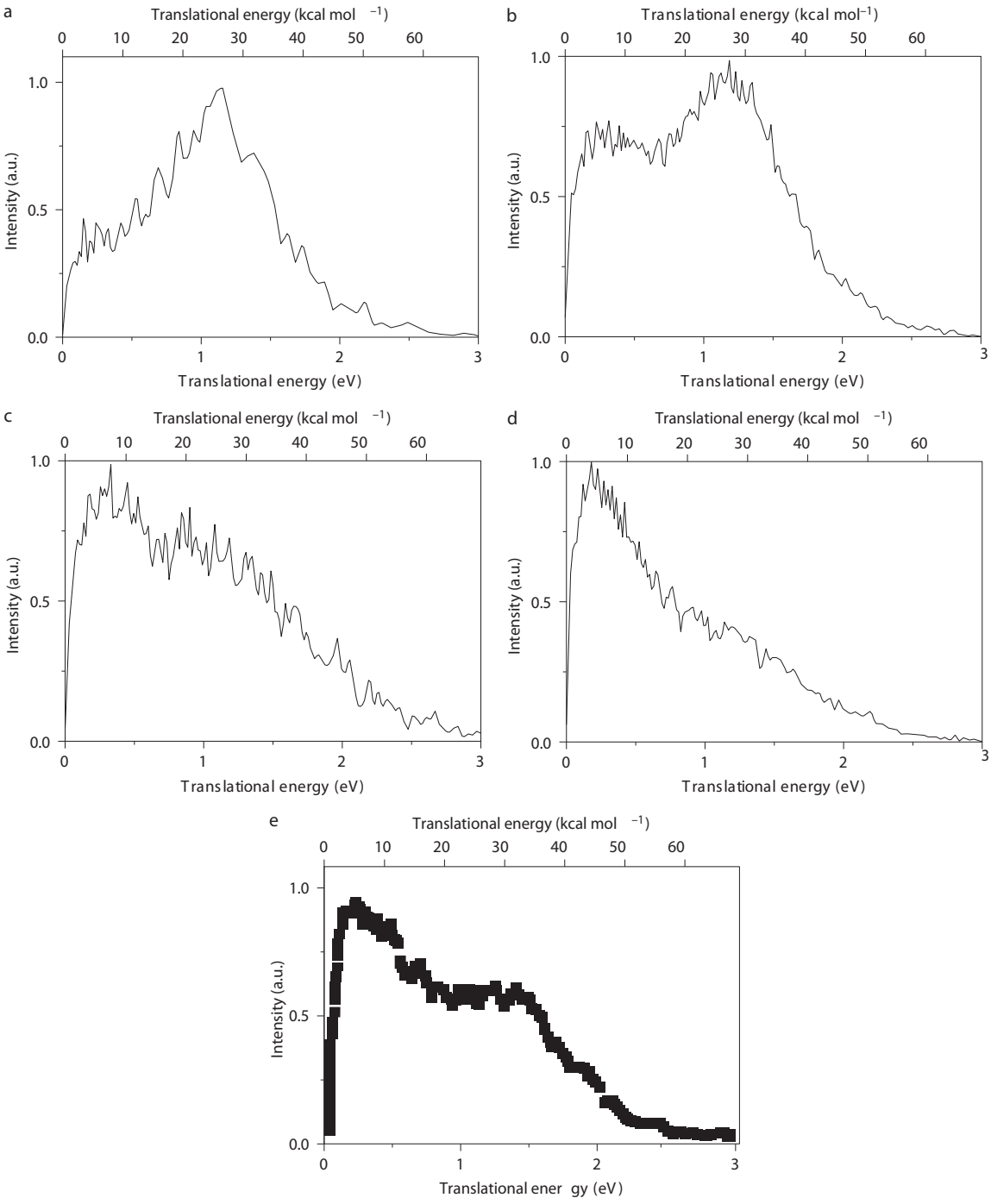

Figure 4.2: Total translational energy distributions derived from the images in Fig.4.1 a-d, Distributions for the indicated rotational level obtained via transitions P_1 (59.5), Q_1 (50.5), Q_1 (35.5) and Q_1 (29.5) (d). e, Total NO translational energy distribution at 248 nm integrated over all NO co-fragments; from ref. [91], © 2007 AIP. From conservation of linear momentum and energy, we convert the NO recoil velocities in Fig.4.1 into total translational energy release between the fragments. The bimodal structure is seen to vary with NO rotational levels

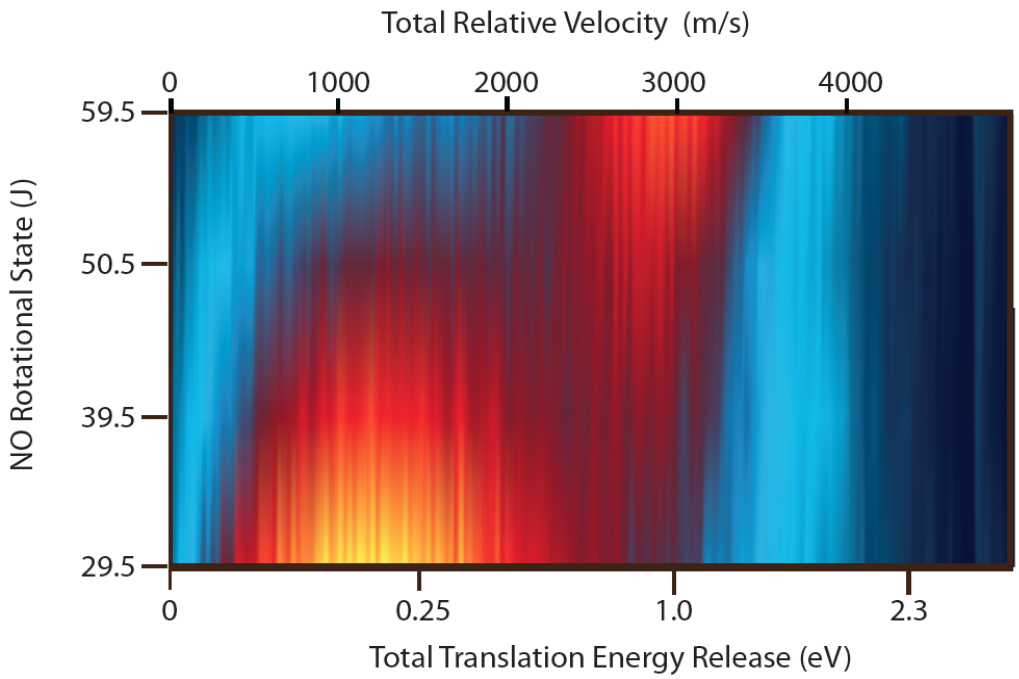

Figure 4.3: State-correlated plot showing NO(J) versus total translational energy or relative velocity derived from analysis of the images. Higher intensity is in red-orange, lower intensity in blue. This plot indicates the correlation of the bimodality in translational energy seen in Fig. 4.2 with the rotational level of NO.

energies allowed for J levels 59.5, 50.5, 35.5 and 20.5 are 87, 92, 98 and 99.4 kcal mol^{-}1, respectively. The translational energy distributions do not show NO fragments out to this energetic limit, which suggests a large amount of rotational and vibrational energy remains in the C_6H_5O counter fragment. These relatively slow fragments are again consistent with early work showing internal conversion distributing large amounts of energy into the internal coordinates as well as the production of CO from secondary dissociation of the remaining C_6H_5O. The images clearly demonstrate that not only does the NO distribution split into two different translational pathways, these two components also have strongly correlated rotational distributions. This is seen very clearly in Fig. 4.3, in which we plot the detected NO rotational level against the total translational energy release for three nitroaromatics (NB, o-NT, p-NT). The strong correlation between the NO rotational excitation and translational excitation is quite clear: the bright feature at the lower left is the slow, low-J component.

Our task is now to identify the underlying pathways that can give rise to the following key observations: (i) there is a very slow component peaking at 6 kcal mol^{-}1 or less that is largely composed of rotational levels below J = 50.5, and at J = 29.5 it is the main contribution;(ii) there is also a fast component, peaking above 23 kcal mol^{-}1, that begins with rotational levels around J = 35.5, and at the highest probed level (J = 59.5) it is the main contribution; (iii) the distributions are indistinguishable for the three molecular systems studied, although here we focus on nitrobenzene. We might add the wavelength dependence inferred from the results of Ni and colleagues (they argued that the fast component grew in intensity with increasing excitation energy); however, no fitting of the contribution was attempted. It is also clear that the shape of the fast distribution changed somewhat with excitation wavelength. This makes it rather difficult to be quantitative about the wavelength dependence of the branching. Indeed, in the result from Ni and colleagues for nitrobenzene at 266 nm, although only one feature is seen, it peaks at very low energy but extends all the way to 55 kcal/mol, consistent with the fast peaks at other wavelengths. Nevertheless, it is at least qualitatively apparent that the high-energy component increases with increasing excitation energy,

To gain further insight into possible pathways to account for these observations, our collaborators M. C. Lin and R. Zhu revisited the ground-state potential energy surface at the G2M(CC1// UB3LYP/6-311 + G(3df,2p) level of theory, seeking in particular to characterize any possible roaming transition-state (RTS) region that may play a role. The results are summarized in Fig. 4.4.

If the energy of the separated phenyl + NO_2 is taken as the zero of energy, then Zhu and Lin find the tight isomerization TS_1 at 13.9 kcal/mol, largely consistent with earlier theoretical work. However, a roaming-type saddle point region is found at 1.3 kcal/mol and its characteristic structure is shown in Fig. 4.4a. This is typical for a roaming saddle point region: bond distances extend beyond 3.2 Å or more, and energies are within 12 kcal/mol of the asymptotic energy of the corresponding separated fragments arising from

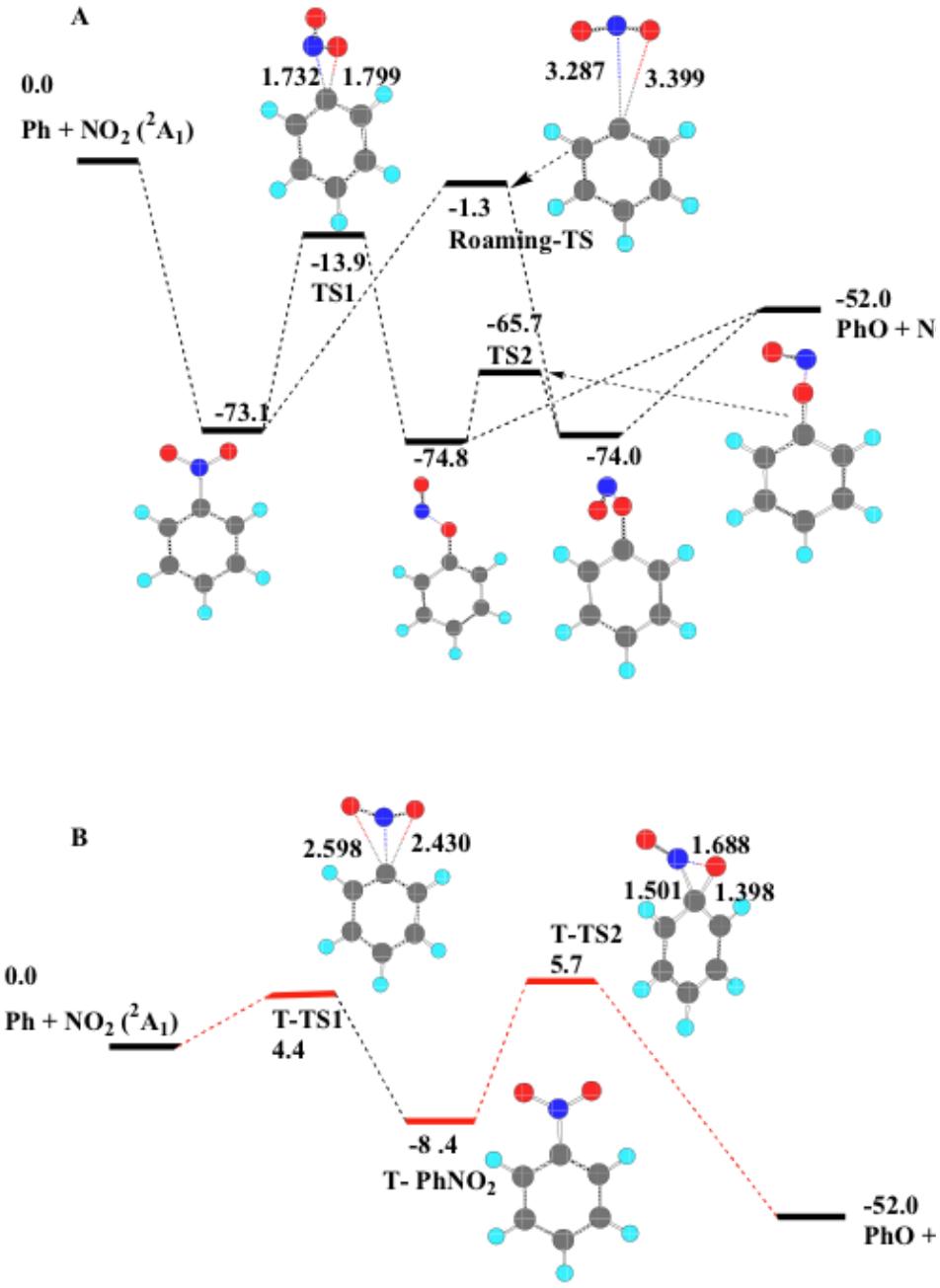

Figure 4.4: Schematic potential surfaces for the ground singlet and lowest triplet states of nitrobenzene. a, Key stationary points on the ground singlet surface for nitrobenzene relevant to NO formation. b, Key stationary points on the T_1 surface for nitrobenzene relevant to NO formation. Oxygen atoms are shown in red, nitrogen atoms in dark blue, carbon in grey and hydrogen atoms in light blue. Red lines are shown on the triplet surface, black lines on the singlet surface. Calculations were carried out by R. Zhu and M. C. Lin. Energy in kcal/mol and bond lengths in $\AA$

simple bond fission. This roaming-mediated isomerization pathway leads to a local minimum of phenyl nitrite that can readily lose NO barrierlessly with an additional 22 kcal mol^{-}1. It should be mentioned that for this large size of system, they can only locate the RTS using the UB3LYP/6-311 + G(3df,2p) method, and at this level, the wave functions are spin-contaminated: the coupled cluster calculations have a T_1 diagnostic of 0.039, which is slightly higher than the proposed maximum value of 0.02. For a similar small CH_3NO_2 system[26], they confirmed the RTS by the CCSD and CASSCF methods; all gave similar structures. The level of electronic structure theory used in this work may only be expected to yield qualitative rather than quantitative results. Determination of the quantitative contribution to the dissociation products from the roaming channel versus the conventional product channels requires a full dimensional calculation on a complete potential surface, which is outside the scope of this work. Nevertheless, these calculations suggest that the probable explanation for the slow component of the bimodal energy distribution is roaming-mediated isomerization.

To further verify that roaming is key to the dissociation pathway giving rise to the low-J, slow NO products, branching ratio calculations were run on the saddle points in Fig. 4.4 by Lin and Zhu. Figure 4.5 presents energy-dependent branching ratios obtained by treating the smaller frequencies as free rotors. The results are quite striking. As shown by the solid black line, the yield of NO products due to the lower-lying, tight transition state decreases sharply at energies only slightly above the threshold for NO_2 formation as alternative pathways take over. Branching to NO production from roaming mediated isomerization quickly increases and reaches a maximum at energies near 15 kcal/mol above the NO_2 simple bond fission (SBF) threshold. We should point out here that we are referring to roaming-mediated isomerization to phenyl nitrite. It will subsequently decompose after some time, but Lin and Zhu have not calculated that lifetime, which will obviously be energy-dependent. The system may or may not linger long at the phenyl nitrite minimum. Simple bond fission giving NO_2 grows with increasing energy, as would be expected for a barrierless reaction, and ultimately

dominates. The conclusion drawn from Fig. 4.5, for the ground electronic state, is that the slow component is indeed due to roaming-mediated isomerization deriving from the CN bond fission channel; however, the fast component is not due to dissociation through the tight transition state following isomerization on the ground electronic state. The predicted rates are simply too low to account for the observed yield, and the wavelength dependence is also inconsistent. Instead, the fast component is probably due to dissociation on the excited triplet state, as suggested by Ni and co-workers[26].

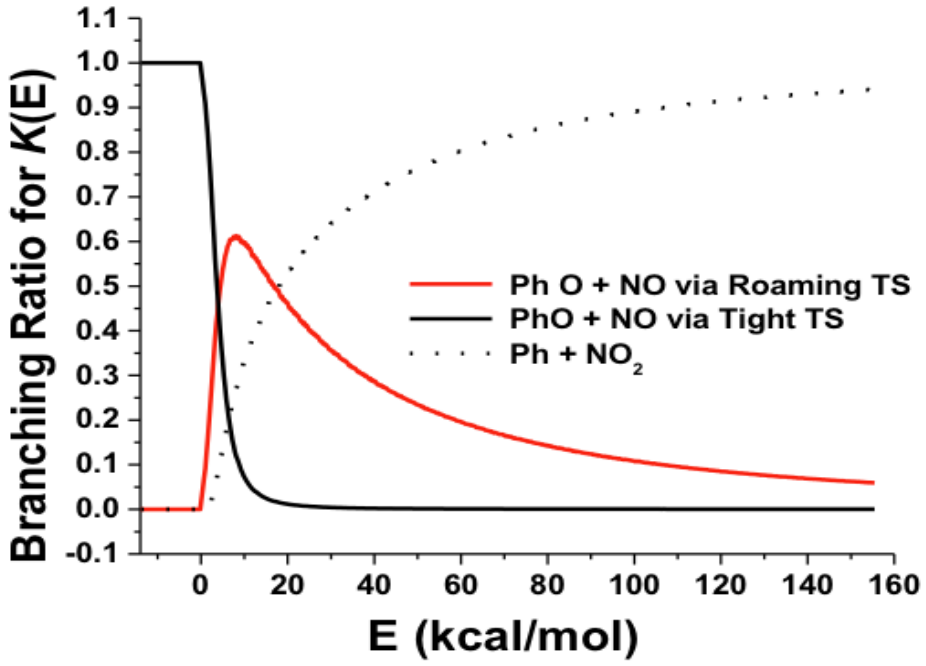

Figure 4.5: Plot of the branching ratio for dissociation of nitrobenzene versus energy relative to the simple bond fission threshold (loss of NO_2). The black curve represents formation of C_6H_5O + NO through the tight transition state, the red curve the yield through the RTS, and the dotted black curve is the SBF pathway: formation of C_6H_5 + NO_2. Calculations were performed with the surfaces shown in Fig. 4.4a.Calculations were carried out by R. Zhu and M. C. Lin. Energy in kcal/mol

To gain insight into this, further calculations of stationary points on T_1 were performed

by Lin and Zhu at the same G2M(CC1)//UB3LYP/6-311 + G(3df,2p) level of theory shown in Fig. 4.4 b. The T_1 minimum is 8.4 kcal/mol below the NO_2 SBF asymptote, and there is a tight TTS_2 5.7 kcal/mol above that, leading directly to C_6H_5O + NO with the release of some 57.7 kcal/mol potential energy, much of which would likely find its way into translation. This would also give rise to impulsive NO rotational excitation, accounting for the greater rotational excitation seen in the fast component. This TTS_2 barrier may also be responsible, in part, for the energy dependence Ni and co-workers reported for the fast component. Energy excess above TTS_2 will increase its reactive likelihood as opposed to decay over TTS_1 to NO_2 or intersystem crossing back to the ground state. In fact, at these energies there are several electronic states that may participate; nevertheless, the uniformity of behaviour among the different compounds suggests that relatively straightforward issues underlie this branching to the high-energy component, rather than subtle, unique features of each surface. They also examined the contribution of the C_6H_4OH + NO channel: the rate-controlling tight transition state of this channel is 2.6 kcal/mol higher than the RTS, the branching ratio lies below 2.6 $\times$ in the energy range of $\sim$ 0-155 kcal/mol and can be ignored. For this reason, it is not plotted in Fig. 4.5. Other higher-energy channels are expected to have even smaller contributions for NO formation. The slow NO component is thus ascribed to barrierless, near dissociation into C_6H_5 + NO_2 products $\sim$14 kcal/mol higher in energy than the tight isomerization saddle point. If insufficient energy is localized into the CN bond, dissociation will not be complete.

The NO_2 and phenoxy fragment will reorient, or roam until they isomerize into the nitrite, at which point far less energy is needed to produce the NO fragments. This is entirely analogous to the formation of O_2 + NO in the nitrate radical dissociation recently reported by North and co-workers[23] and interpreted theoretically by Morokuma and co-workers[104]. Generally, roaming occurs at 3-4 Å, where the chemical bond is essentially broken and the radial anisotropy of the potential may be exceeded by the angular anisotropy, allowing roaming excursion to other reactive portions of the molecule to take place. These

are often highly exoergic radicalradical reactions that take place at long range, giving rise to high vibrational excitation and low rotational excitation in the new bond.

4.4 Conclusions

Roaming-mediated isomerization explains the bimodal NO distribution with low J-low velocity (roaming) and high J-high velocity components (triplet decay). More insight is clearly needed into the triplet pathway, which has been sketched here only vaguely. Infrared multiphoton dissociation would also be very useful to verify that excited-state dynamics are responsible for the fast, rotationally excited fragments. Based on these calculations and on the large yield of NO in the presence of a barrierless pathway (giving NO_2), if the dominant source of NO on the ground electronic state is indeed a consequence of roaming-mediated isomerization, then images from infrared multiphoton dissociation experiments at comparable energies should only contain low-energy, low-J NO fragments. This would offer a very general probe of roaming phenomena.

Chapter 5

Photodissociation Dynamics of Tetrachloroethylene

5.1 Introduction

This chapter presents the study of the dissociation dynamics of tetrachloroethylene using state-resolved slice imaging approach. Tetrachloroethylene (C_2Cl_4, TCE) is an important industrial solvent that has received considerable attention due to its impact on the environment as a soil contaminant and particularly as an atmospheric pollutant[105–109]. Despite its atmospheric impact, its photochemical behavior has not been deeply investigated, although many studies have focused on the ultraviolet (UV) absorption spectroscopy of C_2Cl_4.[110–115] Recently, our laboratory has begun using TCE as a precursor to produce Cl atoms for scattering experiments, owing to its reduced toxicity and reactivity compared to the widely used oxalyl chloride[116]. We here present a detailed investigation of its photodissociation dynamics at two wavelengths, 235 and 202 nm, spanning the first broad absorption band.

Among many theoretical and experimental UV absorption studies reported previously on TCE we will specifically mention only a few of the recently published articles in detail. An *ab initio* study by Arulmozhiraja *et al.*[114] reported the excitation energies and the oscillator strengths for the electronic transitions of TCE. They assigned a $\pi^* \leftarrow \pi$ transition around 6.41 eV as the optically bright state. They were the first to identify and assign $\sigma \leftarrow \pi^*$, $\sigma^* \leftarrow$n, $\pi^* \leftarrow$n vertical transitions with 5.76 eV, 7.91 eV, 7.28 eV excitation energies,

respectively. The $\pi\sigma^*$ is a 1^1B_{1u} state and the lowest energy singlet transition. A recent study by Eden *et al.*[115] reported the vacuum ultraviolet (VUV) spectrum of TCE employing photoabsorption measurements over the range of 3.8 eV -10.8 eV (325-115 nm). Their absorption spectrum, reproduced in Fig. 5.1 , consists of two major bands at low energies and more structured features at higher energies. Considering the previously reported experiments and theoretical calculations, they identified the first low energy structure around 6.2 eV as mainly the singlet valence $\pi^* \leftarrow\pi$ transition. The low-energy shoulder appearing around 5.34 eV was assigned as a π^*(C-Cl)$\leftarrow$ π (C=C) transition. The calculations of Arulmozhiraja *et al.*[114] found the same transition at a slightly higher energy. The π^*(C=C)$\leftarrow\pi$(C=C) transition was associated to the major component of the first absorption band which lies around 5.9 eV. Furthermore, they assigned the features at 6.08 eV and 6.20 eV as the excitation of the fundamental and the overtone of ν_1, C=C stretch.

Previous studies on the UV photodissociation dynamics of mono- and dichloroethylene[117–119] aid in understanding the photodynamics of TCE. Umemoto *et al.*[117] measured the translational energy distribution of Cl and HCl following photodissociation of mono- and dichloroethylene at 193 nm via the $\pi^* \leftarrow\pi$ transition. They found that HCl products were formed in large abundance in vinyl chloride (VC), which they attributed to internal conversion (IC) to a $\pi\sigma^*$ state. In dichloroethlyene, they found a second Cl product channel and claimed it is due to a dissociation on an nσ^* state. Tonokura *et al.*[118] measured the translational energy distribution as well as the angular dependence of the Cl products of mono- and dichloroethylene and found two product channels. High translational energy products were formed with a large anisotropy parameter of 1.0 and a low translational energy channel was formed with a nearly isotropic, statistical distribution. They assigned the two channels to electronic relaxation and dissociation from a $\pi\sigma^*$ state and the ground state, respectively.

This paper, we present a study of the photochemical dynamics of TCE following absorption at 235 nm and 202 nm, chosen to access the $\pi\sigma^*$ and $\pi\pi^*$ transitions, respectively.

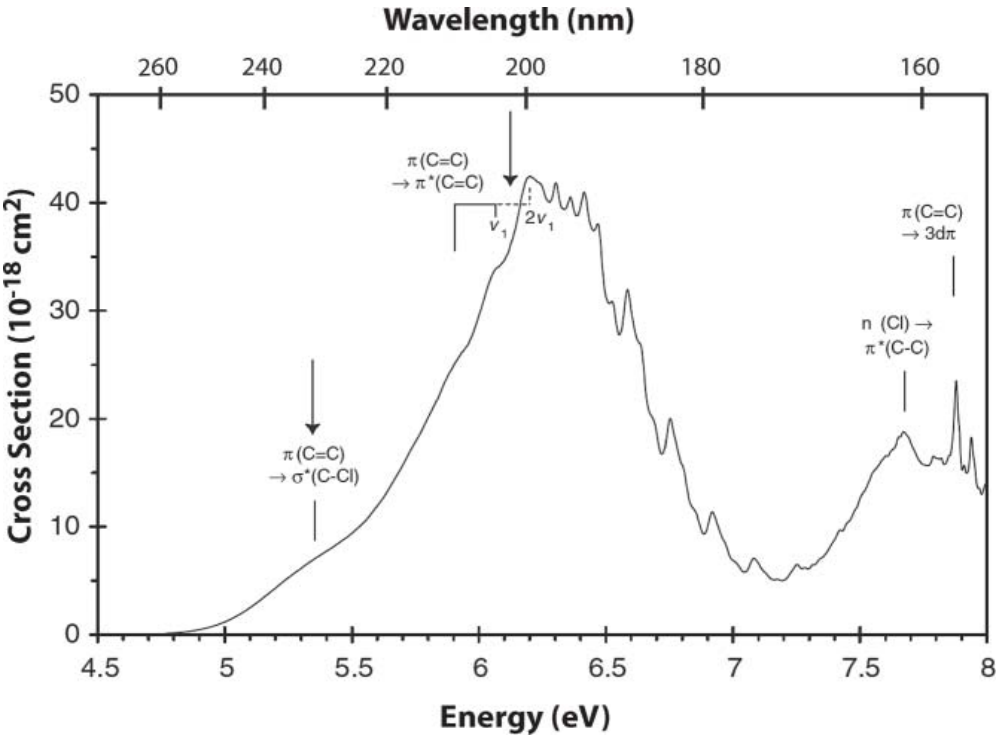

Figure 5.1: The UV absorption spectrum of C_2Cl_4. The arrows denote the two excitation energies used in the current work. Adapted with permission from S. Eden, B. Barc, N. J. Mason, S. V. Hoffmann, Y. Nunes, and P. Limo-Vieira, Chem. Phys. 365(3), 150 (2009). ©2009, Elsevier.

The absorption spectrum of C_2Cl_4 in Fig. 5.1 shows the absorption cross sections are quite large: 6×10^{-18} and 4×10^{-17}cm^2 at 235 and 202 nm, with the latter near the peak of the absorption. We use a two-color reduced-Doppler probe[49] in which two laser beams of distinct frequencies are sent counter propagating into the chamber. One of the two beams is responsible for the photodissociation, while both beams together are necessary for the 2+1 resonance enhanced photoionization (REMPI), which then takes place with enhanced signal-to-noise, and with no need to scan the lasers to encompass the full Doppler profile of the recoiling fragments.

5.2 Experiment

A detailed description of the DC slice imaging apparatus employed in this experiment is described elsewhere[39] and only a brief summary is given here. A pulsed supersonic beam of TCE seeded 5 % in Ar gas with the backing pressure near 1 atm was introduced into the source chamber operated at $\sim 10^{-5}$ Torr using a solenoid valve. Following passage through a skimmer, the molecular beam entered the main chamber, which was held at a pressure near 10^{-7} Torr, and was intersected by two laser beams. In this experiment, tetrachloroethylene was excited and dissociated with the resulting chlorine photoproducts probed using REMPI through resonances of the Cl 4p $^2D_{3/2} \leftarrow {}^2P_{3/2}(84988.480\ cm^{-1})$ and Cl* 4p $^2S_{1/2} \leftarrow 3p^2P_{1/2}(85917.937\ cm^{-1})$ transitions. We employed two-color reduced-Doppler (TCRD) imaging[49] for the both transitions in order to acquire the full ion image without scanning the broad Doppler profile of the Cl atom. For the lower energy transition, we used two tunable UV beams each $\sim 100 cm^{-1}$ on opposite sides of the resonance. The beams were produced by sum frequency mixing of the third harmonic of seeded Nd: yttrium aluminum garnet (Nd:YAG) lasers with the fundamental output of a dye laser pumped by the second harmonic of the same Nd:YAG laser. Typical laser powers of the both beams were $\sim$ 1.2 mJ. One photon from either laser excited and dissociated TCE after which one photon from each of the lasers excited the desired resonance for the REMPI process. We also carried out photolysis at 202 nm using the TCRD imaging technique[49] in a similar manner. For this purpose, we used UV pulses around 282 nm and 202 nm such that the sum of the pulse energies is equal to the total energy of the each transition. We produced 202 nm light by mixing the fundamental output of the dye laser pumped by the second harmonic of the Nd:YAG laser in a beta-Barium Borate (BBO) crystal with the frequency doubled of the output of the same dye laser produced in a potassium dihydrogen phosphate (KDP) crystal after matching the polarizations of the beams using a waveplate. The 282 nm light was produced by the doubling the fundamental output of the second dye laser pumped by

the second harmonic of the Nd:YAG laser. The Cl atoms (^2P_J) were ionized through the same resonances as in the former case, although here the wavelength splitting between the lasers was much larger. The typical powers of 202 nm and 282 nm were ∼1 mJ and 1.5 mJ, respectively. This approach is very sensitive and convenient, in that the molecule is transparent to the 282 nm light, and there is no "probe only" background. The resulting ions were accelerated and detected by a 120 mm diameter multichannel plate (MCP) detector coupled to a fast phosphor screen. A charged-coupled device (CCD) camera captured the image, and a photomultiplier tube collected the total ion signal. The IMACQ/IMAN megapixel imaging software[41] acquired and analyzed the resulting data. We obtained the Cl/Cl* branching by scanning over both Cl transitions. For the 235 nm absorption, we used a single laser in this case, while for the 202nm transition, we used the TCRD approach with the 282 nm laser frequency fixed. We scanned these transitions multiple times to ensure consistent results and measured the power of the UV beams throughout the experiment to obtain constant signal levels. We adjusted our measured Cl/Cl* ratios using the REMPI sensitivity to the two spin-orbit states reported by Regan *et al.*[120] using the equation

$$\frac{I(Cl^*)}{I(Cl)} = \frac{N(Cl^*)}{S(Cl^*)} \div \frac{N(Cl)}{S(Cl)} = \frac{N(Cl^*)}{N(Cl)}, \tag{5.1}$$

where I(Cl*)/I(Cl) is the branching ratio to be determined, N(Cl*)/N(Cl) is the integrated experimental REMPI intensities, and the scaling factor, f = S(Cl)/S(Cl*). They employed high-n Rydberg H atom time-of-flight measurements to obtain the Cl (^2P_J) spin-orbit branching for HCl photodissociation, determining the scaling factor f for the REMPI sensitivity by comparing the raw REMPI intensities to the data obtained for the H atom product. The resonance enhanced multiphoton ionization (REMPI) probabilities obtained were through the 4p $^2D_{3/2} \leftarrow^2 P_{3/2}$ and 4p $^2S_{1/2} \leftarrow 3p^2P_{1/2}$ Cl-atom transitions (although we note the latter transition was mislabeled as 4p $^2P_{1/2}$.) Comparing the results from both H and Cl probe, they derived the Cl:Cl* scaling factor f =1.06 ± 0.17. In our TCRD probe, we are not assured of having the same scaling factor if, for example, one of the photon energies falls near an embedded resonance. This is not the case here, as the similarity in the

branching at both wavelengths given below would seem to confirm.

5.3 Results

Figure 5.2 shows the DC sliced images of ground state (Cl) and spin orbit excited (Cl*) chlorine atoms collected by photolysis of TCE at 235 nm with an acquisition of 100,000 shots for each image. The right side of Figure 5.3 shows the corresponding translational energy distributions extracted from the images. The image of ground state Cl has a clearly seen sharp edge at high translational energy. The translational energy distribution for Cl peaks around 1 eV and shows a sharp drop immediately after the peak, very near the indicated limit of available energy. The Cl* shows a broad distribution with the peak around 0.75 eV.

Figure 5.3 shows the images recorded for Cl and Cl* at 202 nm, and the corresponding translational energy distributions. In contrast to the image obtained at 235 nm, the ground state image at 202 nm shows a dominant slow component (low E_T). Furthermore, the intensity at higher translational energies is significantly lower compared to the images collected at 235 nm.

The branching of Cl*/Cl products at 235 nm and 202 nm wavelengths are shown in Table 5.1. The relative contributions for Cl and Cl* were obtained by integrating the REMPI Doppler profile for each wavelength, corrected by the scaling factor, f = 1.06 $\pm$0.17 as described above.[120] The results show a consistent branching of Cl:Cl* of 70:30 despite the difference in the excitation energies. The average translational energies for Cl and Cl* products, and the fraction of the available energy in translation, f_T, are also shown. At both excitations energies, the average translational energy release is similar for Cl and Cl*, while the fraction of the available energy in translation is significantly larger at 235 nm than 202 nm.

Figure 5.4 shows plots for the Cl* branching versus the total translational energy for the two dissociation energies. These were obtained by weighting the integrated translational energy plots (P(E)s) for Cl and Cl* by the overall product ratio, then by taking the ratio of

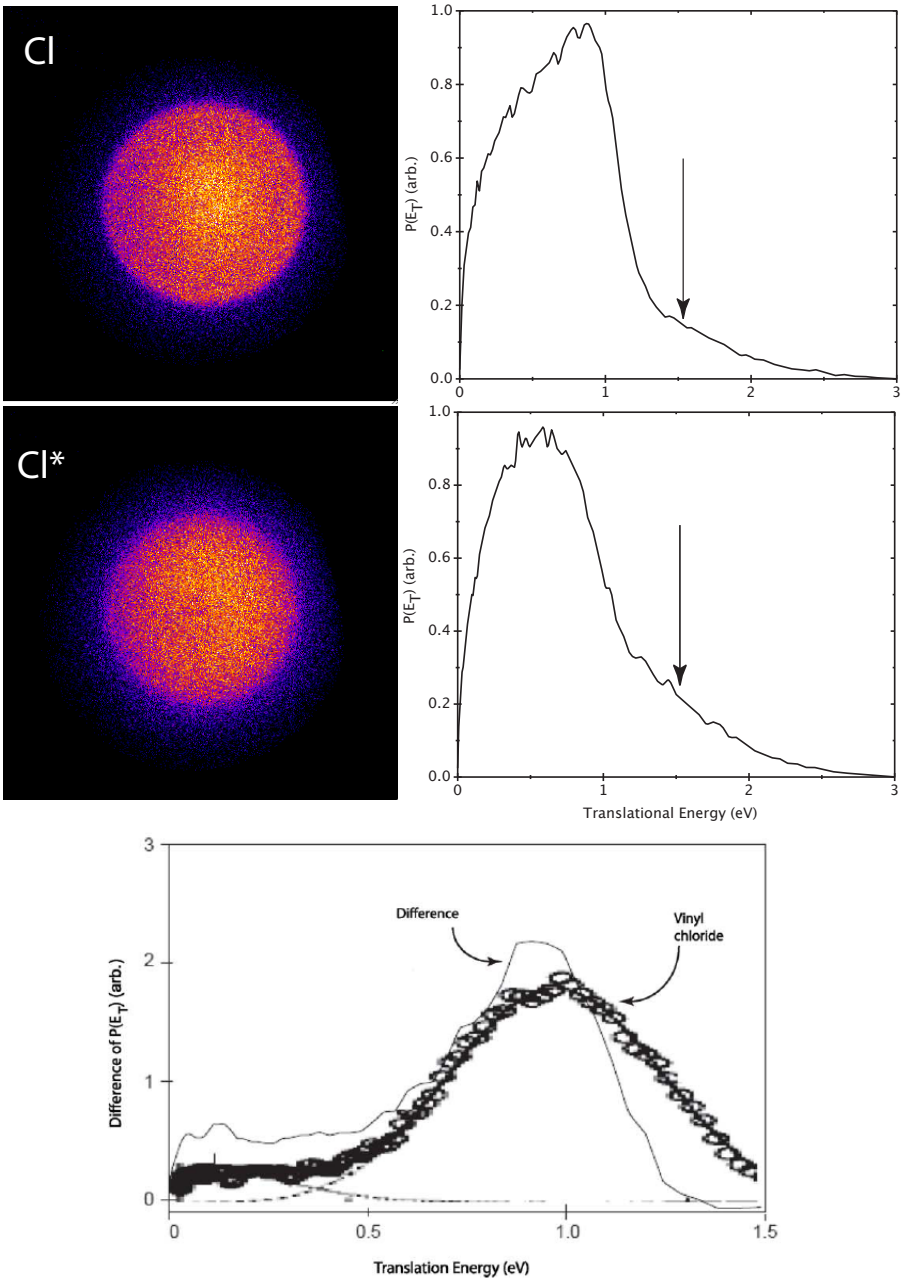

Figure 5.2: DC slice images and total translational energy distributions of C_2Cl_4 dissociation at 235.326 and 235.195 nm probed via Cl ($^2P_{3/2}$), 4p $^2D_{3/2} \leftarrow ^2 P_{3/2}$ transition and Cl* ($^2P_{1/2}$), 4p $^2S_{1/2} \leftarrow 3p^2P_{1/2}$ transitions, respectively. The arrows denote maximum product translational energy assuming one photon excitation. The third plot is the difference of normalized Cl and Cl* distributions. The latter is overlaid with Cl data from photodissociation of vinyl chloride ; adapted from K. Tonokura, L. B. Daniels, T. Suzuki, and K. Yamashita, J. Phys. Chem. A 101(42), 7754 (1997).© 1997 ACS

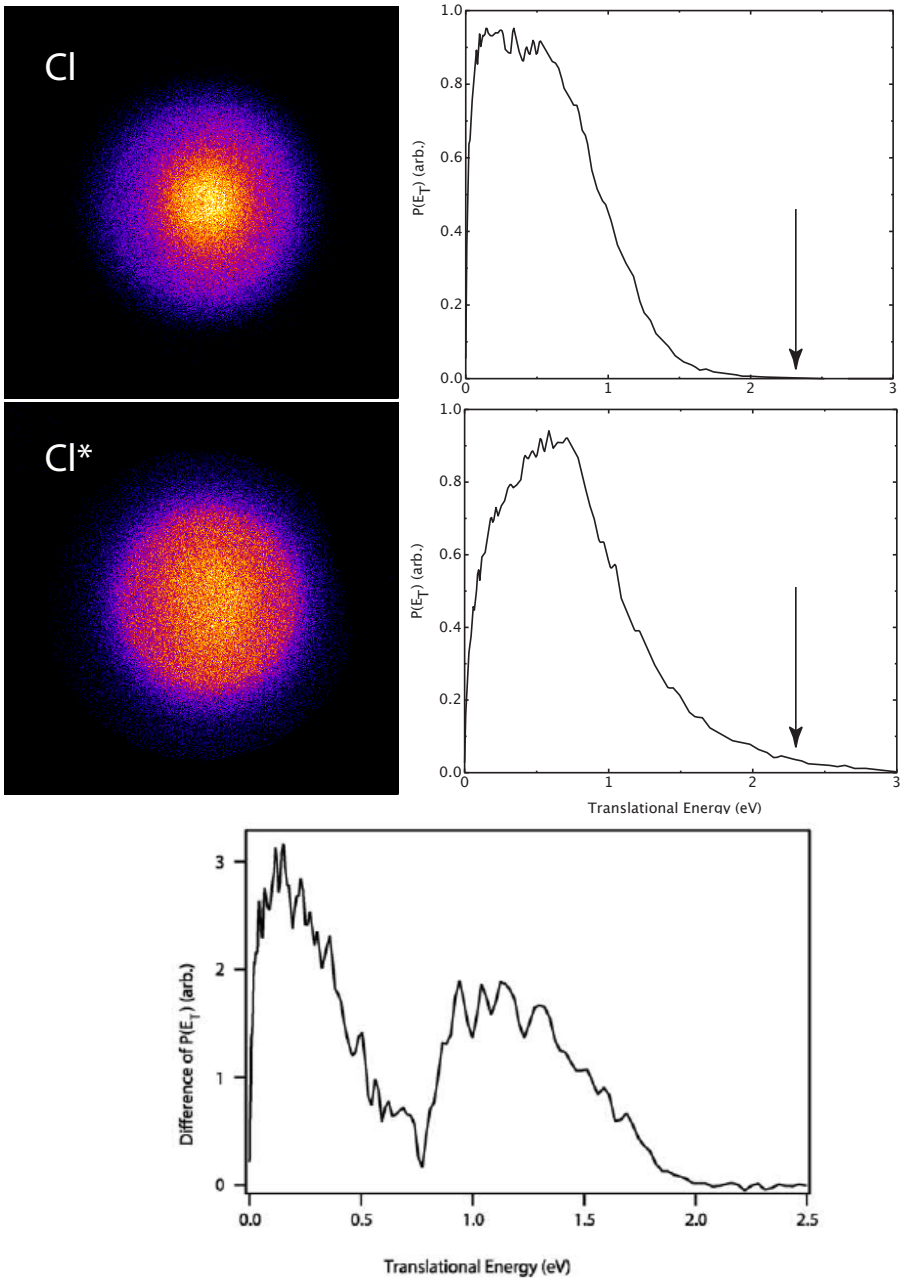

Figure 5.3: DC slice images and total translational energy distributions of C_2Cl_4 dissociation at 202.0 and 201.808 nm probed via Cl ($^2P_{3/2}$), 4p $^2D_{3/2} \leftarrow^2 P_{3/2}$ transition and Cl* ($^2P_{1/2}$), 4p $^2S_{1/2} \leftarrow 3p^2P_{1/2}$ transitions, respectively. The arrows denote maximum product translational energy assuming one photon excitation. The third plot is the difference of the normalized Cl and Cl* translational energy distributions.

Table 5.1: The Cl and Cl* product percentage yield, average translational energy (eV), and fraction of available energy in translation, f_T, at 235 and 202 nmUncertainty for the branching is 2σ for four independent measurements

	Branching ratio		Average Translational Energy (eV)		f_T	
Wavelength (nm)	Cl	Cl*	Cl	Cl*	Cl	Cl*
235	71.8(44)	28.2(44)	0.61	0.60	0.41	0.40
202	70.8(8)	29.2(8)	0.63	0.68	0.27	0.30

the Cl* P(E) to the weighted sum of the two P(E)s at each wavelength. At 235 nm, the plot shows a sharp decline around 1 eV. On the other hand, at 202 nm, the ratio of the excited molecules shows a similar albeit smoother drop around 1.5 eV. Both excitation energies show a relatively constant percentage of excited state Cl* of about 30%, the same as the total percentage.

The anisotropy parameters were obtained by fitting the angular distributions, integrated over recoil velocity, to the well-known expression[28] :

$$I_s \propto 1 + \beta P_2(\cos\theta), \tag{5.2}$$

where θ is the angle between the photolysis laser and the direction of the fragment recoil velocity, $P_2(x)$ is the second Legendre polynomial, and β ranges between 2 and -1. The obtained anisotropy parameters (β) of Cl and Cl* are ~ 0.05 at both excitation energies, essentially isotropic.Anisotropy parameters, particularly near the higher velocity feature, showed little difference and ranged from 0.01 to 0.08.

5.4 Discussion

We will begin our discussion with the DC sliced images and the translational energy distributions obtained at 235 nm as shown in Figure 5.2. Using gas phase enthalpy of formation values from Bylaska *et al.*[113], we can calculate the maximum energy release available for each wavelength. At 235.35 nm, the available energy is 1.5 eV, which is shown by the arrows

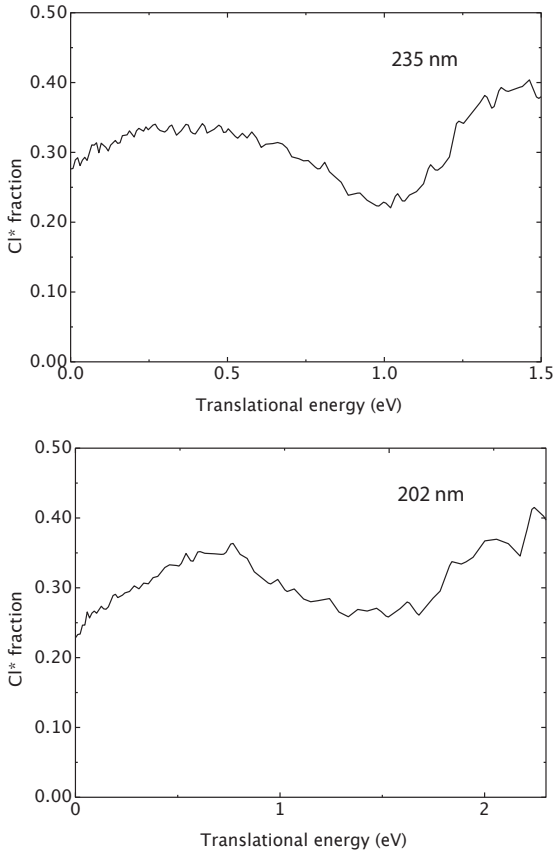

Figure 5.4: Translational energy distributions of the fraction excited state Cl($^2P_{1/2}$) for both excitation energies at 235 nm and 202 nm. These two plots are obtained from the distributions in Figure 5.2 and Figure 5.3, respectively.

on the translational energy distributions in Figure 5.2. The signal observed beyond the cut-off point is likely due to the multiphoton dissociation of C_2Cl_4 or photodissociation of the C_2Cl_3 radical product. We tried to minimize the multiphoton dissociation by reducing the power of both UV pulses, but the translational energy distributions showed little difference as laser power was reduced four-fold. The other distinct feature of the Cl distribution is the sharp peak seen in translational energy curve just after the 1 eV, which is close to the limit of the available energy for the Cl product. We conducted our experiment at 5.3 eV; the same energy range assigned by Eden *et al.*[115] to the $\pi\sigma^*$ electronic transition. In this transition, the electron is directly excited into the C-Cl antibonding orbital, rupturing the C-Cl bond

and resulting in fast Cl atoms with little internal excitation of the C_2Cl_3 radical co-product. This direct dissociation process creates the sharp peak in the translational energy distribution. The remaining lower energy component is either due to photo absorption into the tail of the $\pi\pi^*$ absorption underlying the $\pi\sigma^*$ feature, followed by internal conversion (IC) and dissociation of a longer-lived intermediate, or to ultrafast IC directly competing with dissociation from the repulsive $\pi\sigma^*$ultimately leading to a state that dissociates more or less statistically.

Next we will move on to the DC slice images and the translational energy distributions obtained at 202 nm. The calculated available energy at 202 nm is 2.3 eV, which is indicated by the arrows on the energy distributions in Figure 5.3. At 202 nm, the signal observed due to the multiphoton ionization is lower than in the case of 235 nm consistent with the six-fold stronger parent absorption at this wavelength.

The ground state Cl atom translational energy distribution can be explained by the bound $\pi\pi^*$ state, and its subsequent transitions to lower-lying states. Ashfold *et al.*[121] recently presented a comprehensive review of photochemistry of $\pi\sigma^*$ states that are often accessed following excitation of $\pi\pi^*$ states through nonadibatic coupling or conical intersections. Similar to what we have seen with at 235-nm excitation, these $\pi\sigma^*$ states are dissociative. However, the $\pi\pi^*$ state is bound, so dissociation will either be by IC to a lower-lying state or to a repulsive excited state. As we see a similar change in the Cl*/Cl ratio from excitation at 202 nm, we conclude that this is due to either remaining excitation of the $\pi\sigma^*$ state or fast, nonadibatic transition from the $\pi\pi^*$ state to a repulsive state. However, the low intensity at high translational energies in the both the Cl and Cl* energy distributions suggest little or no coupling to the $\pi\sigma^*$ surface in this case, with dissociation taking place via lower-lying triplet states or the ground state instead.

Vinyl chloride (VC) is likely to have similar dissociation dynamics as C_2Cl_4 and is a useful subject for comparison. Tonokura *et al.*[118] obtained images and Blank *et al.*[122] time-of-flight spectra from the photodissociation of VC at 193 nm, and determined that the

excitation was to a $\pi\pi^*$ state. A bimodal distribution was observed with fast fragments strongly dominating, and in this case, an anisotropic angular distribution. The $\pi\pi^*$ state is bound, so dissociation requires IC to either another excited state or the ground state. It was generally thought the $\pi\sigma^*$ repulsive state was responsible for high translation energy fragments; however, Arulmozhiraja *et al.*[119] calculations suggest instead it is the nσ^* state. While this nσ^* is higher in energy than the $\pi\pi^*$ state, as the Cl bond breaks, the nσ^* state crosses and couples with the $\pi\pi^*$ state forming an avoided crossing and leading to fast dissociation. The $\pi\sigma^*$ state couples to the $\pi\pi^*$ state as well, but this requires C=C out-of-plane twisting motion. They concluded that this would lead to slower Cl products. The Cl products of the VC photodissociation show mainly a strong, highly anisotropic peak around 1 eV translational energy, superimposed on a much smaller component peaking near zero translational energy. The fast component strongly resembles the fast component in the ground state Cl from TCE at 235 nm. The slow component in vinyl chloride was ascribed to IC to the ground state. In the VC absorption spectrum, there is no evidence of the $\pi\sigma^*$ shoulder as seen in TCE, so the excitation at 193 nm is believed to be dominated by the $\pi\pi^*$ state. Still, the results from both dissociation energies suggest some interesting distinctions between TCE and VC. For the $\pi\pi^*$ excitation in TCE, we see little evidence of IC to repulsive surfaces, and in fact the only evidence of these is in the ground state Cl at 235nm, which is likely from direct excitation to the $\pi\sigma^*$ surface. Instead, TCE dissociation is dominated by what appears to be statistical dissociation on lower-lying states. This difference is likely due to the change in the relative energy of the excited states in these two molecules. In going to from VC TCE, addition of halogens stabilize the $\pi\pi^*$ state due to electronegative inductive effects, while destabilizing the π state due to interaction of nonbonding Cl orbitals with the vinyl group; thus, the $\pi\pi^*$ state is lower in energy by over 0.5 eV in TCE compared to VC; However, the nσ^* state is nearly the same energy.[119] Potential energy surface calculations of Cl bond stretching are not available for TCE, but it is likely that the coupling between these two states could leave a barrier that is too large for TCE to dissociate via the nσ^*

surface. The $\pi\sigma^*$ state could be involved, but that would require energy to be left in C=C twisting motion leading to less remaining energy available for translational energy. Perhaps more important, for TCE the $\pi\sigma^*$ states are lower in energy than the $\pi\pi^*$ state,[114] meaning that there are no direct crossings and IC is required for an transfer between the two surfaces. Indeed, at 202 nm, as discussed below, we see no evidence of the fast Cl indicating a fast, repulsive pathway; whereas, the image obtained using 235-nm excitation shows a sharp peak and at the same time a drop in Cl*/Cl ratio. We conclude this is the signature of dissociation of the $\pi\sigma^*$ state.

The branching ratio for Cl and Cl* at 235 nm and 202 nm are quite similar. The ratio we observe is near the statistical 2:1 ratio of the degeneracy of the two states, albeit with a slight, energy-dependent deviation from this. We observe the greatest deviation from the average for the ground state Cl product precisely at the energy where we expect to see the greatest contribution for the $\pi\sigma^*$ dissociation. The energy distributions of Cl* fragments themselves contain no analogous sharp feature, suggesting that Cl* is a much smaller fraction of the product via the $\pi\sigma^*$ excitation. In the case of 202 nm photodissociation, the Cl* fragments peak at slightly higher energies than the Cl fragments. For a statistical dissociation from the ground state, there would be little difference. The Cl* translational energy distribution in particular appears to have a feature that abruptly ends just before 1 eV. The ground state also contains this feature as a double peak or perhaps a plateau with the feature due to IC to the ground state. This change in the maximum of the Cl* image may be due to some remaining underlying dynamics. For example, there are lower lying triplet surfaces, particularly the triplet $\pi\sigma^*$ states, that could be accessed as the molecule dissociates, and coupling to the $\pi\sigma^*$ state itself is a possible candidate as the required C=C twisting motion could lead to slower fragments. Another possibility is secondary dissociation of another Cl atom. Heat of formation data suggest that another 1.2 eV of energy is required[113, 123]. This would be energetically possible at the 202 nm dissociation, but barriers along this channel could preclude it.

It may seem surprising that the anisotropy parameters for the images are near zero with a component clearly evident from fast dissociation at 235 nm. The UV photodissociation study of vinyl chloride by Tonokura *et al.*[118] determined the anisotropy parameters for Cl photofragments. They obtained β 1.0 consistent with fast dissociation. Furthermore, their *ab initio* calculations predicted β as 1.0 with the transition dipole moment lying 34° from to the C-Cl direction. In contrast, we have a fully chlorinated system. Here, the transition dipole moment should be lying along the molecular axis of the C=C bond. We carried out time-dependent density functional theory calculations at the B3LYP/6-311 + d level using the Gaussian 09 package[100]. We found several excited states with significant oscillator strengths near the energy range considered, consistent with previous work. We found the angle between the C-Cl and the dipole moment direction was 54.6° for these states, implying a theoretical β value for axial recoil of 0.02, which is near isotropic and consistent with our experimental results. This angle between the transition dipole moment and the C-Cl bond will not result in any observed anisotropy regardless whether the dissociation is fast or slow. We can thus conclude that the sharp cutoff that is most apparent in the Cl image at 235 nm occurs as a result of direct dissociation on a repulsive surface, with the absence of anisotropy due to the geometry of TCE. For the Cl* product, and the Cl product at 202 nm, we might not expect any anisotropy, as the dissociation may not be rapid; in any case, we do not expect to observe any anisotropy given the geometry of the parent molecule.

5.5 Conclusions

We have studied the UV photodissociation of C_2Cl_4 near 235 nm and 202 nm using a two-color reduced-Doppler dissociation/probe strategy with DC slice imaging. We reported the translational energy distributions and the recoil-energy dependent branching ratios of Cl fragments in the ground state Cl($^2P_{3/2}$) and the excited state Cl*($^2P_{1/2}$). At 235 nm, the dissociation occurs in part via a $\pi\sigma^*$ excitation yielding more Cl product, whereas at 202 nm, excitation is exclusively to the $\pi\pi^*$ state with IC to other states preceding dissociation. The near-statistical branching ratio and broad translational energy distributions peaking at lower energy at both wavelengths is due to a large contribution from IC and dissociation from the ground state or lower-lying states of C_2Cl_4. A fast component with diverging product yield tending towards Cl is due to direct dissociation on the $\pi\sigma^*$ that is accessed through direct excitation and not likely due to electronic transfer from the $\pi\pi^*$ state. All the images are nearly isotropic, with anisotropy parameters (β)$\sim$ 0.05.

Chapter 6

Slice Imaging Studies of Nitric acid Photodissociation: $O(^1D)$ + HONO channel

6.1 Introduction

This chapter presents the slice imaging studies of nitric acid photodissociation using the state-resolved imaging approach. The ultraviolet photodissociation of nitric acid is of considerable importance in Earth′s atmosphere[124], motivating many studies of its dissociation processes, branching ratios and quantum yields [125–136]. In recent years it has become clear that in the region of the intense deep UV absorption to the S_3 ($2\ ^1A'$) excited state at 190 nm, the products $O(^1D)$ + HONO dominate over the OH + NO_2 ($1\ ^2B_2$) channel despite being energetically disfavored by 2 eV [136]. There is some disagreement over the angular distributions, and the dynamical studies in this region have exclusively used photofragment translational spectroscopy (PTS), first by Huber and coworkers[127], and later by the Butler group.[132] This system is thus a promising one for application of the high-resolution DC slice imaging approach, as state-correlated product distributions may be used to gain deeper insight into the dissociation mechanisms and resolve some of these open questions.

The ground state of HNO_3 is planar, of $^1A'$ symmetry, and there is a weak transition at 260 nm accessing the S_1 ($^1A''$) state[137]. This state exclusively dissociates to OH + NO_2, and it has been the subject of numerous studies [126, 130, 132]. There is another $^1A''$

state at 337 nm with little oscillator strength, and the broad S_3 absorption mentioned above peaking at 190 nm[137]. This transition is described by Bai and Segal as a mixture of $n\pi^*$ and $\pi\pi^*$ transitions. Although the ground state is planar, all of these excited singlet states possess similar pyramidal equilibrium geometries.[137] Product branching at 193 nm was reported by Butler and coworkers[132] based on analysis of the PTS results: they concluded total branching to O atom formation of 67%, with 54% to $O(^1D)$ and the remainder to ground state $O(^3P)$. Formation of OH + NO_2 accounted for the remaining 33%, including both ground state and electronically excited NO_2. There is rough agreement between these determinations and results from Ravishankara and coworkers[126] who reported quantum yields for $O(^1D)$ at 193 and 222 nm of 33% and 7%, respectively.

In this study, $O(^1D)$ is sensitively probed *via* 2+1 resonant ionization at 205 nm ($^1P_1 \leftarrow\leftarrow {}^1D_1$) and 203 nm ($^1F_3 \leftarrow\leftarrow {}^1D_1$), allowing us to perform convenient "1-laser" (both dissociation and probe) imaging studies following excitation to the S_3 state.

6.2 Experimental section

The detailed description of the experimental setup employing the DC slice imaging approach has been described previously[37–39] and only a brief outline is given here. Fuming HNO_3 acid (99.5%, Sigma Aldrich) was bubbled with Ar to remove traces of NO_2. $O(^1D)$ images from NO_2 were also recorded and compared to ensure that there was no residual contamination of the HNO_3 signal. Argon was then also used as a carrier gas to deliver 5% HNO_3 at a backing pressure of 2 bar into the source chamber operated at 10^{-5} Torr. A supersonic molecular beam of the resulting gas mixuture was generated by expansion through a solenoid valve. This molecular beam entered the main chamber, held at 10^{-7} Torr, through a 1 mm skimmer. A linearly polarized laser intersects the molecular beam perpendicular to the propagation axis. The tunable UV laser beam was produced by the frequency doubling of the fundamental output of a dye laser (Spectra-Physics Sirah) pumped by the second harmonic of a Nd:YAG laser (Spectra-Physics Quanta-Ray PRO-250) in KDP, then mixing

the fundamental and doubled light in a BBO crystal after matching the polarization using a waveplate. Dissociation of the HNO_3 and probing of the O(^{1}D) product was accomplished by a single laser beam, linearly polarized parallel to the detector face. The O (^{1}D) was probed by 2+1 REMPI through the $^1P_1 \leftarrow\leftarrow {}^1D_2$ (205.4 nm) and $^1F_3 \leftarrow\leftarrow {}^1D_2$ (203.8 nm) transitions. The output power of the laser was ∼1.4 mJ . The laser frequency was continuously scanned across the Doppler profile during image acquisition. The resulting O^+ ions were detected by a 120 mm microchannel detector (MCP) coupled to a fast phosphor screen where the gate of the time of flight was set to detect the mass of the O atom. For the DC slice imaging approach a ca. 60 ns gate was applied on to the MCP in order to select the center of the ion cloud. The phosphor screen was monitored by a CCD camera and a photomultiplier tube. Ion impact spots were centroided prior to integration. The imaging acquisition and analysis were done by our IMACQ Megapixel imaging software as reported previously.[41] DC sliced velocity images were calibrated by the detection of N_2 from the photodissocaiton of N_2O at 203.6 nm.[138]

6.3 Results

DC slice images of photodissociaton of HNO_3 obtained at 205.4 nm and 203.8 nm are shown in Fig. 6.1. Each image was acquired by averaging 100,000 shots. Images $^1P_1$ and $^1F_3$ were obtained by probing the O(^{1}D) atom *via* the$^1P_1 \leftarrow\leftarrow {}^1D_2(2 \times 48668.3\ cm^{-1})$ and $^1F_3 \leftarrow\leftarrow {}^1D_2(2 \times 49064.2\ cm^{-1})$ transitions, respectively. Both images consist of 4 rings showing a parallel transition. Figure 6.1 shows the corresponding translational energy distributions obtained from the images. As mentioned in the experimental section, the calibration was performed using the image on a single N_2 rotational level from N_2O photodissociation. The translational energy plots show 4 peaks which correspond to each ring in the DC slice images. For $^1P_1$ and $^1F_3$ images, the position of each peak is roughly the same (there is only 500 cm^{-1} difference in available energy) but the intensities of each ring vary. In particular, the intensity of the sharp peak at low translational energy is significantly larger for HNO_3

dissociation at 203 nm ($^1F_3$ probe) than for dissociation at 205 nm ($^1P_1$ probe).

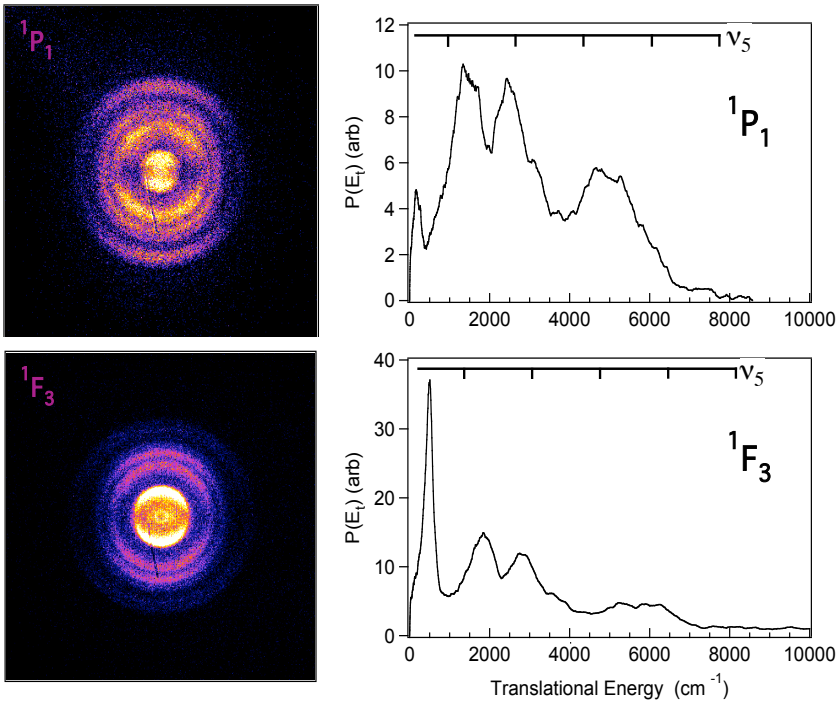

Figure 6.1: DC slice images and translational energy distributions of HNO_3 dissociation at 205.1 nm and 203.8 nm probed via the indirect transition of $O(^1P_1 \leftarrow\leftarrow ^1D_2)$ and $O(^1F_3 \leftarrow\leftarrow ^1D_2)$

The images show additional structure beyond that expected for the scattering distribution following one-photon dissociation. This is clearly a manifestation of polarization of the $O(^1D)$ orbital which modulates the detection efficiency, a **v-J** vector correlation. It is most apparent on the second ring of the $^1P_1$ probe transition. The angular momentum polarization of atomic products in photolysis of important atmospheric polyatomic molecules has been the subject of many recent publications. [29–34] It is most apparent on the second ring of the $^1P_1$ probe transition.

Figure 6.2 shows the angular distributions obtained for each ring of the images. To understand the structure in these images, we consider the angular momentum distribution of $O(^1D)$ from the photodissociation of HNO_3 molecules and its manifestation in these "1-laser" experiments.

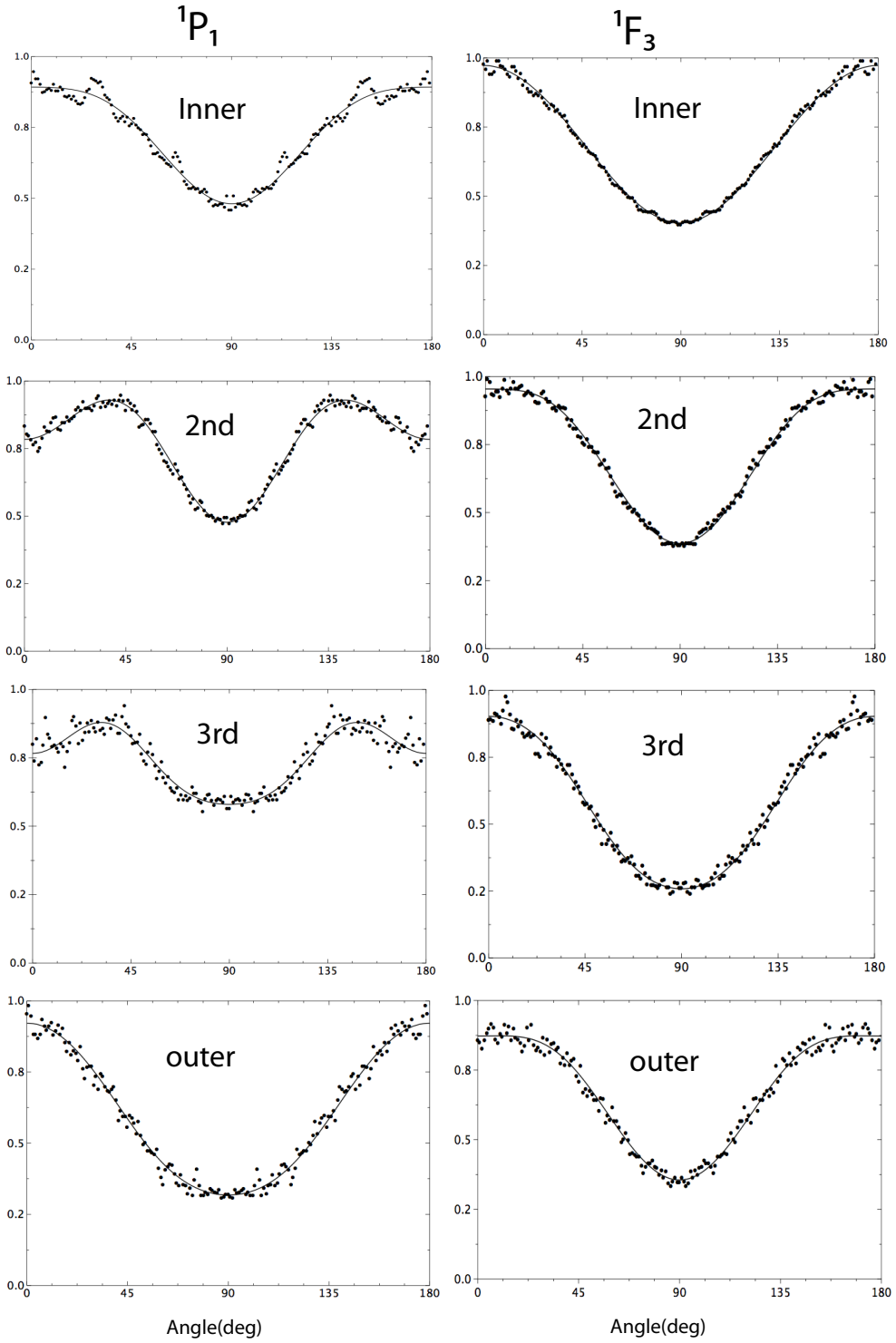

Figure 6.2: Angular distributions of the O(^{1}D) recoil velocity from the $\sim$ 204 nm photodissociation of HNO_3 for each of the four primary HONO co-product vibrational states as measured via the $^1F_3 \leftarrow\leftarrow {}^1D_2$ and $^1P_1 \leftarrow\leftarrow {}^1D_2$ oxygen transitions. The smooth curves denote the fit of Eq. 6.6 to experimental data.

Table 6.1: Fitted β parameters, shown in Fig. 6.2

	$^1P_1$			$^1F_1$		
	β_2	β_4	β_6	β_2	β_4	β_6
Inner	0.46	-0.12	-0.001	0.64	-0.03	0.002
2nd	0.42	-0.35	0.008	0.68	-0.16	-0.02
3rd	0.33	-0.15	-0.09	0.94	0.005	-0.04
Outer	0.79	0.07	-0.02	0.68	-0.18	-0.02

The theoretical calculations were done by the assistance of our collaborator Prof. Oleg S. Vasyuntinskii. Given the laser light source is linearly polarized parallel to the laboratory Z-axis, the expression for the experimental signal is:[35]

$$I_s = C\left[\rho_{00} + \frac{P_2}{P_0}\rho_{20} + \frac{P_4}{P_0}\rho_{40}\right], \tag{6.1}$$

where ρ_{K0}, $K = 0, 2, 4$ is the photofragment state multipole[139] and P_K is the two-photon line strength factor.[140] As shown earlier by Mo and Suzuki [141], absolute linestrength factors are difficult to obtain, but the relative values may be easily calculated for these transitions. For the transition $^1F_3 \leftarrow\leftarrow^1 D_2$ the ratios of the linestrength factors are $P_2/P_0 = 0.68$, $P_4/P_0 = -0.11$; for the $^1P_1 \leftarrow\leftarrow^1 D_2$ transition, they are -0.60 and -1.1, respectively.[140, 141]

The expressions for the fragment state multipoles in Eq. 6.1 can be presented in the form: [142]

$$\rho_{00}(\theta,\phi) = \frac{1}{4\pi\sqrt{2j_A+1}}[1+\beta P_2(\cos\theta)], \tag{6.2}$$

$$\rho_{K0}(\theta,\phi) = \frac{\sqrt{2K+1}\,V_K(j_A)}{4\pi\sqrt{2j_A+1}}\left\{d^K_{00}(\theta)\Big(s_K - 2\alpha_K P_2(\cos\theta)\Big) - \sqrt{6}\,\gamma_K d^K_{01}(\theta)\sin\theta\cos\theta - \frac{\sqrt{6}}{2}\,\eta_K d^K_{02}(\theta)\sin^2\theta\right\}, \tag{6.3}$$

where $P_2(\cos\theta)$ is the second order Legendre polynomial, $d^K_{QQ'}(\theta)$ are Wigner d-functions, and the rank K can take the values $K = 2$ and $K = 4$. Note that these Legendre polynomials, with $\cos\theta$ arguments, are distinct from the linestrength factors above.

The anisotropy parameters α_K, s_K, γ_K and η_K in Eq. 6.2, embody the full description of the orbital alignment that can be probed via a two-photon transition. In the case of photodissociation of a linear molecule in the absence of Coriolis interactions, the parameters α_K and s_K represent contribution to the photofragment alignment from incoherent excitation via perpendicular and parallel transitions, while the parameters γ_K and η_K represent contribution from coherent excitation[140].

In the more general case of photolysis of an arbitrary polyatomic molecule, the interpretation given above may not be strictly valid, because each of the parameters can contain contributions from incoherent parallel and perpendicular excitations as well as contributions from coherent excitations.[143, 144] However, as recently shown by Shternin and Vasyutinskii,[143] the angular distributions in Eqs. 6.2 and 6.3 remain valid for any photolysis reaction. Each anisotropy parameter in Eq. 6.3 is proportional to a certain universal anisotropy transforming coefficient c^K_{kdq} , where K is the photofragment rank, k_d = 0, 1, 2 is the rank of the photolysis light polarization matrix, and q is the projection of each of the ranks K and k_d onto the recoil axis. The projection q = Ω-Ω' the coherence between the helicity states and Ω and Ω' of the product angular momentum onto the recoil axis. In perticular, C^2_{20} = -$\sqrt{30}V_2(j_A)\alpha_2$, C^2_{00} = -$\sqrt{15}V_2(j_A)s_2$, C^2_{21} = -$\sqrt{15/2}V_2(j_A)\gamma_2$ and C^2_{22} = -$\sqrt{15/2}V_2(j_A)\eta_2$ Moreover, Shternin and Vasyutinskii have proved[143] that the coherent quantum number q = 0,$\pm$1,$\pm$2 is a constant of motion, which is preserved in the photolysis of any polyatomic molecule, irrespective of the reaction mechanism.Usually the anisotropy parameters are determined in imaging experiments by recording images in several experimental geometries to isolate particular contributions.[140] In these one-beam experiments, this is not possible, so we develop an approximate treatment to examine the dominant features. A more detailed study of the O(^{1}D) polarization will follow in a future publication.

Substituting Eqs. 6.2 and 6.3 into Eq. 6.1, the latter can be rewritten as:

$$I_s = C'\Bigg[1+\beta P_2(\cos\theta)+\frac{\sqrt{5}P_2}{P_0}V_2 j_A P_2(\cos\theta)\left[s_2-2\alpha_2 P_2(\cos\theta)+\frac{3P_4}{P_0}V_4 j_A P_4(\cos\theta)\right]$$
$$\times\,[s_4-2\alpha_4 P_2(\cos\theta))-\frac{3\sqrt{5}P_2}{P_0}V_4 j_A\gamma_2\sin^2\theta(\cos^2\theta)$$
$$-\frac{3\sqrt{5}P_2}{P_0}V_2 j_A\eta_2\sin^4\theta$$
$$+\frac{3\sqrt{30}P_4}{4P_0}V_4(j_A)\gamma_4(\sin^2\theta\cos^2\theta)(3-7\cos^2\theta)$$
$$+\frac{3\sqrt{15}P_4}{8P_0}V_4(j_A)\eta_4(\sin^4\theta)(1-7\cos^2\theta)\Bigg] \tag{6.4}$$

Expansion over the the Legendre polynomials gives:

$$I_s = C'\Bigg[1-\frac{2\sqrt{5}}{5}\frac{P_2}{P_0}V_2(\alpha_2+\gamma_2+\eta_2)+\left(\beta+\frac{2\sqrt{5}P_2}{7P_0}V_2(\frac{7}{2}s_2-2\alpha_2-\gamma_2+2\eta_2)\right)$$
$$-\frac{2P_2}{7P_0}V_4(6\alpha_4+\sqrt{30}\gamma_4+\sqrt{15}\eta_4)(P_2\cos\theta)$$
$$-(\frac{9\sqrt{5}P_2}{35P_0}V_2(4\alpha_2+\frac{8}{3}\gamma_2+\frac{2}{3}\eta_2)-\frac{3P_2}{4P_0}V_4(s_4-\frac{40}{77}\gamma_4+\frac{12\sqrt{15}}{77})P_4(\cos\theta)]$$
$$-\left(\frac{2P_2}{11P_0}V_4(15\alpha_4-2\sqrt{30}\gamma_4+\sqrt{15}\eta_4)P_6(\cos\theta)\right)] \tag{6.5}$$

Equation 6.5 shows that in general the experimental signal can be presented in the known form

$$I_s(\theta)\propto 1+\beta_2 P_2(\cos\theta)+\beta_4 P_4(\cos\theta)+\beta_6 P_6(\cos\theta), \tag{6.6}$$

A fit of Eq.6.6 to the angular distributions shown in fig. 6.2 furnishes optimized values for β_2, β_4, and β_6, shown in table 6.1. Note that the second term in the first line in the *rhs* in Eq. 6.5 is proportional to the total photofragment alignment averaged over all recoil angles, which is usually small in photolysis of polyatomic molecules.

Neglecting the second term in the the first line in the *rhs* in Eq.6.5 compared with the unity, the relationship between the β_2, β_4, and β_6 parameters in Eq. 6.6 and the anisotropy parameters $\beta, \alpha_2, \alpha_4$, s_2, and s_4 in Eqs. 6.6 can be presented as:

$$\beta_2 = \beta + \tfrac{2\sqrt{5}}{7}\tfrac{P_2}{P_0}V_2(\tfrac{7}{2}s_2 - 2\alpha_2 - \gamma_2 + 2\eta_2) - \tfrac{2P_4}{7P_0}V_4(6\alpha_4 + \sqrt{30}\gamma_4 + \sqrt{15}\eta_4) \quad (6.7)$$

$$\beta_4 = \tfrac{-9\sqrt{5}}{35}\tfrac{P_2}{P_0}V_2(4\alpha_2 - \tfrac{8}{3}\gamma_2 + \tfrac{2}{3}\eta_2) + \tfrac{3P_4}{P_0}V_4(s_4 - \tfrac{40}{77}\alpha_4 - \tfrac{2\sqrt{30}}{77}\gamma_4 + \tfrac{12\sqrt{15}}{77}\eta_4) \quad (6.8)$$

$$\beta_6 = \tfrac{-2P_4}{11P_0}V_4(15\alpha_4 - 2\sqrt{30}\gamma_4 + \sqrt{15}\gamma 4) \quad (6.9)$$

The resulting six equations arising from the $^1F_3 \leftarrow\leftarrow {}^1D_2$ and $^1P_1 \leftarrow\leftarrow {}^1D_2$ transitions contain nine unknown anisotropy parameters and therefore cannot be resolved in general within the condition of our one-laser experiment. However, an approximate treatment of the problem is possible and given in Sec. IV.

6.4 Discussion

We begin our discussion of these results with an examination of the translational energy distributions, after which we will turn to the angular distributions and orbital polarization. The structure observed in the total translational energy distributions, shown in Fig. 6.1, is due to the vibrational excitation of the HONO co-product; the lowest electronic excitation of HONO is inaccessible.[145] HONO exists in two isomeric forms, cis and trans, with the trans isomer 200 cm^{-1} lower in energy and a barrier of 3500 cm^{-1} separating them.[146] *Ab initio* calculations by Bai and Segal[137] reported the molecular geometry of the S_3 excited state of nitric acid as pyramidal, with NO bonds bent 30° below the N-OH bond, and the O-H bond rotated 90° above the molecular plane, as depicted in Fig.**??**. This suggests a HONO product that is predominantly trans, and therefore we will focus our attention on this isomer, although the vibrational frequencies are quite similar for both HONO species.

There are six vibrational modes in *trans*-HONO, and their frequencies and character are

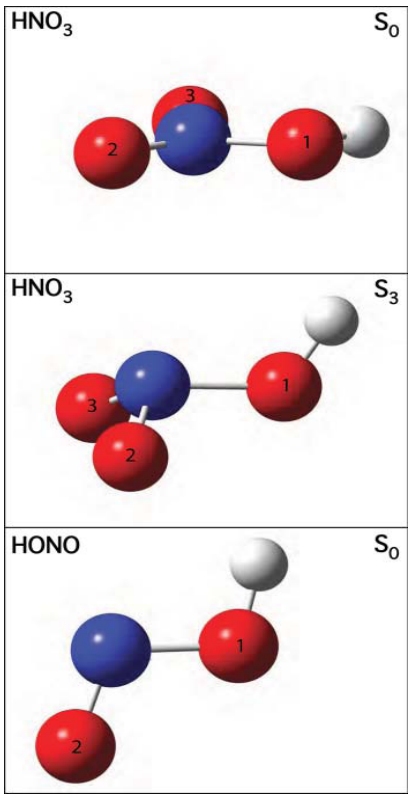

Figure 6.3: The geometries of HNO_3 ground state, excited state(S_3), and *trans*-HONO

presented in Table 6.3. It is clear that there are too many possible modes and combinations to make unique fits to the four broad peaks we observe. To understand the likely vibrational excitation in the HONO co-product, we thus consider the relations between the starting equilibrium geometry, the excited state geometry, and the HONO product, to look for large changes during the excitation and dissociation process. Table 6.2 shows the comparison of the molecular geometries of ground state HNO_3 ($1^1A'$), S_3 excited state HNO_3 ($2^1A'$), and *t*-HONO.[145, 147] Changes in N-O bond length and O-N-O bond angle are the major geometric adjustments to occur during the excitation from the ground state to the S_3 excited state and subsequent formation of *t*-HONO.

The N-O bond length increases during the excitation and then decreases to a shorter length than in the ground state. This suggests significant excitation in the N=O stretching

Table 6.2: The table of geometries of HNO_3 and trans HONOa) Ref. [137] b)Ref.[145]

State	Geometry					
	R_{OH}	R_{NO}	R_{NO_2}	O_1NO_2	O_2NO_3	HO_1N
HNO_3 $S_0(1^1A')$	0.95	1.39	1.22	115.0	130.0	102.[a]
HNO_3 $S_3(2\ ^1A')$	0.95	1.47	1.30	108.6	112.8	103.3[a]
t-HONO	0.96	1.43	1.17	110.7	- -	103.0[b]

mode. Change in the O-N-O bond angle from 115° to 108.6° during $S_3 \leftarrow S_0$ excitation, and then back to 110° in ground-state t-HONO likely induces excitation of the O-N-O bend. This, in conjunction with excitation to the pyramidal S_3 state in HNO_3 prior to dissociation, excites movement primarily in three main vibrational modes: the OH out of plane twist (ν_1) ,O-N-O bend (ν_2) and N=O stretching (ν_5). Therefore, neglecting possible exit channel dynamics, the translational energy distributions likely reflect excitation of these three dominant vibrational modes. According to the vibrational frequencies of t-HONO given in table 6.3, the difference between ν_1 and ν_2 is about 50 cm^{-1}. Thus the combination bands arising from vibrations of ν_1 and ν_2 cannot be distinguished separately. Furthermore $2\nu_1 + \nu_2$ is roughly equal to one quanta of ν_5. Therefore we are unable to make unambiguous assignment for each peak of the translational energy distribution. However, in figure 6.1 we overlay the ν_5 vibrational mode spacings, as we expect this to be the dominant high frequency excitation, with low frequency combinations superimposed on this.

We note that the vibrational energy in HONO corresponding to the sharp low energy peak $O(^1D)$ translational energy distribution is greater than four quanta of ν_5. This peak is particularly interesting in that it is so sharp, and it grows so quickly with the modest increase in excitation energy. Although our results provide no direct insight into the rotational excitation of HONO, it is likely to be significant, particularly for the faster HONO product, given the impulsive recoil, large bending excitation expected, and finite exit impact parameter. Future trajectory studies would be very useful to investigate this and to understand the detailed origin of this distinct vibrational structure we observe.

Table 6.3: Vibrational frequencies of HONO [145]

Vibrational frequency(cm^{-1})	Vibrational excitation	
544	ν_1	τ(O-H)
598	ν_2	δ(ONO)
793	ν_3	σ(O-H)
1263	ν_4	δ(NOH)
1698	ν_5	σ(N=O)
3590	ν_6	σ(O-H)

We now consider the β parameter values and the O(^{1}D) orbital polarization. The fits to the angular distributions in Table 6.1 show that the terms related with β_6 give only a minor contribution to the signals observed for both the $^1F_3 \leftarrow\leftarrow {}^1D_2$ and $^1P_1 \leftarrow\leftarrow {}^1D_2$ probe transitions. Moreover, the corresponding β_6 values are quite small. Therefore, we neglected all anisotropy parameters α_4, γ_4, and η_4 in Eqs. 6.7-6.9 the following analysis. The simplified Eqs. 6.7 and 6.8 were solved for the $^1F_3 \leftarrow\leftarrow {}^1D_2$ and $^1P_1 \leftarrow\leftarrow {}^1D_2$ transitions giving the parameters β, s_4 and the parameter combinations ($\frac{7}{2}s_2 - 2\alpha_2 - \gamma_2 + 2\eta_2$), ($4\alpha_2 - \frac{8}{3}\gamma_2 + \frac{2}{3}\eta_2$) shown in Table 6.4. The β values show a significant recoil velocity dependence and vary from 0.47 to 0.84, with the faster O(^{1}D) product having the larger β anisotropy parameter. These values are significantly lower than the 1.4 value measured by the Butler group;[132] although they compare favorably with $\beta = 0.6$ reported by Felder et al..[127] It seems that in the Butler study, they focused on the faster O atom product to avoid possible contamination from clusters, and this may have contributed to the greater anisotropy observed.

The β values show a significant recoil velocity dependence and vary from 0.53 to 0.74, with the faster O(^{1}D) product having the larger β anisotropy parameter. These values are significantly lower than the 1.4 value measured by the Butler group[132]; although they compared favorably with $\beta = 0.6$ reported by Huber and coworkers.[127] It seems that in the Butler study, they focused on the faster O atom product to avoid possible contamination

from clusters, and this may have contributed to the greater anisotropy observed.

In the axial recoil limit, a theoretical anisotropy parameter β can be calculated based on the angle φ between the transition dipole moment $\boldsymbol{\mu}$ and the recoil velocity $\mathbf{v}$: $\beta = 2P_2(\cos\varphi)$.[28] In the case of HNO_3, $\boldsymbol{\mu}$ lies in the molecular plane, parallel to the terminal oxygens.[132] Assuming prompt dissociation from the ground state and recoil along the bond axis, $\varphi = 25°$ determined from the geometry reported in Table 6.2 gives a theoretical $\beta = 1.47$, as reported by Butler's group.[132] For the pyramidal S_3 excited state equilibrium geometry, the analogous calculation gives a predicted β value of 0.98, still significantly more anisotropic than that we observe and reported by Huber. Back-calculation of the β's reported here correspond to O_2-N-O_3 bond angles of 91°-99°, in contrast to the 130° in the ground state and 112.8° in the S_3 excited state. It is postulated that the N=O bond cleavage occurs when the O-N-O bending excitation has overshot the S_3 equilibrium geometry, and the extent of bending excitation, reduced translational energy, and lowered anisotropy, are all correlated.

Table 6.4 reports the anisotropy parameters s_4 and the parameter combinations ($\frac{7}{2}s_2 - 2\alpha_2 - \gamma_2 + 2\eta_2$), ($4\alpha_2 - \frac{8}{3}\gamma_2 + \frac{2}{3}\eta_2$) as calculated using both the $^1F_3 \leftarrow\leftarrow {}^1D_2$ and $^1P_1 \leftarrow\leftarrow {}^1D_2$ transitions according to Eqs. 6.7 and 6.8 and the data in Table 6.1. The contribution from the s_4 alignment mechanism seems to be significant in our experiment, in particular for the second ring in the images. The obtained s_4-values can be compared with that obtained for N_2O photodissociation[142] [$s_4 = (9 \pm 2) \times 10^{-3}$] and with the possible physical range[35] (s_4 = -1/5. . .1/5). Direct determination of the parameters s_2, α_2, γ_2, and η_2 from the parameter combinations above is not possible for a one-laser experiment and needs further approximations. Here we assume that the contribution from the "coherent" parameters γ_2 and η_2 can be neglected as they do not appear to contribute significantly to the experimental images in Fig. 6.1. In that case, the parameters α_2 and s_2 can be easily obtained, and their values are also given in Table 6.4. It is clearly seen from Table 6.4 that the anisotropy parameter α_2 has its value close to zero, while the anisotropy parameters s_2 (and s_4) are

significant, although the uncertainty in the determined s_2 parameters is large. Note that both α_K and s_K anisotropy parameters refer to the contribution to the photofragment angular momentum alignment from incoherent (q = 0) mechanisms. The difference between these two sets of parameters is that α_K refers to the alignment which does not vanish after averaging over all recoil angles, while s_K refers to the alignment which exists only in the molecular frame and vanishes after averaging over all recoil angles[35, 140]. Moreover, $\alpha_K \propto c_{20}^K$ and $s_K \propto c_{00}^K$ [143] which means that α_K refers to the *alignment of the photolysis light polarization vector e, while s_K refers to the isotropic part of the photolysis light* and therefore reflect only the anisotropy of the intermolecular interactions during the photolysis. The dominant contribution from the s_K alignment mechanism seems to be usual in the photodissociation of polyatomic molecules, where the alignment usually exists in the molecular frame and vanishes after averaging over all recoil angles[35]. In addition, upon examining the s_K terms we see the alignment related to the higher order K = 4 term is important for certain rings in the images in Fig. 6.1, which is particularly apparent in the image obtained through the $^1P_1$ probe as a result of the larger P_4/P_0 line strength factor compared to the $^1F_3$ transition. We emphasize, however, that the conclusion about theminor role of the coherent photodissociationmechanism related to the parameters γ_K and η_K is tentative and should be proved in the future using a two-laser experimental scheme.

Much of the study of the photodissocation of HNO_3 has focused on the OH+NO_2 channel[130, 131, 148, 149]. The dominant channel for the photodissocation of HNO_3 at 193 nm, however, is O + HONO with quantum yields of 0.67[127, 132]. Recently Huber and co-workers[136] studied the wavepacket dynamics of HNO_3 in a two-dimenisional treatment fixed in the planar geometry. A key interest in the work was accounting for the remarkable preference for O(^{1}D) production despite the presence of a much lower energy, barrierless process forming OH+NO_2. They found that on the S_3 potential energy surface about 60% of the products form O(^{1}D) + HONO, and the reason is a much steeper slope of the potential along that dimension. It will be very interesting to see how these trends are manifested in

Table 6.4: Calculated anisotropy parameters for each of the four primary HONO vibrational states

	Inner	2nd	3rd	Outer
β	0.48(15)	0.47(9)	0.64(7)	0.84(12)
s_2	0.08(14)	0.24(5)	0.08(4)	0.04(14)
$(\ \frac{7}{2}s_2 - 2\alpha_2 - \gamma_2 + 2\eta_2)$	0.11(20)	0.08(14)	0.36(22)	-0.19(30)
$(4\alpha_2 - \frac{8}{3}\gamma_2 + \frac{2}{3}\eta_2)$	0.01(1)	-0.12(4)	-0.04(6)	-0.17(8)
α_2	0.002(8)	0.029(10)	-0.010(16)	-0.042(20)
s_2	0.40(90)	0.10(70)	1.2(12)	-1.0(16)

a full-dimensional treatment, which is clearly called for based on the angular distributions and vibrational excitation we observe.

6.5 Conclusions

Here we report the translational energy and angular momentum distributions of the $O(^1D)$ product from HNO_3 photodissociation near 204 nm. The vibrational energy distribution of the HONO coproduct, as seen through the $O(^1D)$ translational energy distribution, shows significant vibrational energy remaining in the molecule. Analysis of the angular distributions from both the $^1F_3 \leftarrow\leftarrow {}^1D_2$ and $^1P_1 \leftarrow\leftarrow {}^1D_2$ O probe transitions resulted in a $O(^1D)$ recoil velocity-dependent β of 0.5-0.7. Substantial alignment of the $O(^1\ D)$ orbital was observed and analyzed using an approximate treatment demonstrating that the polarization is dominated by incoherent, high order contributions. These results offer additional insight into the dynamics of the dissociation of nitric acid through the S_3 ($2\ ^1A'$) excited state, helping to resolve some outstanding questions and pointing the way to future studies.

Chapter 7

Conclusions and Prospectus

This dissertation presents the unimolecular photodissociation dynamics studies carried out using the state-resolved sliced ion imaging method. In the acetone photodissociation study, the CO fragments produced from photodissociation of acetone at 230 nm presents a bimodal distribution. This observation provides information regarding the photodissociation dynamics of acetone, suggesting it undergoes roaming dynamics analogous to the reported roaming dynamics in formaldehyde photodissociation and others. Furthermore, another type of roaming mechanism is introduced in the study of nitrobenzene photodissociation. This study, which is a combined theoretical and experimental approach, illustrates that the NO generated from nitrobenzene photodissociation undergoes isomerization prior to the C_6H_5O-NO simple bond rupture; this isomerization process is shown to proceed via a roaming mechanism, therefore it is referred to as "roaming mediated isomerization". Nitromethane is so far the only nitroalkane that has been studied to show roaming mediated isomerization. Nevertheless, our attempts to study higher nitroalkanes using a nanosecond pulsed laser was unsuccessful due to the fast photodissociation of excited state fragments. Nitroethane has following major dissociation pathways[150].

$$C_2H_5NO_2 \rightarrow C_2H_5 + NO_2 \tag{7.1}$$

$$C_2H_5NO_2 \rightarrow C_2H_5O + NO \tag{7.2}$$

$$C_2H_5NO_2 \rightarrow C_2H_4 + HONO \tag{7.3}$$

The calculated barrier height for isomerization, C_2H_5ONO is higher than the simple bond fission symptom of C_2H_5-NO_2 which is analogous to the nitromethane case. However, according to DFT and G3 calculations, one significant difference is that the HONO elimination channel is 11 kcal/mol lower than the simple bond fission of C_2H_5 + NO_2 [151]. Although this suggests that at lower energies, HONO is the major product, at higher energies roaming-mediated isomerization would likely dominate.

We investigated nitroethane, nitropropane and 2-nitropropane at 226 nm. Nitroalkanes were photodissociated and ionized using a single laser beam at 226 nm and the generated NO was probed at various rotational levels:(J= $Q_1(10.5)$, $Q_1(29.5)$, $Q_1(35.5)$, $P_1(50.5)$) via (1 + 1) REMPI through (ν=0) A$\leftarrow$ X transitions. Figure 7.1 presents the image obtained at $J = 50.5$ for nitroethane and the translational energy distribution extracted from this image. The nitropropane and 2-nitropropane images are similar thus they are not shown here.

Obviously, the image is highly anisotropic with the anisotropy parameter(β) ~ 0.5. This clearly illustrate that the excited state dynamics plays an important role in the dissociation process. Therefore, further studies for nitroethane and nitropropane should be carried out using a CO_2 laser. When the CO_2 laser is available, infrared multi-photon dissociation on nitroethane and nitropropane can be investigate and examine the NO yields, product state distributions and translational energy release a function of laser fluence to see if there is any evidence of roaming isomerization.

In the study of photodissociation dynamics of tertacholoethylene (TCE), the spin orbit branching ratio was calculated and found to be quite similar at two different wavelengths.

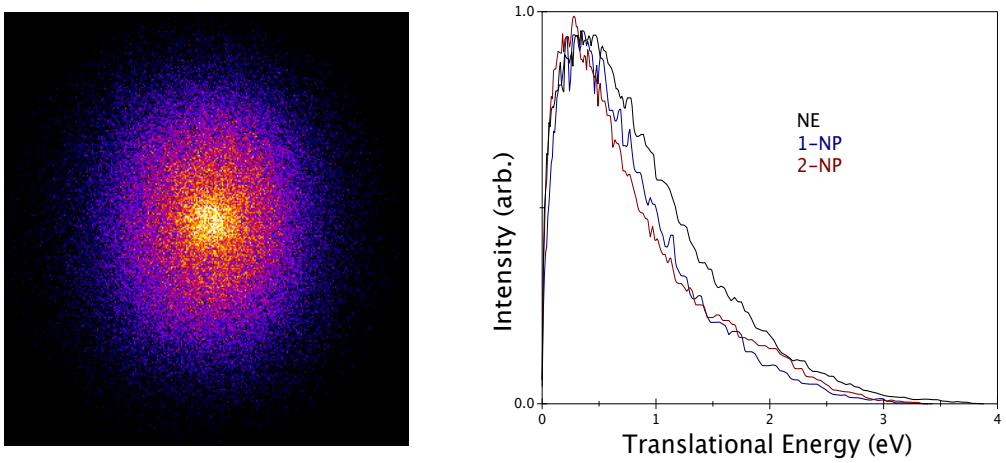

Figure 7.1: (Left) Direct current sliced images of NO from the photodissocation of nitroethane excitation at ∼226 nm. The NO fragment is probed via a 1+1 REMPI scheme through the NO $\nu = 0$, A $\leftarrow$ X band for the transitions: P_1 (50.5) (Right) The translational energy distribution extracted from the image. (Blue) The translational energy distributions obtained for 1-nitropropane, (red) The translational energy distributions obtained for 2-nitropropane

This observation was due to the fact that photodissociation takes place after internal conversion to the ground state or lower lying electronic excited states at both wavelengths.

In the study of nitric acid photodissociation at deep UV wavelengths, we found that the O(^{1}D) + HONO channel dominates despite the high bond dissociation energy, consistent with previous work. The HONO co-product is vibrationally excited and substantial alignment of the O(^{1}D) orbital was observed and analyzed using approximate treatments, demonstrating that the polarization is dominated by incoherent, high order contributions. There was inconsistency with the previously reported angular distributions and we believe that this might be due limitations in our experimental approach association with the use of a single laser for photolysis and probe. In this case, further experiments should be carried out to obtain more accurate values using two laser beams.

In this dissertation we focus on understanding unimolecular reaction dynamics using

the state-resolved slice imaging approach. This allowed us to identify new mechanisms and reaction channels created during the photodissociation events, to calculate the branching ratios and infer the complex reactive processes relevant in combustion, atmospheric and interstellar chemistry.

BIBLIOGRAPHY

[1] D. Townsend, S. A. Lahankar, S. K. Lee, S. D. Chambreau, A. G. Suits, X. Zhang, J. Rheinecker, L. B. Harding, and J. M. Bowman. The roaming atom: Straying from the reaction path in formaldehyde decomposition. *Sci.*, 306:1158, 2004.

[2] Arthur G. Suits. Roaming atoms and radicals: A new mechanism in molecular dissociation. *Acc. Chem. Res.*, 41(7):873–881, 2008. PMID: 18582091.

[3] Joel M Bowman and Xiubin Zhang. New insights on reaction dynamics from formaldehyde photodissociation. *Phys. Chem. Chem. Phys.*, 8:321–332, 2006.

[4] Joel M. Bowman and Benjamin C. Shepler. Roaming radicals. *Annu. Rev. Phys. Chem.*, 62:531, 2011.

[5] Fida Mohammad, Vernon R. Morris, William H. Fink, and William M. Jackson. On the mechanism and branching ratio of the cyanogen + oxygen .fwdarw. carbon monoxide + nitric oxide reaction channel using transient ir emission spectroscopy. *J Phys. Chem.*, 97(45):11590–11598, 1993.

[6] Timothy P. Marcy, Robert Richard Díaz, Dwayne Heard, Stephen R. Leone, Lawrence B. Harding, and Stephen J. Klippenstein. Theoretical and experimental investigation of the dynamics of the production of co from the ch3 + o and cd3 + o reactions. *J Phys. Chem. A*, 105(36):8361–8369, 2001.

[7] Vasiliy Goncharov, Sridhar A. Lahankar, John D. Farnum, Joel M. Bowman, and Arthur G. Suits. Roaming dynamics in formaldehyde-d2 dissociation. *J Phys. Chem. A*, 113(52):15315–15319, 2009. PMID: 19775138.

[8] Sridhar A. Lahankar, Steven D. Chambreau, Dave Townsend, Frank Suits, John Far-

num, Xiubin Zhang, Joel M. Bowman, and Arthur G. Suits. The roaming atom pathway in formaldehyde decomposition. *J Chem. Phys.*, 125(4):044303, 2006.

[9] S. A. Lahankar, S. D. Chambreau, X. B. Zhang, J. M. Bowman, and A. G. Suits. Energy dependence of the roaming atom pathway in formaldehyde decomposition. *J Chem. Phys.*, 126:044314, 2007.

[10] S. A. Lahankar, V. Goncharov, F. Suits, J. M. Farnum, J. D.and Bowman, and A. G. Suits. Further aspects of the roaming mechanism in formaldehyde dissociation. *Chem Phys*, 347:288, 2008.

[11] Xiubin Zhang, Shengli Zou, Lawrence B. Harding, and Joel M. Bowman. A global ab initio potential energy surface for formaldehyde. *J Phys. Chem. A*, 108(41):8980–8986, 2004.

[12] S. A. Lahankar, S. D. Chambreau, D. Townsend, F. Suits, J. Farnum, X. B. Zhang, J. M. Bowman, and A. G. Suits. The roaming atom pathway in formaldehyde decomposition. *J Chem. Phys.*, 125:044303, 2006.

[13] Kurt M. Christoffel and Joel M. Bowman. Three reaction pathways in the h + hco h2 + co reaction. *J Phys. Chem. A*, 113(16):4138–4144, 2009. PMID: 19235994.

[14] Lawrence B. Harding, Stephen J. Klippenstein, and Ahren W. Jasper. Ab initio methods for reactive potential surfaces. *Phys. Chem. Chem. Phys.*, 9:4055–4070, 2007.

[15] S. H. Houston, P.L. Kable. Dissociation of acetaldehyde at 308 nm : another example of the roaming mechanism. *PNAS*, 103:16079, 2006.

[16] Brianna R. Heazlewood, Meredith J. T. Jordan, Scott H. Kable, Talitha M. Selby, David L. Osborn, Benjamin C. Shepler, Bastiaan J. Braams, and Joel M. Bowman. Roaming is the dominant mechanism for molecular products in acetaldehyde photodissociation. *PNAS*, 105(35):12719–12724, 2008.

[17] B. C. Shepler, B. J. Braams, and J. M. Bowman. Quasiclassical trajectory calculations of acetaldehyde dissociation on a global potential energy surface indicate significant non-transition state dynamics. *J Phys. Chem. A*, 111(34):8282–8285, 2007.

[18] L. Rubio-Lago, G. A. Amaral, A. Arregui, J. G. Izquierdo, F. Wang, D. Zaouris, T. N. Kitsopoulos, and L. Banares. Slice imaging of the photodissociation of acetaldehyde at 248 nm. evidence of a roaming mechanism. *Phys. Chem. Chem. Phys.*, 9:6123–6127, 2007.

[19] L. B. Harding, S. J. Klippenstein, and A. W. Jasper. Ab initio methods for reactive potential surfaces. *Phys. Chem. Chem. Phys.*, 9:4055–4070, 2007.

[20] R. Sivaramakrishnan, J. V. Michael, and S. J. Klippenstein. Direct observation of roaming radicals in the thermal decomposition of acetaldehyde. *J Phys. Chem. A*, 114(2):755–764, 2010. PMID: 20017515.

[21] Lawrence B. Harding and Stephen J. Klippenstein. Roaming radical pathways for the decomposition of alkanes. *J Phys. Chem. Lett.*, 1(20):3016–3020, 2010.

[22] Chao Chen, Bastiaan Braams, David Y. Lee, Joel M. Bowman, Paul L. Houston, and Domenico Stranges. Evidence for vinylidene production in the photodissociation of the allyl radical. *J Phys. Chem. Lett.*, 1(12):1875–1880, 2010.

[23] Michael P. Grubb, Michelle L. Warter, Arthur G. Suits, and Simon W. North. Evidence of roaming dynamics and multiple channels for molecular elimination in no3 photolysis. *J Phys. Chem. Lett.*, 1(16):2455–2458, 2010.

[24] Harold S. Johnston, H. Floyd Davis, and Yuan T. Lee. No3 photolysis product channels: quantum yields from observed energy thresholds. *J Phys. Chem.*, 100(12):4713–4723, 1996.

[25] A. M. Wodtke, E. J. Hintsa, and Yuan T. Lee. Infrared multiphoton dissociation of three nitroalkanes. *J Phys. Chem.*, 90(16):3549–3558, 1986.

[26] M.C. Lin R.S. Zhu. Ch3no2 decomposition/isomerization mechanism and product branching ratios: An ab initio chemical kinetic study. *Chem. Phys. Lett.*, 478:11, 2009.

[27] Minh Tho Nguyen, Hung Thanh Le, Balázs Hajgató, Tamás Veszprémi, and M. C. Lin. Nitromethanemethyl nitrite rearrangement: a persistent discrepancy between theory and experiment. *J Phys. Chem. A*, 107(21):4286–4291, 2003.

[28] R.N. Zare. Molecular photochemistry. 4:1, 1972.

[29] Yuxiang Mo, Hideki Katayanagi, Michael C. Heaven, and Toshinori Suzuki. Simultaneous measurement of recoil velocity and alignment of $s(^1d_2)$ atoms in photodissociation of ocs. *Phys. Rev. Lett.*, 77:830–833, 1996.

[30] Zee Hwan Kim, Andrew J. Alexander, and Richard N. Zare. Speed-dependent photofragment orientation in the photodissociation of ocs at 223 nm. *J Phys. Chem. A*, 103(49):10144–10148, 1999.

[31] J.M. Teule, G.C. Groenenboom, D.W. Neyer, D.W. Chandler, and M.H.M. Janssen. State-to-state photodynamics of nitrous oxide and the effect of long-range interaction on the alignment of o(1d2. *Chem. Phys. Lett.*, 320:177 – 185, 2000.

[32] Suk Kyoung Lee, Dave Townsend, Oleg S. Vasyutinskii, and Arthur G. Suits. O(1d2) orbital orientation in the ultraviolet photodissociation of ozone. *Phys. Chem. Chem. Phys.*, 7:1650–1656, 2005.

[33] Alrik J. van den Brom, T. Peter Rakitzis, and Maurice H. M. Janssen. State-to-state photodissociation of carbonyl sulfide (nu[sub 2] = 0,1—j[script l]m). ii. the effect of initial bending on coherence of s([sup 1]d[sub 2]) polarization. *J Chem. Phys.*, 123(16):164313, 2005.

[34] M. Brouard, R. Cireasa, A. P. Clark, G. C. Groenenboom, G. Hancock, S. J. Horrocks, F. Quadrini, G. A. D. Ritchie, and C. Vallance. The photodissociation dynamics of ozone at 193 nm: An o([sup 1]d[sub 2]) angular momentum polarization study. *The Journal of Chemical Physics*, 125(13):133308, 2006.

[35] A. G. Suits and O. S. Vasyutinskii. Imaging atomic orbital polarization in photodissociation. *Chem. Rev.*, 108(9):3706–3746, 2008.

[36] M. N. R. Ashfold and J. D. Howe. Multiphoton spectroscopy of molecular species. *Ann. Rev. Phys. Chem.*, 45(1):57–82, 1994.

[37] Chandler D.W and P.L. Houston. Twodimensional imaging of stateselected photodissociation products detected by multiphoton ionization. *J. Chem. Phys.*, 87:1445–1447,

1987.

[38] A. T. J. B. Eppink and D. H. Parker. Velocity map imaging of ions and electrons using electrostatic lenses: Application in photoelectron and photofragment ion imaging of molecular oxygen. *Rev. Sci. Instru.*, 68:3477–3484, 1997.

[39] D. Townsend, M.P. Minitti, and A.G. Suits. Direct current slice imaging. *Rev. Sci. Instrum.*, 74(4):2530–2539, April 2003.

[40] Jim J. Lin, Jingang Zhou, Weicheng Shiu, and Kopin Liu. Application of time-sliced ion velocity imaging to crossed molecular beam experiments. *Rev. Sci. Instrum.*, 74(4):2495–2500, 2003.

[41] W. Li, S. D. Chambreau, S.A. Lahankar, and A.G. Suits. Megapixel ion imaging with standard video. *Rev. Sci. Instrum.*, 76(6):63106–63113, June 2005.

[42] F. Biraben, B. Cagnac, and G. Grynberg. Experimental evidence of two-photon transition without doppler broadening. *Phys. Rev. Lett.*, 32:643–645, 1974.

[43] M. D. Levenson and N. Bloembergen. Observation of two-photon absorption without doppler broadening on the $3s-5s$ transition in sodium vapor. *Phys. Rev. Lett.*, 32:645–648, 1974.

[44] T.W. HÃnsch, K.C. Harvey, G. Meisel, and A.L. Schawlow. Two-photon spectroscopy of na 3s-4d without doppler broadening using a cw dye laser. *Opt. Comm.*, 11:50–53, 1974.

[45] Marcus J. J. Vrakking, Allan S. Bracker, Toshinori Suzuki, and Yuan T. Lee. Ultrasensitive detection of hydrogen molecules by (2+1) resonance-enhanced multiphoton ionization. *Rev. Sci. Instrum.*, 64(3):645–652, 1993.

[46] Andrew E. Pomerantz and Richard N. Zare. Doppler-free multi-photon ionization: a proposal for enhancing ion images. *Chem. Phys. Lett.*, 370:515 – 521, 2003.

[47] J. Riedel, S. Dziarzhytski, A. Kuczmann, F. Renth, and F. Temps. Velocity map ion imaging of h atoms from the dissociation of hco using doppler-free multi-photon ionization. *Chem. Phys. Lett.*, 414:473–478, 2005.

[48] Cunshun Huang, Wen Li, Myung Hwa Kim, and Arthur G. Suits. Two-color reduced-doppler ion imaging. *J Chem. Phys.*, 125(12):121101, 2006.

[49] Cunshun Huang, Wen Li, Myung Hwa Kim, and Arthur G. Suits. Two-color reduced-doppler ion imaging. *J Chem. Phys.*, 125(12):121101, 2006.

[50] Noah T. Goldberg, Konrad Koszinowski, Andrew E. Pomerantz, and Richard N. Zare. Doppler-free ion imaging of hydrogen molecules produced in bimolecular reactions. *Chem. Phys. Lett.*, 439 - 443, 2007.

[51] Vasiliy Goncharov, Nuradhika Herath, and Arthur G. Suits. Roaming dynamics in acetone dissociation. *J Phys. Chem. A*, 112(39):9423–9428, 2008. PMID: 18588266.

[52] Dragana Č. Radenović, André J.A. van Roij, Shiou-Min Wu, J.J. Ter Meulen, David H. Parker, Mark P.J. van der Loo, Liesbeth M.C. Janssen, and Gerrit C. Groenenboom. Photodissociation of vibrationally excited oh/od radicals. *Mol. Phys.*, 106(2-4):557–572, 2008.

[53] Vasiliy Goncharov, Nuradhika Herath, Andrés Arregui, Luis Bañares, and Arthur G. Suits. Masked velocity map imaging: A one-laser-beam doppler-free spectroscopic technique. *J Phys. Chem. A*, 113(16):3840–3843, 2009.

[54] Xiubin Zhang, Jaime L. Rheinecker, and Joel M. Bowman. Quasiclassical trajectory study of formaldehyde unimolecular dissociation: H[sub 2]co –¿ h[sub 2] + co, h + hco. *J Chem. Phys.*, 122(11):114313, 2005.

[55] J. L. Rheinecker, X. Zhang, and J. M. Bowman. Quasiclassical trajectory studies of the dynamics of h2co on a global ab initio-based potential energy surface. *Mol. Phys.*, 103(6-8):1067–1074, 2005.

[56] Y. Badr, S. Abd El-Wanees, and M.A. Mahmoud. The ro-vibrational spectra of co molecule resulting from the photolysis of acetone. *J Photochem Photobio A: Chem.*, 167:159, 2004.

[57] C. L. Berrie, C. A. Longfellow, A. G. Suits, and Y. T. Lee. Infrared multiphoton dissociation of acetone in a molecular beam. *J Phys. Chem. A*, 105(12):2557–2562,

2001.

[58] D. J. Donaldson and S. R. Leone. Photofragmentation dynamics of acetone of 193 nm: State distributions of the ch3 and co fragments by time- and wavelength-resolved infrared emission. *J Chem. Phys.*, 85(2):817–824, 1986.

[59] G. E. Hall, H. W. Metzler, J. T. Muckerman, J. M. Preses, and Jr. R. E. Weston. Studies of the 193 nm photolysis of diethyl ketone and acetone using time-resolved fourier transform emission spectroscopy. *J Chem. Phys.*, 102(17):6660–6668, 1995.

[60] P. D. Lightfoot, S. P. Kirwan, and M. J. Pilling. Photolysis of acetone at 193.3 nm. *J Phys. Chem.*, 92(17):4938–4946, 1988.

[61] Simon W. North, David A. Blank, J. Daniel Gezelter, Cheryl A. Longfellow, and Yuan T. Lee. Evidence for stepwise dissociation dynamics in acetone at 248 and 193 nm. *J Chem. Phys.*, 102(11):4447–4460, 1995.

[62] Kenshi Takahashi, Tomoki Nakayama, Yutaka Matsumi, and Yoshihiro Osamura. Hydrogen atom formation in the photolysis of acetone at 193 nm. *J Phys. Chem. A*, 108(39):8002–8008, 2004.

[63] Sang Kyu Kim, Soren Pedersen, and Ahmed H. Zewail. Direct femtosecond observation of the transient intermediate in the alpha-cleavage reaction of (ch3)2co to 2ch3+co: Resolving the issue of concertedness. *J Chem. Phys.*, 103(1):477–480, 1995.

[64] S. A. Buzza, E. M. Snyder, D. A. Card, D. E. Folmer, and Jr. A. W. Castleman. Femtosecond excitation dynamics of acetone: Dissociation, ionization, and the evolution of multiply charged elemental species. *J Chem. Phys.*, 105(17):7425–7431, 1996.

[65] S. A. Buzza, E. M. Snyder, and Jr. A. W. Castleman. Further direct evidence for stepwise dissociation of acetone and acetone clusters. *J Chem. Phys.*, 104(13):5040–5047, 1996.

[66] J. C. Owrutsky and A. P. Baronavski. Ultrafast studies of the photodissociation of the acetone 3s rydberg state at 195 nm: Formation and unimolecular dissociation of the acetyl radical. *J Chem. Phys.*, 108(16):6652–6659, 1998.

[67] J. C. Owrutsky and A. P. Baronavski. Ultrafast photodissociation dynamics of the s[sub 1] and s[sub 2] states of acetone. *J Chem. Phys.*, 110(23):11206–11213, 1999.

[68] Q. Zhong, L. Poth, and Jr. A. W. Castleman. Ultrafast dissociation dynamics of acetone: A revisit to the s[sub 1] state and 3s rydberg state. *J Chem. Phys.*, 110(1):192–196, 1999.

[69] Eric W.-G. Diau, Carsten Kötting, and Ahmed H. Zewail. Femtochemistry of norrish type-i reactions: I. experimental and theoretical studies of acetone and related ketones on the s1 surface. *Chem Phys Chem*, 2(5):273–293, 2001.

[70] Wei-Kan Chen, Jr-Wei Ho, and Po-Yuan Cheng. Ultrafast photodissociation dynamics of the acetone 3s rydberg state at 195 nm: a new mechanism. *Chem. Phys. Lett.*, 380:411, 2003.

[71] Wei-Kan Chen and Po-Yuan Cheng. Ultrafast photodissociation dynamics of acetone at 195 nm: ii. unraveling complex three-body dissociation dynamics by femtosecond time-resolved photofragment translational spectroscopy. *J Phys. Chem. A*, 109(31):6818–6829, 2005. PMID: 16834037.

[72] Wei-Kan Chen, Jr-Wei Ho, and Po-Yuan Cheng. Ultrafast photodissociation dynamics of acetone at 195 nm: i. initial-state, intermediate, and product temporal evolutions by femtosecond mass-selected multiphoton ionization spectroscopy. *J Phys. Chem. A*, 109(31):6805–6817, 2005. PMID: 16834036.

[73] Dan Liu, Wei-Hai Fang, and Xiao-Yuan Fu. An ab initio study on photodissociation of acetone. *Chem. Phys. Lett.*, 325(86), 2000.

[74] E. Martinez-Nunez, A. Fernandez-Ramos, M. N. D. S. Cordeiro, S. A. Vazquez, F. J. Aoiz, and L. Banares. A direct classical trajectory study of the acetone photodissociation on the triplet surface. *J Chem. Phys.*, 119(20):10618–10625, 2003.

[75] Eric W.-G. Diau, Carsten Kötting, Theis I. Sølling, and Ahmed H. Zewail. Femtochemistry of norrish type-i reactions: Iii. highly excited ketones—theoretical. *ChemPhysChem*, 3(1):57–78, 2002.

[76] Simon North, David A. Blank, and Yuan T. Lee. Determination of the barrier height to ch3co dissociation. *Chem. Phys. Lett.*, 224:38, 1994.

[77] G. A. Skorobogatov, A. G. Meilakhs, Yu. I. Pogosyan, and V. K. Khripun. New mechanism of photodissociation of gaseous acetone. *Rus. J Gen. Chem.*, 72:1271–1275, 2002. 10.1023/A:1020896200573.

[78] Theis I. Sølling, Eric W.-G. Diau, Carsten Kötting, Steven De Feyter, and Ahmed H. Zewail. Femtochemistry of norrish type-i reactions: Iv. highly excited ketones—experimental. *ChemPhysChem*, 3(1):79–97, 2002.

[79] Satoshi Maeda, Koichi Ohno, and Keiji Morokuma. A theoretical study on the photodissociation of acetone: Insight into the slow intersystem crossing and exploration of nonadiabatic pathways to the ground state. *J Phys. Chem. Lett.*, 1(12):1841–1845, 2010.

[80] Cunshun Huang, Armando D. Estillore, and Arthur G. Suits. State-selected imaging of hcco radical photodissociation dynamics. *J Chem. Phys.*, 128(13):134301, 2008.

[81] J. T. Muckerman. Information theoretic prior functions for large molecular systems. *J Phys. Chem.*, 93(1):179–184, 1989.

[82] Karen A. Trentelman, Scott H. Kable, David B. Moss, and Paul L. Houston. Photodissociation dynamics of acetone at 193 nm: Photofragment internal and translational energy distributions. *J Chem. Phys.*, 91(12):7498–7513, 1989.

[83] A. Woeldike V.H. Schuler. *Phys. Z*, 45:171, 1944.

[84] S. H. Hastings and F. A. Matsen. The photodecomposition of nitrobenzene. *J. Am. Chem. Soc.*, 70(10):3514–3515, 1948.

[85] G. M. Nazin V.G. Matveev. Kinetic s and mechanism of nitrobenzene in gas phase. *Bull. Acad. Sci. USSR Div. Chem. Sci.*, 24:697, 1975.

[86] Alicia C. Gonzalez, C. William Larson, Donald F. McMillen, and David M. Golden. Mechanism of decomposition of nitroaromatics. laser-powered homogeneous pyrolysis of substituted nitrobenzenes. *J Phys. Chem.*, 89(22):4809–4814, 1985.

[87] Wing Tsang, David Robaugh, and W. Gary Mallard. Single-pulse shock-tube studies on c-no2 bond cleavage during the decomposition of some nitro aromatic compounds. *J Phys. Chem.*, 90(22):5968–5973, 1986.

[88] B. Ward G. Porter. The photolutic preparation of cyclopentadienyl and phenyl from benzene derivatives. *Proc. R. Soc. Landon Ser. A*, 303:139, 1968.

[89] Douglas B. Galloway, Jeffrey A. Bartz, L. Gregory Huey, and F. Fleming Crim. Pathways and kinetic energy disposal in the photodissociation of nitrobenzene. *J Chem. Phys.*, 98(3):2107–2114, 1993.

[90] Douglas B. Galloway, Thomas Glenewinkel-Meyer, Jeffrey A. Bartz, L. Gregory Huey, and F. Fleming Crim. The kinetic and internal energy of no from the photodissociation of nitrobenzene. *J Chem. Phys.*, 100(3):1946–1952, 1994.

[91] Ming-Fu Lin, Yuan T. Lee, Chi-Kung Ni, Shucheng Xu, and M. C. Lin. Photodissociation dynamics of nitrobenzene and o-nitrotoluene. *J Chem. Phys.*, 126(6):064310, 2007.

[92] C. Kosmidis, K.W.D. Ledingham, A. Clark, A. Marshall, R. Jennings, and R.P. Singhal J. Sander. On the dissociation pathways of nitrobenzene. *Int. J Mass. spectrom. IOn. Proc.*, 41:873, 2008.

[93] Roger D. van Zee, M. Frances Foltz, and C. Bradley Moore. Evidence for a second molecular channel in the fragmentation of formaldehyde. *The Journal of Chemical Physics*, 99(3):1664–1673, 1993.

[94] Nuradhika Herath and A.G. Suits. Roaming radical reactions. *J Phys. Chem. Lett.*, 2:642, 2011.

[95] Shucheng Xu and M. C. Lin. Computational study on the kinetics and mechanism for the unimolecular decomposition of c6h5no2 and the related c6h5 + no2 and c6h5o + no reactions. *J Phys. Chem. B*, 109(17):8367–8373, 2005. PMID: 16851982.

[96] Guillaume Fayet, Laurent Joubert, Patricia Rotureau, and Carlo Adamo. Theoretical study of the decomposition reactions in substituted nitrobenzenes. *J Phys. Chem. A*,

112(17):4054–4059, 2008. PMID: 18393478.

[97] Karen J. Castle, James E. Abbott, Xianzhao Peng, and Wei Kong. Photodissociation of o-nitrotoluene between 220 and 250 nm in a uniform electric field. *J Phys. Chem. A*, 104(45):10419–10425, 2000.

[98] S. C. Chen, S. C. Xu, E. Diau, and M. C. Lin. A computational study on the kinetics and mechanism for the unimolecular decomposition of o-nitrotoluene. *J Phys. Chem. A*, 110(33):10130–10134, 2006.

[99] Carlos Gonzalez and H. Bernhard Schlegel. An improved algorithm for reaction path following. *J Chem. Phys.*, 90(4):2154–2161, 1989.

[100] M. J. Frisch, G. W. Trucks, H. B. Schlegel, G. E. Scuseria, M. A. Robb, J. R. Cheeseman, G. Scalmani, V. Barone, B. Mennucci, G. A. Petersson, H. Nakatsuji, M. Caricato, X. Li, H. P. Hratchian, A. F. Izmaylov, J. Bloino, G. Zheng, J. L. Sonnenberg, M. Hada, M. Ehara, K. Toyota, R. Fukuda, J. Hasegawa, M. Ishida, T. Nakajima, Y. Honda, O. Kitao, H. Nakai, T. Vreven Jr., J. A. Montgomery, J. E. Peralta, F. Ogliaro, M. Bearpark, J. J. Heyd, E. Brothers, K. N. Kudin, V. N. Staroverov, R. Kobayashi, J. Normand, K. Raghavachari, A. Rendell, J. C. Burant, S. S. Iyengar, J. Tomasi, M. Cossi, N. Rega, J. M. Millam, M. Klene, J. B. Knox, J. E.and Cross, V. Bakken, C. Adamo, J. Jaramillo, R. Gomperts, R. E. Stratmann, O. Yazyev, A. J. Austin, R. Cammi, C. Pomelli, J. W. Ochterski, R. L. Martin, K. Morokuma, V. G. Zakrzewski, G. A. Voth, P. Salvador, S. Dannenberg, J. J.and Dapprich, A. D. Daniels, O. Farkas, J. B. Foresman, J. V. Ortiz, J. Cioslowski, and D. J. Fox. Gaussian 09(revision a. 1.), gaussian, inc., wallingford, ct,. 2009.

[101] D. M. Wardlaw and R.A. Marcus. Rrkm reaction rate theory for transition states of any looseness. *Chem. Phys. Lett.*, 110:230, 1984.

[102] S.J. Llippenstein, A. F. Wagner, S.H. Robertson, and D.M. Dubner, R.and Wardlaws. Variflex software: Version 1.00 abalable at http://chemistry.anl.gov/variflex. 1999.

[103] J.W.C. Johns, J. Reid, and D.W. Lepard. The vibration-rotation fundamental of no.

J Mol. Spec., 65:155, 1977.

[104] Hongyan Xiao, Satoshi Maeda, and Keiji Morokuma. Excited-state roaming dynamics in photolysis of a nitrate radical. *J Phys. Chem. Lett.*, 2(9):934–938, 2011.

[105] E.P. Olaguer. *Enviorn. Sci. Poll. Res.*, 9:175, 2002.

[106] Carrie J. Christiansen and Joseph S. Francisco. Atmospheric oxidation of tetrachloroethylene: An ab initio study. *J Phys. Chem. A*, 114(34):9177–9191, 2010.

[107] Rouslan V. Olkhov and Ian W. M. Smith. Time-resolved experiments on the chlorine atom initiated oxidation of tetrachloroethene (cl2cccl2). *J Phys. Chem. A*, 108(12):2232–2237, 2004.

[108] L. P. Thüner, I. Barnes, K. H. Becker, T. J. Wallington, L. K. Christensen, J. J. Orlando, and B. Ramacher. Atmospheric chemistry of tetrachloroethene (cl2cccl2): products of chlorine atom initiated oxidation. *J Phys. Chem. A*, 103(43):8657–8663, 1999.

[109] I. J. Simson, S. Menardi, N. J. Blake, F. S. Rowland, and D.R. Blake. *J. Geophys. Res. Lett.*, 31:L08108, 2004.

[110] A. D. Walsh. The absorption spectra of the chloro ethylenes in the vacuum ultra-violet. *Trans. Faraday Soc.*, 41:35–45, 1945.

[111] Michael J. Berry. Chloroethylene photochemical lasers: Vibrational energy content of the hcl molecular elimination products. *J Chem. Phys.*, 61(8):3114–3143, 1974.

[112] Bradley A. Williams, Terrill A. Cool, and Celeste M. Rohlfing. Multiphoton spectroscopy of rydberg states of tetrachloroethylene. *J Chem. Phys.*, 93(3):1521–1532, 1990.

[113] Eric J. Bylaska, Michel Dupuis, and Paul G. Tratnyek. Ab initio electronic structure study of one-electron reduction of polychlorinated ethylenes. *J Phys. Chem. A*, 109(26):5905–5916, 2005.

[114] Sundaram Arulmozhiraja, Masahiro Ehara, and Hiroshi Nakatsuji. Electronic transitions in cis- and trans-dichloroethylenes and tetrachloroethylene. *J. Chem. Phys.*,

129(17):174506, 2008.

[115] S. Eden, B. Barc, N. J. Mason, S. V. Hoffmann, Y. Nunes, and P. Limão-Vieira. Electronic state spectroscopy of c2cl4. *Chem Phys*, 365:150, 2009.

[116] Armando D. Estillore, Laura M. Visger-Kiefer, Tarek Abdul Ghani, and Arthur G. Suits. Dynamics of h and d abstraction in the reaction of cl atom with butane-1,1,1,4,4,4-d6. *Phys. Chem. Chem. Phys.*, 13:8433–8440, 2011.

[117] Masayuki Umemoto, Kanekazu Seki, Hisanori Shinohara, Umpei Nagashima, Nobuyuki Nishi, Minoru Kinoshita, and Ryoichi Shimada. Photofragmentation of mono- and dichloroethylenes: Translational energy measurements of recoiling cl and hcl fragments. *J Chem. Phys.*, 83(4):1657–1666, 1985.

[118] Kenichi Tonokura, Lizla B. Daniels, Toshinori Suzuki, and Koichi Yamashita. Ccl bond rupture in ultraviolet photodissociation of vinyl chloride. *J Phys. Chem. A*, 101(42):7754–7764, 1997.

[119] Sundaram Arulmozhiraja, Ryoichi Fukuda, Masahiro Ehara, and Hiroshi Nakatsuji. Electronic spectra and photodissociation of vinyl chloride: A symmetry-adapted cluster configuration interaction study. *J Chem. Phys.*, 124(3):034312, 2006.

[120] Paul M. Regan, Stephen R. Langford, Daniela Ascenzi, Phillip A. Cook, Andrew J. Orr-Ewing, and Michael N. R. Ashfold. Spin-orbit branching in cl(2p) atoms produced by ultraviolet photodissociation of hcl. *Phys. Chem. Chem. Phys.*, 1:3247–3251, 1999.

[121] Michael N. R. Ashfold, Graeme A. King, Daniel Murdock, Michael G. D. Nix, Thomas A. A. Oliver, and Alan G. Sage. I[euro sign]i[function of]* excited states in molecular photochemistry. *Phys. Chem. Chem. Phys.*, 12(6):1218–1238, 2010.

[122] David A. Blank, Weizhong Sun, Arthur G. Suits, Yuan T. Lee, Simon W. North, and Gregory E. Hall. Primary and secondary processes in the 193 nm photodissociation of vinyl chloride. *J Chem. Phys.*, 108(13):5414–5425, 1998.

[123] J.A. Manion. *J Chem. Phys.*, 31:123, 2002.

[124] J Mettews, A. Sinha, and J.S. Francisco. The importance of weak absorption features

in promoting tropospheric radical production. *PNAS*, 102:7449–7452, 2005.

[125] R. L. Sinha, A.and Vanderwal and F. F Crim. The vibrationally mediated photodissociation dynamics of nitric-acid. *J. Chem. Phys.*, 91:2929–2938, 1989.

[126] A. A. Turnipseed, G. L. Vaghjiani, J. E. Thompson, and A. R. Ravishankara. Photodissociation of hno3 at 193, 222, and 248 nm - products and quantum yields. *J. Chem. Phys.*, 96(8):5887–5895, April 1992.

[127] P. Felder, X. F. Yang, and J. R. Huber. Photodissociation of nitric-acid in a cold molecular-beam at 193 nm. *Chem. Phys. Lett.*, 215:221–227, 1993.

[128] A. Schiffman, D. D. Nelson, and D. J. Nesbitt. Quantum yields for oh production from 193 and 248 nm photolysis of hno3 and h2o2. journal of chemical physics. *J. Chem. Phys.*, 98:6935–6945, 1993.

[129] J. R. Huber. Photochemistry of molecules relevent to the atmosphere:photodissocaito of ntric acid in the gas phase. *Chem Phys Chem*, 5:1663–1669, 2004.

[130] F. Y. Wang, Z. C. Chen, Y. W. Zhang, Q. Shuai, B. Jiang, D. X. Dai, X. Y. Wang, and X. M. Yang. Uv photodissociation dynamics of nitric acid: The hydroxyl elimination channel. *Chi. J. Chem. Phys.*, 22:191–196., 2009.

[131] F Assenmacher, M Gutmann, F Noack, V Stert, and W Radloff. Femtosecond photodissociation dynamics of hno3 after exitation of the s-3-state at 200 nm. *App. Phys. B*, 71(3):385–390, September 2000.

[132] T.L. Myers, N.R. Forde, B. Hu, D.C. Kitchen, and L.J. Butler. The influence of local electronic character and nonadiabaticity in the photodissociation of nitric acid at 193 nm. *J. Chem. Phys.*, 107(14):5361–5373, October 1997.

[133] P. S. Yeh, G. H. Leu, Y. P. Lee, and I. C. Chen. Photodissociation of hno3 at 193 nm - near-infrared emission of no detected by time-resolved fourier-transform spectroscopy. *J. Chem. Phys.*, 103(12):4879–4886, September 1995.

[134] Q Li, R.T. Carter, and J.R. Huber. The photodissociation dynamics of nitric acid studied at 193 nm by lif and rempi-tof methods. *Chem. Phys. Lett.*, 334(1-3):39–46,

February 2001.

[135] M.J. Krisch, M.C. Reid, L.R. McCunn, L.J. Butler, and J. Shu. Photofragment translational spectroscopy of nitric acid at 248 nm with vuv photoionization detection of products. *Chem. Phys. Lett.*, 397:21–25, 2004.

[136] M. Nonella, H. U. Suter, and J. Robert Huber. An ab initio and dynamics study of the photodissociation of nitric acid hno3. *Chem. Phys. Lett.*, 487(1-3):28–31, February 2010.

[137] Y. Y. Bai and G. A. Segal. Features of the electronic potential-energy surfaces of nitric-acid below 7 ev. *J. Chem. Phys.*, 92:7479–7483., 1990.

[138] D.W. Neyer, A.J.R. Heck, and D.W. Chandler. Photodissociation of n2o: J-dependent anisotropy revealed in n-2 photofragment images. *J. Chem. Phys.*, 110(7):3411–3417, February 1999.

[139] A.S. Bracker, E.R. Wouters, A.G. Suits, and O.S. Vasyutinskii. Imaging the alignment angular distribution: State symmetries, coherence effects, and nonadiabatic interactions in photodissociation. *J. Chem. Phys.*, 110:6749, 1999.

[140] Elroy R. Wouters, Musahid Ahmed, Darcy S. Peterka, Allan S. Bracker, Arthur G. Suits, and Oleg S. Vasyutinskii. Imaging the atomic orientation and alignment in photodissociation. In *ACS Symposium Series*, number 770 in Imaging in Chemical Dynamics, pages 238–284. 2000.

[141] Yuxiang Mo and Toshinori Suzuki. Vector correlation in molecular photodissociation: Quantum mechanical expression and comparison with the formal expansion formula. *J Chem. Phys.*, 112(8):3463–3473, 2000.

[142] A. G. Smolin, O. S. Vasyutinskii, E. R. Wouters, and A. G. Suits. Orbital alignment in n2o photodissociation. i. determination of all even rank anisotropy parameters. *J. Chem. Phys.*, 121:6759–6770, 2004.

[143] Peter S. Shternin and Oleg S. Vasyutinskii. The parity-adapted basis set in the formulation of the photofragment angular momentum polarization problem: The role of

the coriolis interaction. *J Chem. Phys.*, 128(19):194314, 2008.

[144] Vladislav V. Kuznetsov, Peter S. Shternin, and Oleg S. Vasyutinskii. The role of the coriolis interaction on vector correlations in molecular predissociation: Excitation of isolated rotational lines. *J Chem. Phys.*, 130(13):134312, 2009.

[145] King G.W. and Moule. D. The ultraviolet absorption spectrum of nitrous acid in the vapor state. *Can. J. Chem.*, 40:2057–2065., 1964.

[146] P.O. DehayemKamadjeu, J. Orphal, I. Kleiner, and P. Flaud. The far-infared rotational spectrum of nitrous acid(hono) and its deuterated species(dono) studied by high-resolution fourier-transform spectroscopy. *J Mol. Bio.*, 234:182–189, 2005.

[147] C. G.and Huang Yu, S. Y.and Zhang. A cas study of the so, t-1, s-1, t-2, and s-2 states of the trans-hono molecule. *Chem. Phys. Lett.*, 440:187–193, 2007.

[148] SJ Baek, CR Park, and HL Kim. Photodissociation dynamics of hno3 at 266 nm. *J Photochem Photobio A*, 104(1-3):13–18, April 1997.

[149] Y Miller, G.M Chaban, B.J Finlayson-Pitts, and R.B Gerber. Photochemical processes induced by vibrational overtone excitations: Dynamics simulations for cis-hono, trans-hono, hno3, and hno3-h2o. *J Phys. Chem. A*, 110(16):5342–5354, April 2006.

[150] A. M. Wodtke, E. J. Hintsa, and Yuan T. Lee. Infrared multiphoton dissociation of three nitroalkanes. *The Journal of Physical Chemistry*, 90(16):3549–3558, 1986.

[151] Pablo A. Denis, Oscar N. Ventura, Hung Thanh Le, and Minh Tho Nguyen. Density functional study of the decomposition pathways of nitroethane and 2-nitropropane. *Phys. Chem. Chem. Phys.*, 5:1730–1738, 2003.

ABSTRACT

STATE RESOLVED SLICE IMAGING OF PHOTOCHEMICAL DYNAMICS

by

Herath Mudiyanselage Nuradhika Herath

August 2012

Advisor: Arthur G. Suits

Major: Chemistry (Physical)

Degree: Doctor of Philosophy

This dissertation focuses on the understanding the unimolecular photochemistry and dynamics utilizing state-resolved slice imaging approach combined with the quantum-state selective spectroscopy technique called resonance enhanced multi photon ionization (REMPI) method. This powerful technique allows selecting the initial quantum states of the reactants and determining the final quantum states, energy, the orientation and alignments of the products. In the investigations of photodissociation dynamics of acetone at 230 nm, a bimodal distribution for the resulting CO photoproduct is identified. This observation indicated the presence of unimolecular dissociation mechanism analogues to the roaming dynamics reported in formaldehyde photodissociation. Moreover, another type of roaming mechanism called "roaming-mediated isomerization" is introduced in the study of nitrobenzene photodissociation. In this study molecules undergo roaming type isomerization before the simple bond fission take place. In the study of photodissociation dynamics of tertachloroethylene (TCE) at 235 nm and 202 nm using state resolved slice imaging approach illustrate that the dissociation take place at the ground state despite the difference in the excitation energies. A similar spin-orbit branching ratio of Cl/Cl* at both wavelengths are observed due to the above dynamical behavior of the molecule. In the study of HNO_3

photodissociation near 204 nm report the translational energy and angular momentum distributions of the resulting $O(^1D)$ product. The vibrational energy distribution of the HONO co-product, as seen through the $O(^1D)$ translational energy distribution, shows significant vibrational energy remaining in the molecule. Analysis of the angular distributions from both the $^1F_3 \leftarrow\leftarrow {}^1D_2$ and $^1P_1 \leftarrow\leftarrow {}^1D_2$ O probe transitions offer additional insight into the dynamics of the dissociation of nitric acid through the S_3 ($2\ ^1A'$) excited state, helping to resolve some outstanding questions and pointing the way to future studies. This approach allowed us to identify new mechanisms and channels created during the photodissociation events, calculate the branching ratios and infer the complex reactive processes in combustion, atmospheric and interstellar chemistry.

AUTOBIOGRAPHICAL STATEMENT

HERATH MUDIYANSELAGE NURADHIKA HERATH

Education

08/2012 Ph.D., Chemistry, Wayne State University.
05/2005 B.S., Chemistry, University Of Peradeniya.

Awards and Honors

2007 Departmental Citation for Excellence in Teaching Service

Recent Publications

1. M. Hause, N. Herath, R. Zhu, M. C. Lin, and A. G. Suits, "Roaming-Mediated Isomerization in the Photodissociation of Nitrobenzene", *Nature Chemistry*, 3, 932 (2011).

2. N. Herath, M. Hause and A. G. Suits, "The photodissociation dynamics of tetracholoroethylene" *Journal of Chemical Physics*, **134**, 164301.

3. N. Herath and A. G. Suits, "Roaming radical reactions", *Journal ofPhysical Chemistry Letters*, **2**, 642 (2011).

4. N. Herath, S. C. Everhart, A. G. Suits, O. S. Vasyuntinskii, "Slice imaging of nitric acid photodissociation: The O(1D) + HONO Channel", *Journal of Chemical Physics*, **134**, 034311 (2011).

5. V. Goncharov, N. Herath, A. Arregui, L. Banares, A. G. Suits, "Masked velocity map imaging: A one-laser-beam Doppler-free spectroscopic technique", *Journal of Physical Chemistry A*, **113**, 3840 (2009).

6. V. Goncharov, N. Herath and A. G. Suits, "Roaming dynamics in acetone dissociation", *Journal of Physical Chemistry A*, **112**, 9423 (2008).